NORTHWESTERN UNIVERSITY

Assessing Optimal Modes of Soil Parameter Identification

A DISSERTATION

SUBMITTED TO THE GRADUATE SCHOOL

IN PARTIAL FULFILLMENT OF THE REQUIREMENTS

for the degree

DOCTOR OF PHILOSOPHY

Field of Civil and Environmental Engineering

By

Anastasia Nally

EVANSTON, ILLINOIS

June 2022

ABSTRACT

This thesis describes an exploratory project to develop a highly non-traditional approach to devise novel test methods for characterizing the properties of materials that are essential to the design of sustainable and resilient infrastructure, particularly naturally occurring materials such as soils and rocks.

The central idea is that the material itself should inform the test method that most effectively reveals the material's strength and deformability. Existing methods for inferring mechanical properties of materials through field tests or laboratory experiments have evolved largely by trial and error, and there is no general, systematic approach for evaluating one possible approach against another. Moreover, existing characterization techniques are inadequate for determining all parameters required to define the material's behavior, particularly when the number of parameters is large.

A metric to compare tests is devised by (1) creating a min-max optimization of parameter sensitivities, taking into account the local and global topological properties of the forward model, and (2) evaluating the proposed metric for fundamental material tests. Using optimization to minimize the proposed metric, the result will return the optimal material parameter test for the given constraints. The proposed metric is first implemented to simple material tests with analytical forward models before being applied to finite element analysis where more complex topology optimization can be performed.

A parallel objective is included in the exploratory project, which investigates a new method to continuously discover material parameters. Prevailing techniques for on-site assessment of material parameters are capable of providing information only at specific locations—a significant shortcoming since soil parameters can vary widely over small areas. The key idea explored in this work is that opportunities for continuous characterization of ground conditions are already present in most situations, through the presence of ground-engaging equipment. The development of new techniques for discovering material parameters in this way will have a significant impact,

particularly in the fields of construction and trafficability.

Achievement of the objectives set out in this thesis will form the first step in enabling the discovery of new devices and testing protocols that will potentially revolutionize the way material parameters are measured.

ACKNOWLEDGEMENTS

First and foremost, I would like to thank Professor James Hambleton (Jim), whom brought me to Northwestern from Newcastle University and for providing support and guidance as my advisor throughout my research. I also want to acknowledge and thank Professors Richard Finno, Giuseppe Buscarnera, and Simge Küçükyavuz for being on my dissertation committee and providing valuable advice, suggestions, and critiques on my work.

Furthermore, for the trafficibility work contained in Chapter 5, thank you to Professor Nina Stark and her Virginia Tech research team, in particular Julie Paprocki. Thanks for inviting me to join the field work and helping me in completing my testing.

I would also like to acknowledge my friends and family who have given me support and cut me slack during this time. This period of my life has been one of immense growth and challenges. I value every discussion we have had, every piece of advice that was given to me, and every moment we have spent together. I sincerely thank you.

Finally, I want to give a special thanks to eight people without whom this achievement would not have been possible: my partner Hayley, my mother Dianne, my siblings Christopher, Harrison, and Stephanie, and my dear friends Martha, Tierney, and Hayley. Thank you for your constant and unconditional encouragement and support, even if for some of you that has been from a distance!

TABLE OF CONTENTS

LIST OF FIGURES

LIST OF TABLES

CHAPTER 1
INTRODUCTION AND LITERATURE REVIEW

A commonality in all geotechnical analysis is the presence of soil material parameters. These parameters are critically important to all of society, as they feed into the computations that lead to the construction of infrastructure and the prediction or understanding of major natural events, such as landslides and subsidence. Therefore, the accurate determination of these material parameters is vital to advancing our world in terms of geotechnical engineering. For this reason, the material parameter determination field is understandably highly researched with many new and innovative soil material parameter determination techniques constantly being developed.

Among all methods for material parameter determination, both *in situ* and laboratory, there is little indication as to the optimal method to test materials. The term *optimal* in this context implies that the desired parameters can be extracted from a single test most easily and accurately. Should we be unlimited by the apparatus and the modes in which we can deform materials, we might expect that there is an optimal method in which we can extract material parameters. This could be in the form of applying a combination of tractions and displacements to the boundaries of an arbitrary volume of material and measuring the material response, as shown in Figure 1.1.

An increasingly common method of material parameter determination is through inverse analysis. An example of the inverse analysis process for material parameter determination is presented in Figure 1.2. With this approach, an action is applied to the material, and a reaction is measured. The data generated from this test is used to create a forward model, and this forward model is used in the inverse model in order to determine material parameters. A series of tests which can be used in an inverse analysis, are presented in Figure 1.2(a). Each of these tests are presented here because they have a particular significance to the work in this thesis.

Similar to previous works in inverse analysis, this thesis focuses on material parameter determination. However, here the focus is to reinvent entirely the methodology of how to design a

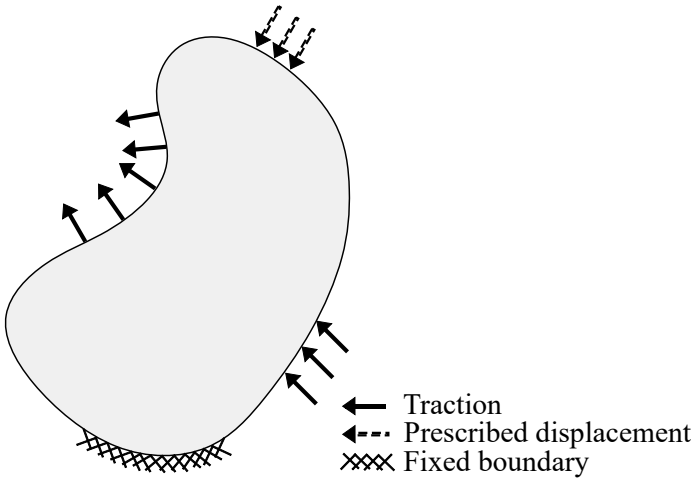

Figure 1.1: Arbitrary volume of material.

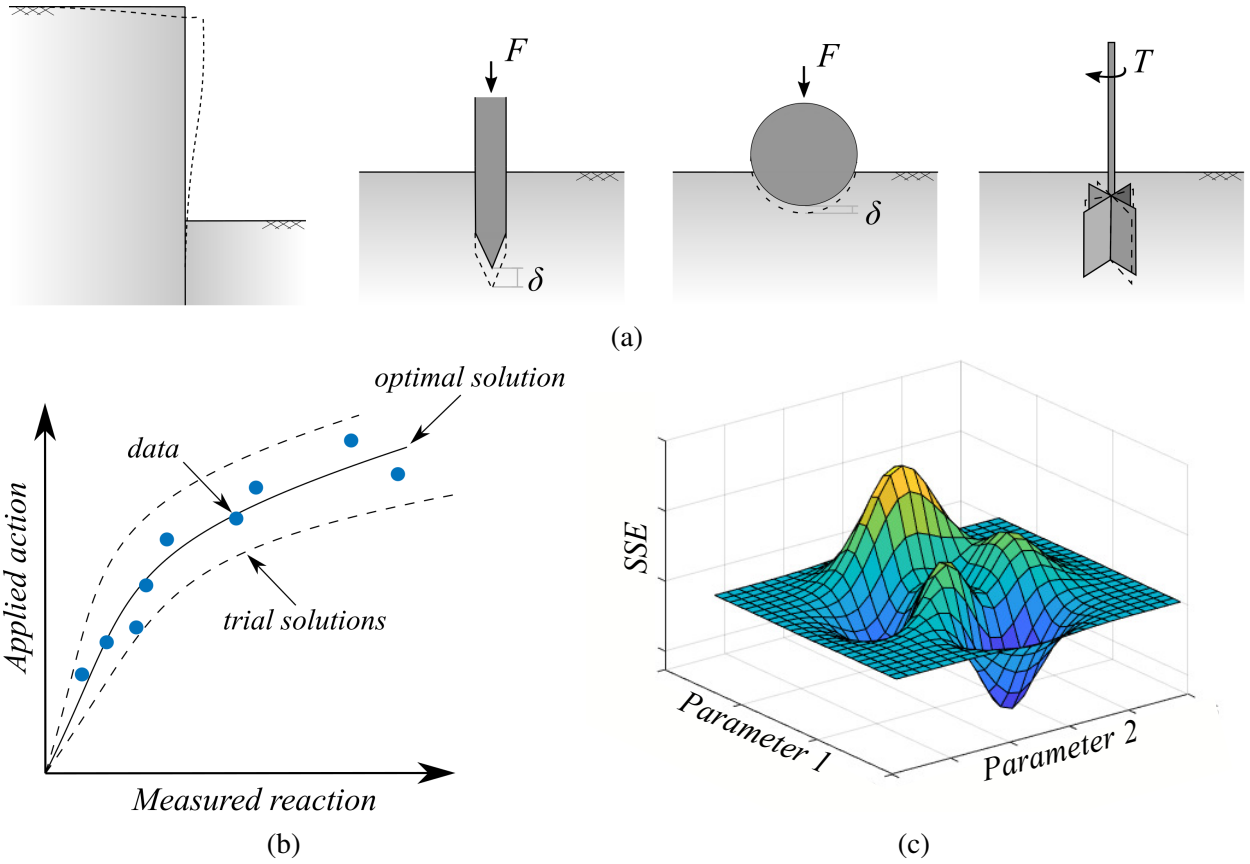

Figure 1.2: Inverse process for material parameter determination: (a) tests: wall displacement [1–6], penetration, indentation, and vane shear; (b) forward model; (c) inverse model. Sub-figure (c) is partially reconstructed from [7].

material test. The overarching aim is to create a methodology to design optimal soil tests, and this is done by effectively optimizing the inverse procedure presented in Figure 1.2. This optimization is completed by considering test configurations, boundary conditions, and the testing procedure, to compare tests in a quantitative way.

This is explored in two distinct tracks. Track I provides the first step in being able to compare material tests by quantifying desirable features and developing a quantitative metric. Track II investigates methods of continuous surface profiling. Aiming to demonstrate that properties of materials can be inferred from simple ground-engaging equipment movements, thus guiding future work to implement the quantitative metric developed in Track I. This introduction provides the necessary background to understand the current state of research and the knowledge gaps addressed by this thesis. The history and current state of material parameter testing is outlined (Section 1.1) to illustrate how the work in this thesis approaches the methodology of designing a test in an entirely new way. Furthermore, the test comparison methodology that is developed uses knowledge from optimization, specifically inverse analysis and topology optimization (Section 1.2), and sensitivity analysis (Section 1.3) to first determine desirable features of a material test and then design a quantitative metric. Section 1.4 reviews the fields relevant to the work of designing a continuous field test, including trafficability, remote sensing, and photogrammetry. Finally, Section 1.5 outlines the structure of this thesis and details the specific aims that are addressed.

1.1 Conventional soil parameter determination

Both *in situ* and laboratory testing fundamentally rest on mechanically deforming (actuating) the material and simultaneously measuring its response in terms of displacements and stresses (reactions). While these existing test procedures can be both accurate and reliable, they have *ad hoc* origins. The methods of determining soil parameters from laboratory tests have evolved significantly since their origin, such as that of a soil classification system by Atterberg in 1900 [8] and the triaxial test device by Casagrande in 1930 [9]. The continual improvement of these tests has allowed advancements over the years, although, the origin of these tests remaining for the sake

of convenience has remained almost unchanged. For example, triaxial specimens are traditionally sized with standard height-to-diameter ratios. When radial drainage is used, a ratio of 2:1 is recommended, to allow a combination of the solution for vertical and radial drainage to be used [10]. This sizing has not been proven as an optimal selection. This traditional method of sizing triaxial specimens is the current practice adopted by most regulatory authorities around the world, and the situation remains similar for most traditional laboratory testing procedures. Furthermore, the development of many *in situ* tests has come from the widespread need for an applicable test, resulting in similar methods being simultaneously developed. For example, the development of the vane shear test came from the necessity to determine more accurate undisturbed shear strengths in clay, and history suggests multiple very similar devices were simultaneously developed. The first use of a vane shear-like device was in 1919 on the site of the Lidingo Bridge in Stockholm, Sweden [11]. Yet an independent and very similar device was patented in 1929 in Germany (German patent No. 508 711), although, there is no information regarding the German device's use in practice. Later, two vane shear devices were developed in the North America by Vey & Schlesinger [12], and Lea in 1950 [13], and the device was standardized by Cadling & Odenstand in 1950 [14]. Although this device is heavily researched and is very effective in practice today, again, there is no fundamental justification as to its standardized design and operation, specifically referring to being an optimal device. Furthermore, there are a rising number of less conventional material tests, mostly designed for *in situ* deployment. These include balls, t-bars, torpedo-like devices [15–17], and intelligent compaction [18, 19], as well as remote sensing options such as satellites, radar, and images to infer soil mechanical properties [20–24]. These tests each possess their own motivation, with some designed for maximum convenience, robustness in harsh environments, or durability. Most of these tests focus on the near-surface material and typically have no indication of being an optimal test.

Another significant drawback of a conventional soil-testing program is the reliance on spot-checking, which typically cannot assess more than a few percent of the entire construction area. This leaves the rest to engineering judgment, which ultimately yields over-conservative designs or costly failures in terms of (1) construction delays, (2) shortened design life, and/or (3) increased

maintenance requirements. Striving for optimal performance in the context of engineering is ideal because it reduces cost, time, and inaccuracies. With geotechnical site investigation a necessary cost, using the optimal material testing program will result in savings down the line.

1.2 Optimization—inverse analysis and topology optimization

Optimization refers to maximizing or minimizing a mathematical function—the objective function—to find the desired optimal solution, and is used extensively throughout this thesis. Inverse analysis is a type of optimization that specifically aims to retrieve unknown parameters by fitting experimental data to modeled data. In the case applicable to this work, and presented in Figure 1.2, the model of the system is the forward model and is used to compute data that are compared to the respective experimental data. The model parameters that provide the closest match to the experimental data solve the inverse problem [25–28]. Optimization in the case of inverse analysis automates the inverse problem by taking a mathematical expression of the inverse problem (e.g. the sum of squared errors between the modeled data and experimental data) and minimizes this. The exact method in which the optimization minimizes the mathematical expression is dependent on the optimization solver used, and this is explored in more depth in Chapters 3 and 4.

The use of inverse analysis for material parameter determination is a significant area of research. Yin *et al.* [29] provides a review of material parameter determination in geotechnical engineering through optimization. Previous works specific to geotechnical engineering have combined optimization solvers with finite element software such as PLAXIS, FLAC, and ABAQUS to predict the material parameters. Such applications include modeling pseudo *in situ* tests [30–32], deep supported excavations [1–6], dams [33], and underground works [34, 35]. Many of these studies also include a sensitivity analysis, which is specifically addressed in Section 1.3. More broadly than geotechnical engineering, material parameter determination through inverse analysis is used in many other fields for which knowledge can be gained to assist the work in this thesis. In particular, there are significant bodies of work determining material parameters using inverse analysis in other areas such as indentation tests [28, 36–39], penetration tests [40], and in the study

of elasticity [41, 42]. Of particular note, Zhang *et al.* [38] showed that the type of measurement that is taken is significant, as some measurements in their work lead to a non-unique solution impacting the analysis. The measurements Zhang *et al.* considered included indenter displacement and disturbed surface profile.

Topology optimization differs from inverse analysis in the formation of the objective function. In topology optimization the objective function describes features such as cost or weight, and this is minimized by changing the topology of the problem. Topology optimization is a multidisciplinary field that covers a significant array of problems and aims to determine the optimal shape/structure/layout of a problem, given an objective to minimize. Eschenauer & Olhoff [43] and Sigmund & Maute [44] provide reviews of the field of topology optimization. Eschenauer & Olhoff provide a detailed history of the development of the field and Sigmund & Maute focus on the approach each work takes to solve the optimization. The objective of using topology optimization in design is usually to minimize the cost or size of a design relative to a set of constraints. The constraints often include any geometric constraints specific to the design, factors of safety, and stability constraints. Topology optimization is often thought of as the design of structural elements for minimizing cost and maximizing strength. Specific applications in geotechnical engineering include the design of retaining walls [45–49] and shallow foundations [50, 51].

Optimization is a significantly broad subject area, and details above were given for two specific sub areas with significant application to the work in this thesis. There are endless other applications across the field and more specifically, many other applications within geotechnical engineering. Kashani *et al.* [52] provides a review of the application of optimization in geotechnical engineering with a emphasis placed on optimizations that implemented particle swarm optimization. Such applications not mentioned above include predicting the critical slip surface in slope stability by minimizing the factor of safety [53–58] and load capacity of piles using artificial neural networks [59–63] as well as many others.

The work in this thesis differs from the types of inverse analysis described above: rather than using improvements in the measured data or models to predict the response, resulting in the pre-

dictions of material parameters, this thesis aims to modify the tests that produce that measured data so that the material parameters can be more accurately determined. Furthermore, the work in this thesis aims to use an optimization model to change the geometries, boundary conditions and other features of tests, which is similar to the objectives seen in topology optimization. The work in this thesis still differs from any previous works in topology optimization, as the construction of the objective function in this thesis in unique. Detail of this construction is found in Chapter 2.

1.3 Sensitivity analysis

Sensitivity analysis is a vital aspect of the work presented in Track I and has a wide history of use in various fields. Applications specific to this work include assisting optimization and design, for the purpose of more effectively informing optimization, and the understanding of design flexibility. A sensitivity analysis is an indication of how much a change in an input variable will influence the prediction of the function output, and it is typically evaluated only at the location of the desired setup or optimal solution [64, 65]. There are many applications of this process, and particularly relevant to the application proposed here is the field of material parameter determination, where an insensitive parameter can lead to parameter indefinability [66]. Additionally, in the field of robust design and topological sensitivity analysis, the insensitivity of parameters is desirable as higher tolerances can be specified for a final design in robust design and unnecessary sections of a design removed in topological sensitivity analysis [67–70].

The maximization of parameter sensitivity in order to improve material parameter determination is detailed extensively in the computer program MODFLOWP [71]. Maximization is essential as parameter insensitivity leads to insufficient variation in the parameter with given inputs and difficulty estimating the parameter [66]. The focus of this technique is in hydraulic engineering [72–77]; however, it has also been adopted into geotechnical engineering [3, 6, 30–32]. In all of these cases, a sensitivity analysis is used to inform better inverse analysis problems. This consists of selecting the parameters to optimize and informing predictions of initial optimization inputs in the inverse analysis procedure.

Alternatively, there is also a large focus of sensitivity analysis to use minimized sensitivities in the aid of design optimization. Contrary to the maximizing of sensitivities, this area of study is not interested in the determination of parameters, but rather in identifying the parameters or areas of a design which have little to no impact on an output. These parameters or areas can be removed or subjected to increased tolerances with minimal impact on the output. Topological sensitivity analysis or topological sensitivity was first introduced by Eschenauer *et al.* [69]. It aims to optimize the topology of a shape by minimizing a cost function based around the sensitivity of the design to an introduced small defect. Noteworthy works in this area include that by Eschenauer *et al.* [69] and Novotny *et al.* [70]. Another use of minimizing parameter sensitivities is in robust design where parameters of a design, with small sensitivities, can be subjected to greater tolerances with minimal influence on the design performance. When a parameter in the design has a small sensitivity, a greater fluctuation in this parameter will not have a large impact on the output or performance of the design. Other works in this area of research include that by Taguchi *et al.* [67], Park *et al.* [68], and Phadke [78].

All previously mentioned studies incorporate local sensitivity analysis, which computes only the sensitivities related to a single point at a particular time. An alternative to this is global sensitivity analysis. Global sensitivity analysis considers these same influences of parameters across the full range of interest [65]. Kontoravdi *et al.* [79] present work which uses global sensitivity analysis for the design of experiments is particularly applicable to this thesis. By investigating which model parameters have a greater influence on the output, an experiment can be setup to produce more accurate results. While the work by Kontoravdi *et al.* [79] is seemingly similar, it does not construct an optimization model, nor does it investigate minimizing the sensitivity of any parameters. Two global sensitivity methods of note are (1) Morris Sensitivity Method [80] and (2) Sobol Sensitivity Method [81]. However, for the application proposed in this thesis, the significant computational cost to implement these methods make them infeasible to implement [82]. Iooss & Lemaitre [83] present a review of global sensitivity analysis, and their results suggest that for the expected complexity in the sensitivities of the problem presented here, a regression analysis is

recommended, as opposed to a global sensitivity analysis.

The method proposed in Chapter 2 combines parameter sensitivities into a single quantitative metric. The idea of combining sensitivities is known as 'overall sensitivity' and was first proposed by Vajda *et al.* [84]. Vajda *et al.* use a summation of the sensitivities of the objective function to the parameters, in order to determine the most important reaction step of a kinetic model. In Vajda *et al.*'s work, normalization is applied, sum of squared errors used, and weightings can be incorporated to the summation of the sensitivities. These similarities deem Vajda's work noteworthy. However, the implementation of the overall sensitivity differs significantly from the objective of the work presented in this thesis because there is no inclusion of minimizing and maximizing sensitivities, nor is an optimization applied to the sensitivity analysis.

Overall, the field of sensitivity analysis is highly relevant to the work presented in this thesis. Many previous works have influenced and guided the work presented in this thesis, although no work could be found that implemented combined sensitivities to an optimization, which is the fundamental aspect of the work presented in Track I.

1.4 Trafficability, remote sensing, and photogrammetry background

The research presented in Chapter 5 uses the video recordings from cameras mounted to an experimental trailer to reconstruct the rut left by this trailer and infer material strength by comparing rut depth to other material tests. This work has the potential to provide a significant advancement to two key applications: (1) continuous site characterization, and (2) site characterization by novel ground-engaging equipment movements. An application of (1) could allow continuous testing profiles for construction and, in particular, instant feedback of weak areas that need attention during compaction. For (2), by providing the proof of concept that novel ground-engaging equipment movements can infer material strength, models can be developed that can optimize material testing on construction sites or for vehicle mobility. This section covers the relevant areas of research that have informed and assisted in the analysis discussed in Chapter 5. Firstly, the field of trafficability is covered, followed by remote sensing, and finally, photogrammetry.

Much of the current research directly related to vehicles and mobility is focused on extraterrestrial application, given that planetary rovers are unmanned and can cause significant problems if they become immobile. Slightly more related to geotechnical engineering is the area of terramechanics, which is specifically focused on the study of terrain-vehicle systems. The origins of terramechanics are documented by Bekker [85–87] and Wong [88]. Most of the applications in both extraterrestrial rovers and terramechanics are focused directly on mobility characteristics, such as wheel slippage and axle forces, and can be determined using tests such as those developed by Nohse *et al.* [89] and Shmulevich *et al.* [90]. These testing types are very similar to other non-traditional testing methods (further detailed below), in that they are able to determine the near surface parameters of interest at discrete locations. Other works in this field have been included in the following paragraph as they are specifically applicable to remote sensing technology.

Remote sensing, in the context presented here, refers to the retrieval of information about an *in situ* material without any physical contact with that material. This technology makes use of sensors both in the sky and in space and has long been used in the field of earth science for applications such as studying climate change and plate tectonics [91]. Applications in geotechnical engineering date back to 1936 when the U.S. Department of Agriculture's Soil Conservation Service began using aerial photography to examine the land after a major flood on the east coast [92]. Rathje *et al.* [91] give an overview of the application of modern remote sensing in geotechnical engineering and breaks it down into three categories optical imagery, light detection and ranging (LiDAR), and synthetic aperture radar. Optical imagery forms images by detecting the solar radiation reflected by the surface of interest. Applications include using satellites to map the earth's surface and inform on topics such as vegetation coverage and land-use. LiDAR, also known as LaDAR (Laser Detection And Ranging), is the use of lasers to map the topography of an area of interest. It is highly accurate and can be used in applications such as mapping landslides [93], earthquake reconnaissance [94], and excavation monitoring [95]. Furthermore, Manduchi combines a single axis LaDAR with a color stereo camera to present an obstacle detection system for off-road vehicles [96]. Finally, synthetic aperture radar (SAR) is a radar system where the motion of the sensor over the target

creates higher resolution images than a fixed location sensor [97].

Methods to determine the material parameters of *in situ* soils, which require contact with the material but are unlike the traditional *in situ* material testing methods, are referred to here as non-traditional testing methods. As mentioned above, these devices include penetration instruments such as balls, t-bars, and torpedo-like devices [15–17]. Much like traditional testing methods, they are usually only capable of testing in discrete locations and often require repetition to ensure accurate results. Two of the non-traditional testing methods, which are utilized in the work presented in Chapter 5, are the Soilsaber and BlueDrop. The SoilSaber is a miniature vane shear device that gives a digital measurement of shear resistance. This device has been shown to be suitable for a wide range of *in situ* materials, ranging from 0.5 - 500 kPa [98]. The BlueDrop, a free fall penetration device, was originally designed for use underwater on the seabed, but can be used on land by the user lifting and stabilizing the device before allowing it to free fall. The penetration of the BlueDrop can be converted to quasi-static bearing capacity using the method proposed by Stark *et al.* [99]. Both the SoilSaber and BlueDrop are rapidly deployable and provide a good characterization of the *in situ* material. Therefore, they are used as a comparison method in Chapter 5.

A further area of research not known to be associated with traditional remote sensing is photogrammetry. Photogrammetry uses media in the form of images or video to reconstruct a 3D model of the subject matter and therefore is also remote sensing. Much like LiDAR, there are many applications in geotechnical engineering. Zekkos *et al.* [100] provide a thorough overview of the previous uses of photogrammetry in geotechnical engineering. Significant applications include mapping liquefaction [101], landslides [102], and other natural disasters [103]. These works use the models created through photogrammetry to make measurements and to monitor displacements and changes over time.

The work contained in this thesis is unique from all of the areas mentioned above. This work uses photogrammetry as a form of recording test data to provide a continuous profile of material strength. The material tests in terramechanics do not attempt to classify geotechnical material

parameters and are only performed in discrete locations. Similarly, although the non-traditional test methods are more focused on geotechnical material parameters, they are only applicable to discrete locations. The systems described in remote sensing currently have applications in geotechnical engineering, although, none are known to target the assessment of material strength in terms of measurable geotechnical parameters. Finally, photogrammetry is currently used in geotechnical engineering but has no known application in material strength assessment.

1.5 Thesis aims and layout

Scrutiny of previous work reveals that the determination of material parameters has seen significant development in the last century, although little emphasis has been placed on the optimal method to determine the material parameters. The overarching objective of this work is to investigate optimal test methods for soil parameter determination. The work is broken into two distinct tracks.

Track I focuses on mathematically defining an optimal soil test and implementing the proposed quantitative metric analytically and numerically, and includes Chapters 2 to 4. Track II investigates the process of inferring a continuous measurement of material strength and qualitatively assessing the accuracy of material strength determination, and is contained in Chapter 5. It is intended that in the future the proposed quantitative metric, developed in Track I, could be implemented to the work presented in Track II. The specific aims of these tracks are:

1. Determine desirable mechanical test features, and from this devise a quantitative metric that can discriminate between different types of mechanical tests with respect to their ability to recover the true material properties.

2. Provide proof of concept of the ability of this quantitative metric to perform as designed, through analytical implementation.

3. Implement the quantitative metric to finite element analysis and deduce the optimal testing configuration for a given set of constraints.

4. Experimentally investigate a continuous material test method for material strength determination of near-surface soil through an experimental campaign of a towed wheel and wedge.

This thesis is arranged such that each of the above aims is presented as a chapter, and a final chapter is provided to consolidate the conclusions of this work and outline proposed future work (Chapter 6). Furthermore, three appendices complementing the work presented in the main body of the thesis are included. Appendix A contains related preliminary work, and although it formed an alternative track that was discontinued, it is particularly relevant to the work in Chapter 2. The work contained in Appendix A can be found in the proceedings of GeoCongress 2019 [104]. Appendix B outlines the details of the optimization procedure used in Track II and, in particular, the complexities required to complete the analysis in Chapter 4. Finally, Appendix C contains the methodology of the analysis completed in Chapter 5.

CHAPTER 2
PROPOSED QUANTITATIVE METRIC

Traditionally, there are two common ways to obtain soil material parameters when given a data set of experimental or field work—analytically or through empirical correlations. A less common method, increasingly more present in research, is the method of determining material parameters through inverse analysis. In considering any of the material testing methods (analytical, empirical correlations, or inverse analysis), a basic question arises: what is the best test? To begin to answer this question and to specify an optimal test, a mathematical optimization problem must be developed. To construct this optimization problem, the desirable features of a test need to be specified and then quantified. This chapter postulates the desirable features of a material test and, from this, designs a quantifiable metric.

Consider a situation where two engineers are given samples of the same aluminium with the objective of determining the true elastic modulus. Although uniaxial extension would be a natural choice for metals, suppose uniaxial compression and three-point bending tests, classified by ASTM standards E9 [105] and E290 [106], are chosen to determine the elastic modulus. The uniaxial compression test is specifically chosen for its applicability to geotechnical engineering, where compression is of greater interest. The data these engineers collect from these tests is used to compute the elastic modulus of the aluminium. However, regardless of the test they chose, the methodology with which they run it, or the sample geometry, their calculations will almost never match each other or theoretical values. This leads one to consider what must be causing error in their calculation of the elastic modulus when, theoretically, it should be exact. The answer is always the same—errors in the measurements taken, sample differences, and differences between idealized conditions and actual conditions. The elastic modulus of the sample is inclusive of material imperfections, stress history, and heterogeneity. Considering the remaining sources of error, the determination of the optimal test is a function of which test to run, how to run it, and the geometry

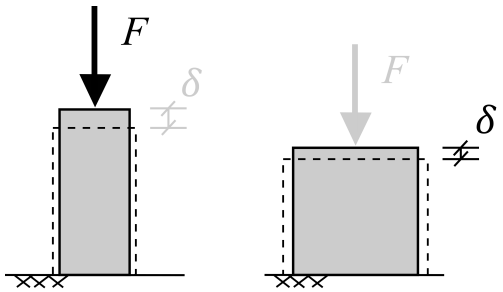

Figure 2.1: Variation of a simple test, highlighting different test type (force, F, and displacement, δ, control) and sample size. Bold action (force or displacement) is applied and greyed action is the recorded measurement.

of the sample. This can be visualized with the two tests presented in Figure 2.1. Both are uniaxial compression tests which are run with two different test methodologies, force and displacement control, and have different sample sizes.

From the example above, the calculation of the elastic modulus would be most accurate when the factors contributing to errors in the test have the least impact on the computation of the elastic modulus. From the two tests presented in Figure 2.1, if the true sample size was smaller or larger than the perceived sample size this would have an impact on the recorded measurement and subsequently on the computation of the material parameter. Furthermore, a test which is less susceptible to the differences in actual and idealized conditions will produce a better calculation of the elastic modulus. For the simple case of uniaxial compression presented in Figure 2.1, the theoretical computation of the elastic modulus is $E = \sigma/\varepsilon$, where σ is stress and ε is strain. However, this assumes no friction, when in reality there is always friction on the ends of the sample.

The axiom posited in this thesis states **the optimal test is the one which can recover the material parameters closest to the true material parameters given potential errors in the test**. This susceptibility of the test output to any potential errors in the test can be modeled using sensitivities. From this, the proposed quantitative metric is derived, with the basic application to the simple tests of uniaxial compression and three-point bending referenced above, in Chapter 3. Note that the derivation of the quantitative metric in the form presented in this thesis is considered a mathematical representation of the above statement, and it is almost impossible to ensure this solution is the best solution without first considering all other possibilities. Although, extensive

efforts have been focused on investigating alternatives. Analyses are shown towards the end of Chapter 3 (Section 3.5) which provide a proof of concept of the intended use by showing that the quantitative metric does indeed present a solution where the material parameter determination is least susceptible to error.

In this work, the optimization problem has been developed to minimize the value of a quantitative metric, Q. The proposed method for measuring test quality through the quantitative metric makes use of a combination of previous techniques found in sensitivity analysis literature. The review presented in Chapter 1 shows that when the sensitivity of a parameter is higher, it is the easiest to discover, and minimizing the sensitivity will lessen any impact a parameter has on the test output. Implementing these minimizations and maximizations will lead to more robust tests which are less susceptible to errors introduced by non-material parameters and have more discoverable material parameters, satisfying the axiom above. This combination of minimizing and maximizing in a minimization optimization allows the sensitivity of some parameters to be minimized while others are maximized. The quantitative metric is intended to encompass all aspects of a test, including but not limited to the test geometry and force-displacement relationship. More specific examples of applications of tests can be found below and in the following chapters.

This work explores a new idea which makes use of features presented in previous works. By maximizing the sensitivity of material parameters, the testing configuration can be specified for the greatest possibility of accurately determining these parameters [66]. Alternatively, the minimization of the constant test parameters works to decrease their influence on the optimization and therefore allow for any associated errors in these terms to have negligible effect on the optimization [67].

The quantitative metric, Q, is proposed and used throughout this thesis. It is a measure of a test's quality and can account for all components of a forward model. It is defined as

$$Q = \frac{1}{n}\sum_{i=1}^{n} w_i \left[\left(\frac{\partial \alpha}{\partial \beta_i}\right)\left(\frac{\beta_{i,avg}}{\alpha}\right)\right]^2 \tag{2.1}$$

where Q is intended to be minimized, n is the number of parameters to be assessed, w_i is the weighting of the i^{th} parameter, α is the output parameter, β_i is a vector of all input parameters, $\partial\alpha/\partial\beta_i$ is a vector of the sensitivities of the output parameter to the input parameters, and $\beta_{i,avg}$ is the average value selected across an expected input parameter range. Negative weightings are added to parameters to be maximized and positive weightings to parameters to be minimized. Furthermore, weightings can be used to manipulate data in a desired way, such as placing greater importance on parameters of more interest or decreasing the influence of parameters deemed unimportant. The quantitative metric is a minimization and therefore adding a negative weighting to a term will minimize the negative of this term, resulting in a maximization of the absolute value of the term. Parameters can be bound within desired limits or individual parameter relationships specified by subjecting the optimization to any desired constraints. With the use of this metric, tests can be compared and new optimal tests developed. Proof of concept for the ability to compare tests is provided for more complex applications in Section 3.5. The selection of the form of the quantitative metric presented in Equation 2.1 is nontrivial, and the following section details the derivation.

2.1 Derivation of the quantitative metric

Each of the components of the quantitative metric presented in Equation 2.1 are explicitly chosen, and the following sections detail how this form is derived from the more general form,

$$Q = \frac{1}{m}\left[\sum_{i=1}^{n} w_i \left[\left(\frac{\partial\alpha}{\partial\beta_i}\right)\left(\frac{\beta_{i,norm}}{\alpha_{norm}}\right)^{p}\right]^{1/q}\right]^{1/r} \tag{2.2}$$

where $\beta_{i,norm}$ is a vector of the input parameter normalization values, α_{norm} is the output parameter normalization, and m, p, q and r are positive integers selected by the user and designed to transform the function. All the input parameters referred to in this analysis are known as decision variables in optimization, and therefore are allowed to be optimized unless otherwise fixed.

In this work, sensitivities are used as the main component to optimize, and their selection is

further discussed in Section 2.1.1. By implementing weights, sensitivities can simultaneously be set to either minimize or maximize, which is also further discussed in Section 2.1.1. The summation includes the overall normalization by m, as well as the exponents p, q and r, which are all individually specified. Details of their selection are presented in Section 2.1.2. The normalization of all the sensitivities (to achieve dimensionless quantities) is achieved with the $\beta_{i,norm}/\alpha_{norm}$ term and is discussed in detail in Section 2.1.3.

2.1.1 Sensitivities and the optimization

The sensitivity is a measure of how much a change in the input will change the output. Positive and negative weightings are applied to the sensitivities and used to minimize and maximize the sensitivities, respectively. By investigating the sensitivity as the measure of the quality of a test, the influence of all aspects of the test on the output can be assessed. Particularly relevant applications of sensitivity to the analysis presented here is the work in robust design and topological sensitivity analysis [68–70], soil and ground-water parameter determination [3, 66, 71], population biology [107, 108], and other environmental modelling applications for ranking, mapping or screening of data [109]. Topological sensitivity analysis uses sensitivities to determine redundant components of a design, which can be removed. Robust design assesses areas that have minimal influence on the design, so design or manufacturing tolerances can be increased. Groundwater and soil parameter determination uses the sensitivities of material parameters to determine which parameters have the greatest influence on the output and therefore are most easily discovered. Finally, population biology and other environmental modelling applications use the sensitivities of animal populations to various events, to investigate the past, present, and future of our natural world. All of the previously mentioned fields of research focus on local sensitivities, which consider only one set of parameters for any given analysis. The implementation of sensitivity analysis presented in this thesis requires the analysis of global sensitivities. In global sensitivity analysis, consideration must be given to the variation of parameters across their respective parameter space. The sensitivity function is used here to refer to the variation of sensitivity across the parameter space.

By maximizing the sensitivity of the output to the material parameters in the analysis, the output of the test will be more sensitive to the material parameters, enhancing their accuracy. Additionally, the simultaneous minimization of the sensitivity of the output to all other components of the forward model reduces their influence on the output. This minimization optimization is achieved by minimizing the value of Q with the terms wished to be maximized given negative weights. The negative weights minimize the negative of these terms resulting in a maximization of the term. Additional weights, not equal to one or negative one, can be added to increase or decrease the significance of particular sensitivities, however these are not addressed further in this work.

2.1.2 Sensitivity combinations in optimization problem

A combination technique is required for the analysis of multiple parameter sensitivities into a single quantitative metric. There are various methods available for which most cases result in similar or the same outcomes of the optimization problem. A selection of options is provided here along with applicable reasoning as to the proposed method.

Firstly, the normalization of the quantitative metric by the number of parameter sensitivities assessed allows for the comparison of quantitative metrics across tests with a varying number of parameters. Therefore, $m = n$ in Equation 2.2 for all of the following applications. The quantitative metric, Q, as a sum of absolute values is achieved in Equation 2.2 when p and q = 2 and r = 1. This method is particularly effective when large and isolated errors are present in a data set [110, 111], although, in this application the forward models are known and free of error. An absolute value is undesirable as it introduces complications for further analytical analysis due to the non-smoothness of the resulting function. Sum-of-squares is achieved with Equation 2.2 when p = 2 and q and r = 1. This method theoretically produces the same result as sum of absolute values with no error present and is especially easy to work with mathematically. Although it does not perform well with outliers in a data set, it has been shown to perform well with a normally distributed error [111]. The square root of sum of squares is achieved using Equation 2.2 when

both p and r = 2 and q = 1. Although commonly used in similar applications [3, 66], this is undesirable for this specific application. The addition of the square root hinders the possibility of using a negative metric in the presence of maximized sensitivities. It is therefore determined that for the application to the quantitative metric, mean sum of squares is the most suitable combination technique, due to the mathematical tractability and the same performance in an optimization with the lack of error, this is reflected in Equation 2.1.

2.1.3 Sensitivity normalization

The parameter sensitivities are dimensional and require a normalization to be correctly summed. The normalization must be achieved without distorting the trends of parameter sensitivity variation across the parameter range, otherwise the normalization would influence the optimization. The various methods considered for the form of the $\beta_{i,norm}/\alpha_{norm}$ normalization term in Equation 2.1 are outlined here with their applicability to the optimization procedure detailed.

Hill [71] normalizes the sensitivity by the input parameter resulting in a normalization term of β_i. In this case, the sensitivity term will remain dimensional, with all terms in the quantitative metric having units of the output parameter and can therefore be summed. Although this method normalizes the sensitivities to have common units, they are not scaled by the input variable. Therefore, a direct comparison is heavily weighted toward the input parameters with larger magnitudes. With the purpose of the optimization to vary the input parameters, the scaling of the sensitivity by the input is not appropriate as the sensitivity function will be distorted by varying normalizations, and made independent of the input parameter.

In the field of population biology, sensitivities are normalized by a multiplication of the input and output parameters, a technique known as elasticity [108]. For application into the quantitative metric, the normalization term becomes β_i/α, not only making the result dimensionless but also scaling such that comparisons are reasonable. However, as with the normalization only by the input parameter presented above, the scaling of the sensitivity by the input is not appropriate to this application of optimization. Alternatively, applying this normalization and making the

sensitivity independent of the output parameter will not influence the results of an optimization. The output factors all sensitivity functions equally, meaning that the combined minimum will occur at the same location, with only the value of the metric scaled by a function of the output. To achieve a normalization of the input parameter, which does not distort the sensitivity function yet still produces a dimensionless metric and scales the sensitivities to comparable magnitudes, the normalization of the input parameter must be constant. Possibilities for the numerator of the normalization term in Equation 2.2 could be equal to the minimum or maximum expected parameter, the range of expected parameters, or the average parameter defined as the midpoint across an expected range ($\beta_{i,norm} = \beta_{i,min}, \beta_{i,max}, \beta_{i,range}, \beta_{i,avg}$, respectively). The average parameter is selected as a viable constant over other constants, as it presents the least variation across the various parameter sensitivity functions. It has particular benefits when the minimum value of a parameter range does not approach zero or the range is very narrow, for example, in the case of a friction angle. All of these terms are considered subjective, and their values should be selected with consideration given to any relevant test apparatus restrictions and general limits on the expected input parameters. Finally, if normalization of the denominator was to also be the average output parameter ($\beta_{i,norm}/\alpha_{norm} = \beta_{i,avg}/\alpha_{avg}$), the quantitative metric becomes dependent on the output parameter, which creates a three-dimensional sensitivity function for all parameters and complicates further calculations. The final normalization term as presented in Equation 2.1 combines a normalization by the output parameter and average input parameter. This creates a quantitative metric that is independent of the output parameter and provides a constant scaling across each of the independent sensitivity functions.

2.2 Spring extension thought experiment

As an explicit example, consider the simple problem of measuring spring constant, k, for a linear spring. Moreover, the analysis based on the proposed quantitative metric aims to answer the following question: if faced with a number of springs of unknown spring constants (Figure 2.2), what is the optimal tests to run on these specimens? In other words, what type of test will most

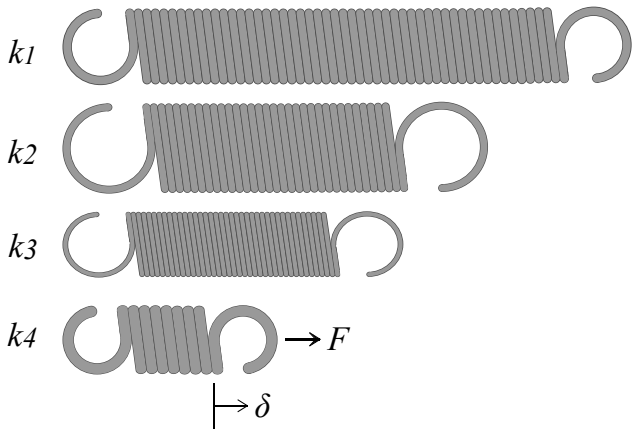

Figure 2.2: Springs of various spring constants (k_1, k_2, k_3, and k_4) determined by imposing/measuring force, F, and displacement, δ.

accurately return the true spring constant?

For the simple case of determining a spring constant, one has a single choice to make: (1) apply a force to the spring and measure the displacement or (2) prescribe a displacement and measure the resulting force. The first option, referred to as a *force-controlled* test, is perhaps the most common for evaluating spring constants. The simplicity of being able to hang weights from a spring and measure the resulting displacement is often easier than attempting to control the displacement and measure the force (e.g., using a load cell), which represents the second choice, a *displacement-controlled* test. The analysis presented in this thesis does not consider the practicality of conducting either force- or displacement-controlled tests and considers only the accuracy to which the spring constant can be calculated. When considering the running of the test, inaccuracy is introduced in one of two ways for a force-controlled test: (1) the measurement of displacement differs from the true value or (2) the prescribed force differs from the intended value. Similarly, for a displacement-controlled test, inaccuracy arises due to errors in either (1) measured force or (2) prescribed displacement. The proposed quantitative metric does not account for other errors present in this test.

The quantitative metric is applied to extension of a spring in order to make a direct comparison of force-controlled and displacement-controlled tests. At this stage it is assumed that force- and displacement-controlled tests can be directly compared, and this is revisited in Section 3.4. Exten-

sion of a spring is used to determine the spring constant, k, and is implemented here to show the comparison of tests in the simplest possible form. The forward model of the spring extension is

$$k = F/\delta \tag{2.3}$$

In an actual test, k is a predetermined unknown constant that is intended to be discovered with the test. If the material parameter were constant in the optimization, the force-to-displacement ratio for the spring extension test would also be constant due to the simplicity of the forward model. Therefore, the optimization of a test with only three components is best analyzed by allowing all components of the test to be variable. In this case, that means that the k, F, and δ are variables in the optimization.

When a spring extension test is run as a displacement-controlled test $\alpha = F$, $\beta_1 = k$ and $\beta_2 = \delta$. The sensitivity of the force to the displacement is minimized to reduce its impact on the output, while the sensitivity of the force to the spring constant is maximized. The resulting quantitative metric is

$$Q_{spring,DC} = \frac{1}{2}\left[-\left(\frac{\partial F}{\partial k}\frac{k_{avg}}{F}\right)^2 + \left(\frac{\partial F}{\partial \delta}\frac{\delta_{avg}}{F}\right)^2\right] \tag{2.4}$$

Equation 2.4 includes the generic form of the sensitivities. At first glance one might be inclined to include the length of the spring, L, in the quantitative metric ($\beta_3 = L$). However, the inclusion of L results immediately in Equation 2.4 as $\partial F/\partial L = 0$.

By substituting the derivatives of the forward model (Equation 2.3) into Equation 2.4, the quantitative metric becomes

$$Q_{spring,DC} = \frac{1}{2}\left[-\left(\delta\frac{k_{avg}}{F}\right)^2 + \left(k\frac{\delta_{avg}}{F}\right)^2\right] \tag{2.5}$$

A further substitution using for the forward model for δ/F and k/F can be made to Equation 2.5

to achieve

$$Q_{spring,DC} = \frac{1}{2}\left[-\left(\frac{k_{avg}}{k}\right)^2 + \left(\frac{\delta_{avg}}{\delta}\right)^2\right] \tag{2.6}$$

Equation 2.6 is particularly significant as it reveals that the optimization model can be analyzed independent of the output parameter and in such a simple form that the trend towards optimal can be seen without an optimization solver. In searching for the optimal test, the objective is to minimize this expression (Equation 2.6). Without implementing parameter bounds to Equation 2.6 the analytical solution will result an infinite δ and a negative k. As k and δ should always be positive constants and within reasonable limits, constraints need to be added to bound the results. It can be seen by assessing Equation 2.6, within a set of constraints, Q will be minimized when k is minimized and δ is maximized, and both k and δ will be pushed to their lower and upper limits, respectively.

For a practical application, k is a fixed property of the spring and this means that the optimal displacement-controlled test should have as large of a displacement as possible. The large displacement will minimize the influence of the displacement on any change in F, and therefore produce the most accurate estimate of k.

For a force-controlled test, $\alpha = \delta$, $\beta_1 = k$ and $\beta_2 = F$. The sensitivity of the displacement to the force is minimized and the sensitivity of the displacement to the spring constant is maximized, as shown

$$Q_{spring,FC} = \frac{1}{2}\left[-\left(\frac{\partial\delta}{\partial k}\frac{k_{avg}}{\delta}\right)^2 + \left(\frac{\partial\delta}{\partial F}\frac{F_{avg}}{\delta}\right)^2\right] \tag{2.7}$$

By substituting the derivatives of the forward model, the quantitative metric becomes

$$Q_{spring,FC} = \frac{1}{2}\left[-\left(\frac{-F}{k^2}\frac{k_{avg}}{\delta}\right)^2 + \left(\frac{1}{k}\frac{F_{avg}}{\delta}\right)^2\right] \tag{2.8}$$

The further substitution for the forward model for F/δ and $1/\delta$ results in

$$Q_{spring,FC} = \frac{1}{2}\left[-\left(\frac{-k_{avg}}{k}\right)^2 + \left(\frac{F_{avg}}{F}\right)^2\right] \tag{2.9}$$

The sequence of Equations 2.7 to 2.9 follows the same as presented for displacement control, with Equation 2.9 making the critical substitution, which shows a simplification of the optimization and independence of the output parameter. The optimal configuration for a force-controlled test can be determined through the minimization of Q in Equation 2.9. As with displacement control, without the implementation of constraints there is no reasonable analytical solution. Although once implemented it can be seen that the ideal test will occur when k is minimized and F is maximized. Similar to displacement control, for a practical application when k is constant, a large force will minimize the sensitivity to displacement, resulting in the optimal test. In both force and displacement control cases a test of constant k can be improved by increasing the applied force and displacement.

For the purpose of this chapter, force- and displacement-controlled tests will be compared directly. The justification supporting the ability to make this comparison, is provided in Chapter 3 (Section 3.4). The comparison of Equations 2.5 and 2.9 can be used to determine the preferred material test, force control or displacement control. A displacement-controlled test is preferred when

$$Q_{spring,DC} < Q_{spring,FC} \tag{2.10}$$

By substituting Equations 2.5 and 2.9 into Equation 2.10, the expression becomes

$$\frac{1}{2}\left[-\left(\frac{k_{avg}}{k}\right)^2+\left(\frac{\delta_{avg}}{\delta}\right)^2\right] < \frac{1}{2}\left[-\left(\frac{k_{avg}}{k}\right)^2+\left(\frac{F_{avg}}{F}\right)^2\right] \tag{2.11}$$

By rearranging the equation and substituting Equation 2.3, the expression simplifies to

$$k < F_{avg}/\delta_{avg} \tag{2.12}$$

It can be seen that the use of force or displacement control is dependent on the comparison of the spring constant to the average force and displacement values, as presented in Equations 2.10 to 2.12. This result is possible due to the normalization of sensitivities creating a quantitative metric

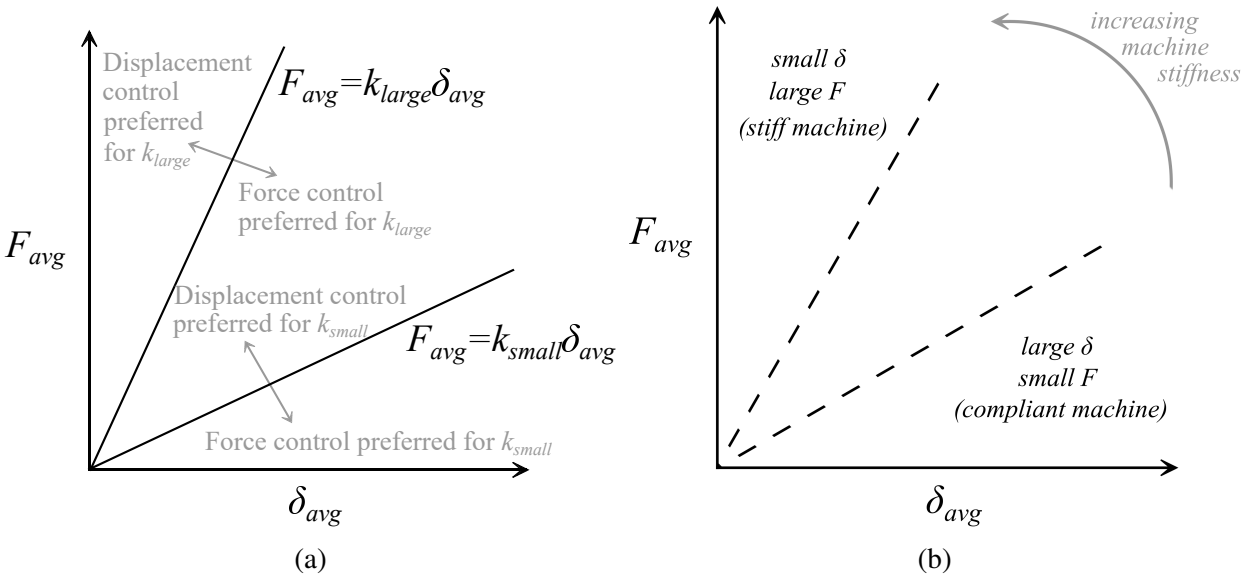

Figure 2.3: Spring Extension Analysis: (a) force vs displacement control comparison; (b) testing machine properties comparison.

that is independent of the output. The significant contribution of the substitution made to get from Equation 2.5 to 2.6 and Equation 2.8 to 2.9 results in the comparison of force- and displacement-controlled tests subsequently becoming only a comparison of the sensitivity of force to displacement and displacement to force. Equation 2.12 suggests that in order to determine which test is preferable, one must first know critical details about the testing machine, including the average force and displacement values and the spring stiffness. In other words, it is not possible to take an unknown spring and specify an optimal test with no prior knowledge. A machine capable of applying small displacement and measuring large force is good for springs with high stiffness, as depicted in Figure 2.3. A machine capable of applying small force and measuring large displacement is good for springs with low stiffness (Figure 2.3). Importantly, Equation 2.12 shows that as the spring constant decreases the more likely it is that one should run a displacement-controlled test. Alternatively, as the spring constant increases the more likely it is that one should run a force-controlled test (Figure 2.3).

By assessing the springs in Figure 2.2, assuming they are the same material, the spring of k_1 would likely have a lower k than that of k_3. The first spring would be best assessed with displacement control as its lower k presents a higher probability that displacement control would

be preferred. This is indicated in Figure 2.3b by a lower k having a much greater area of the Figure with displacement control preferred. For the third spring, with a higher k_3, there is a larger probability that force control will present a better test, therefore, there is a higher possibility that force control will be the preferable test.

2.3 Concluding remarks

The proposition is made that the optimal test is the one where the material parameter is most sensitive and the test is least susceptible to error generated by other parameters. From this, the quantitative metric, Q, is derived. The quantitative metric of Equation 2.1 is carefully constructed with justifications for each component given.

The simple example of spring extension highlights that conclusions can be drawn as to the selection of test and ideal testing configuration. With the selected normalization method, the choice to run a force-controlled or displacement-controlled test rests on comparing the average force to displacement ratio, F_{avg}/δ_{avg}, and the spring constant, where the force-to-displacement ratio presented here is a representation of machine stiffness. The smaller the spring constant, the more likely a displacement-controlled test will be preferred, and as the spring constant increases, so does the probability that a force-controlled test will be preferred. When assessing the force- and displacement-controlled tests individually, the quantitative metric will be lower when a lower spring constant is specified. For the case of a displacement-controlled test, the objective is to minimize the sensitivity of the displacement with respect to the force resulting in a large force. Alternatively, in a force-controlled test, the objective is to minimize the sensitivity of force with respect to displacement, resulting in a preferred large displacement.

CHAPTER 3
APPLICATION OF QUANTITATIVE METRIC TO SIMPLE PROBLEMS AND PROOF OF CONCEPT

In this chapter, examples are presented to provide proof of concept and serve as an explanatory tool for ease of understanding the concepts and intended uses of comparing material parameter tests with the quantitative metric presented in Chapter 2. The examples are specific to civil engineering, but this method can be applied to any application of an optimization or comparison procedure. The examples presented here are a calculation of the material's elastic modulus, E, and include uniaxial compression, three-point bending, and four-point bending. The following sections of this chapter interrogate the meaning of Q, applied to these simple problems. A representation of these tests is shown in Figure 3.1.

The introduction of the uniaxial compression, three-point bending, and four-point bending tests adds geometric parameters to the problem. Now, in addition to the consideration of force and displacement control, each is assessed based on the contributions of sample geometry to Q. Similarly to Chapter 2, in the assessment of Q and all optimizations, the sensitivities of all non-material parameters are minimized by applying a weight of 1, and all the sensitivities of material parameters are maximized by applying a weight of -1.

Material tests must be run as force- or displacement-controlled tests with displacement or force

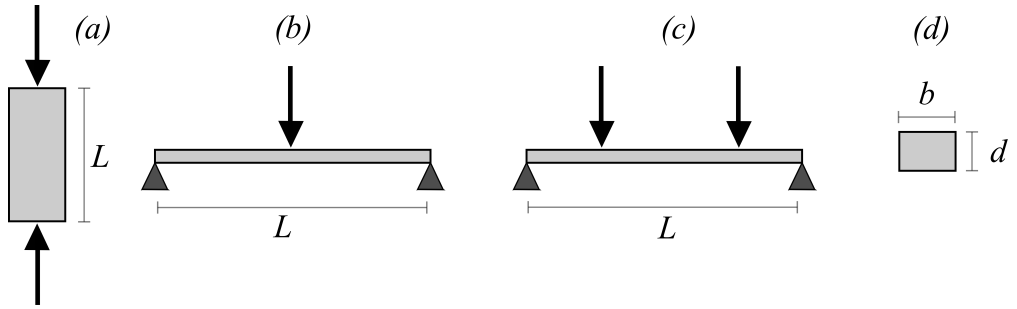

Figure 3.1: Simple tests: (a) uniaxial compression; (b) three-point bending; (c) four-point bending; (d) the sample cross-section.

as the test output, respectively. The three tests presented in Figure 3.1 have known forward models for the computation of elastic modulus. The forward model for a displacement-controlled uniaxial compression test is

$$F = \frac{E\delta bd}{L} \tag{3.1}$$

where F is the force applied (N), E is the elastic modulus (MPa), δ is the sample displacement (mm), L is the sample length (mm), b is the sample width (mm) and d is the sample depth (mm). The forward model for a displacement-controlled three-point bending test is

$$F = \frac{4E\delta bd^3}{L^3} \tag{3.2}$$

Finally, the forward model for a displacement-controlled four-point bending test is

$$F = \frac{4E\delta bd^3}{L^3 a\left(3 - a^2\right)} \tag{3.3}$$

where a is an additional parameter in the four-point bending test, used to specify the distance of the force from the support. The value of a can be computed as $a = 2x/L$, where x is the distance of the force from the support. In this case a has been implemented such that it is a unit-less fraction of the distance from the support (a = 0) to midpoint (a = 1). Units are included throughout this analysis as they have significance to the practical application and in the sense of dimensional error considerations (see Section 3.5). Both force- and displacement-controlled tests are considered in the following subsections. The selection of the uniaxial compression, three-point bending and four-point bending tests is made due to their common use and the minimal justification which exists for their selection, in terms of which test and configuration to select. Additionally, parameters across the forward models are very similar and therefore direct comparisons are made between the tests.

Further analysis of the uniaxial compression test is in Section 3.1, and three- and four-point bending tests are considered in Section 3.2. Section 3.3 implements a cantilever beam model to show the added complexity with two material parameters, and Section 3.4 makes comparisons

between the test configurations and material testing methods. Section 3.5 provides empirical proof of concept of the ability to compare tests, presented through a probabilistic error analysis that compares computed Q values to the accuracy of a material parameter computation subjected to error. Finally, Section 3.6 provides concluding remarks.

3.1 Detailed analysis of uniaxial compression

A uniaxial compression test consists of the axial deformation of a sample and is specifically used for the computation of the elastic modulus, E. For the analysis presented here, the imposed deformation on the sample is assumed to remain within the elastic region of the material. The forward model presented for the uniaxial compression test (Equation 3.1) is used for the determination of E, and graphically this is computed as the slope of the elastic portion of a stress-strain curve. The focus of this chapter is on the determination of an ideal testing configuration for the most accurate computation of the material parameter, E. The testing configuration for a uniaxial compression test can be defined as the sample geometry (L, b and d) and the force/displacement relationship (F and δ). Consideration is given to both force- and displacement-controlled testing configurations.

National standards give directions for testing configurations of various uniaxial compression tests. Within the United States a select few include ASTM E9 (for the uniaxial compression testing of metals), ASTM D2166 [112], ASTM D4767 [113] and ASTM D7181 [114] (for the triaxial testing of soils). All of these documents recommend sample sizes ranging from aspect ratios of L/b = 1.5 – 2.0 (ASTM E9) for metals to 2 – 2.5 for soils (ASTM D2166). These documents provide little to no reasoning as to the selection of sample size, although, elsewhere it is outlined that these specific sizes are selected to ensure the failure mode remains within the desired mode. Darvell [115] provides a detailed review of the uniaxial compression test with an emphasis on slenderness ratios (L/b). Furthermore, ASTM E9 implies that displacement-controlled is preferred, by referencing only the desired strain rates to be applied. Although, no comparison or justification is addressed within ASTM E9. The methodology presented in this chapter aims to provide justification as to the selection of an optimal testing configuration through the implementation of Q. Note that for

Table 3.1: Parameter bounds.

Parameter	Lower bound ($\beta_{i,min}$)	Upper bound ($\beta_{i,max}$)	Average ($\beta_{i,avg}$)
E (MPa)	200	20,000	10,100
F (N)	100	10,000	5,050
δ (mm)	5	200	102.5
b (mm)	10	400	205
d (mm)	10	400	205
L (mm)	20	500	260

the work presented in this chapter, all tests are assumed to remain purely elastic, although any desired constraints specific to a problem can be implemented into any of the optimization problems presented here.

3.1.1 Uniaxial compression: parameter sensitivities

The methods proposed in this chapter use the quantitative metric, Q, proposed in Chapter 2, to optimize the combined parameter sensitivities to specify an optimal testing configuration. In order to investigate the parameter sensitivities, each of the parameters in the uniaxial compression test (E, F, δ, b, d, L) are bounded by upper and lower limits, as shown in Table 3.1. The selection of these bounds is to represent a reasonable set of values for physical upper and lower bounds of a test which could realistically be conducted in a laboratory. The selected values appear to have minimal significance beyond their physical meaning. However, they are essential, as without bounds the optimization will return unrealistic values (negative parameters, zero, or infinity), as shown through further investigation in this Section 3.1.3.

The individual variation of normalized sensitivity of each individual parameter across the normalized parameter range is calculated with

$$S_i = \left(\left(\frac{\partial \alpha}{\partial \beta_i} \right) \left(\frac{\beta_{i,avg}}{\alpha} \right) \right)^2 \tag{3.4}$$

where S_i a vector of the normalized parameter sensitivities representing the individual normalized

sensitivity components within Q. The quantity $\beta_{i,avg}$ is a vector of the arithmetic average of the upper and lower bounds of each parameter. For the case of a displacement-controlled uniaxial compression test, $\alpha = F$ and $\beta = [E, \delta, b, d, L]$. For a force-controlled test, $\alpha = \delta$ and $\beta = [E, F, b, d, L]$.

For the purpose of demonstrating the implementation of parameters to the normalized sensitivity, a displacement-controlled uniaxial compression test (Equation 3.1) is implemented to Equation 3.4, for the parameter L. This results in

$$S_L = \left(\left(\frac{\partial F}{\partial L} \right) \left(\frac{L_{avg}}{F} \right) \right)^2 \tag{3.5}$$

The substitution for the partial derivative results in

$$S_L = \left(\left(\frac{-E\delta bd}{L^2} \right) \left(\frac{L_{avg}}{F} \right) \right)^2 \tag{3.6}$$

where the negative is eliminated by the square. A further substitution is made for the forward model to the left-hand fraction, $F = E\delta bd/L$, resulting in

$$S_L = \left(\frac{L_{avg}}{L} \right)^2 \tag{3.7}$$

This final form of the normalized sensitivity is particularly significant as the value is not dependent on any of the other test parameters. All other normalized sensitivities can be computed the same way and are presented in the assessment of Q in Equations 3.8 to 3.9.

To visualize the normalized sensitivities, they are plotted against the range of each of the parameters. The range of all the parameters are also normalized to fall on a zero to one scale, in order to plot them together. As shown above, the normalization applied to the sensitivities causes the parameters to be independent of the output of the function and this means they are also independent of the type, force or displacement control. The variation of parameter sensitivity over the parameter range is shown in Figure 3.2, where both terms are normalized in different ways. The parameters

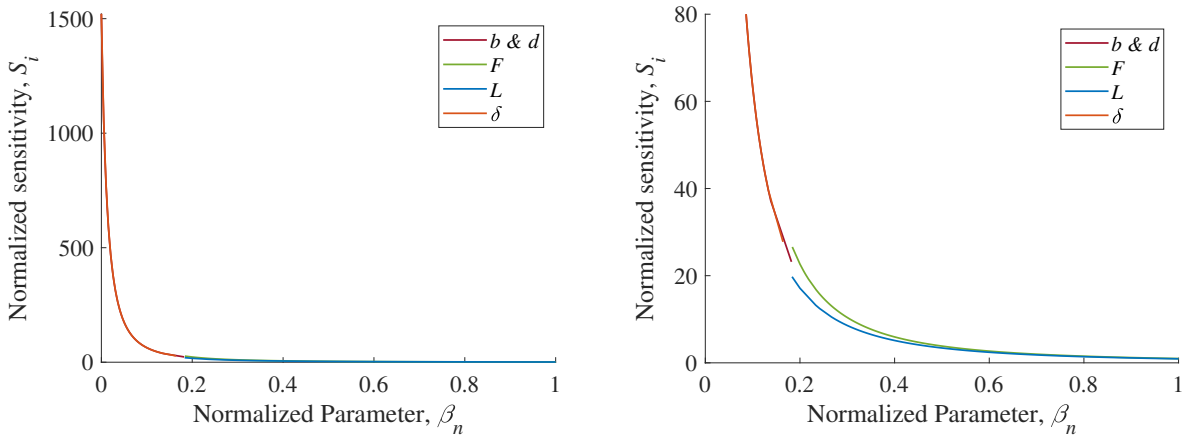

Figure 3.2: Uniaxial compression parameter sensitivities: (a) full range of S_i; (b) highlighted range of S_i.

are normalized as $\beta_n = (\beta_i - \beta_{i,min})/(\beta_{i,max} - \beta_{i,min})$, and the normalization of the sensitivities is presented in Equation 3.4.

By assessing Figure 3.2a, it seems that all of the parameters have the same trend of S_i vs β_n. Sensitivity approaches zero as the parameter increases, and maximum sensitivity occurs at the minimum parameter value. Figure 3.2b shows that there are minor differences in the plots. The line for b and d is not visible as it corresponds exactly to that of δ. The discontinuation of the plots, F and L less than approximately β_n = 0.2 and δ as the line approaches β_n = 0.2, is due to there being no feasible configuration within the specified parameter bounds to satisfy these areas. Using Q to assess the quality of a test, this plot shows that in all cases it is desirable to maximize the parameter values—minimizing their normalized sensitivities. Maximizing all parameters is not possible as the test must conform to the forward model. The process of optimizing Q will find a compromise of the combined S_i's which both satisfy the forward model (Equation 3.1) and minimizes Q. At this point the optimization becomes sufficiently complex and an optimization solver is required.

3.1.2 Uniaxial compression: implementation of the quantitative metric

To combine the uniaxial compression sensitivities into a single quantitative metric, the forward model for uniaxial compression, presented in Equation 3.1, is substituted into the quantitative

metric (Equation 2.1). For the case of a displacement-controlled test, this results in

$$Q_{u,DC} = \frac{1}{5}\left[-\left(\frac{\partial F}{\partial E}\frac{E_{avg}}{F}\right)^2 + \left(\frac{\partial F}{\partial \delta}\frac{\delta_{avg}}{F}\right)^2 + \left(\frac{\partial F}{\partial b}\frac{b_{avg}}{F}\right)^2 + \left(\frac{\partial F}{\partial d}\frac{d_{avg}}{F}\right)^2 + \left(\frac{\partial F}{\partial L}\frac{L_{avg}}{F}\right)^2\right] \tag{3.8}$$

As before, here the weights are set at one for the parameters which sensitivities are intended to be minimized and negative one for the sensitivity of the material parameter, E, so it is set to maximize. This setup assumes that E, is a parameter one wants to determine and all other parameters in the forward model are constants within the test, meaning their variation should have a minimal influence on the optimization. A further substitution for the derivatives is made into Equation 3.8, giving

$$Q_{u,DC} = \frac{1}{5}\left[-\left(\frac{\delta bd}{L}\frac{E_{avg}}{F}\right)^2 + \left(\frac{Ebd}{L}\frac{\delta_{avg}}{F}\right)^2 + \left(\frac{E\delta d}{L}\frac{b_{avg}}{F}\right)^2 + \left(\frac{E\delta b}{L}\frac{d_{avg}}{F}\right)^2 + \left(\frac{-E\delta bd}{L^2}\frac{L_{avg}}{F}\right)^2\right]$$

An additional substitution of the forward model (Equation 3.1) can be made for each of the terms above, resulting in

$$Q_{u,DC} = \frac{1}{5}\left[-\left(\frac{E_{avg}}{E}\right)^2 + \left(\frac{\delta_{avg}}{\delta}\right)^2 + \left(\frac{b_{avg}}{b}\right)^2 + \left(\frac{d_{avg}}{d}\right)^2 + \left(\frac{L_{avg}}{L}\right)^2\right] \tag{3.9}$$

Equation 3.9 is of particular significance as this Q is independent of output (F), and this simple form can be easily manipulated and compared. Note the negative derivative for the L term is removed, as the squaring of the term makes this negative irrelevant.

To apply to a practical example, consider two samples of the same aspect ratio, presented in Table 3.2, both tested under displacement-controlled conditions. Both tests presented in Table 3.2 have the same E and F values and different values for δ, b, d and L. Test 1 has a larger sample, meaning b, d and L have smaller sensitivities and contribute to Test 1 having a lower Q, deeming it a better test. This is intuitive as the larger a measurement, the less absolute error it will

Table 3.2: Displacement-controlled test, variable sample size for E = 200 MPa and F = 1000 N.

Test #	δ (mm)	b (mm)	d (mm)	L (mm)	S_E	S_δ	S_b	S_d	S_L	Q_{DC}
1	6.3	20	20	500	2550	269	105.1	105.1	0.3	-467.9
2	12.5	10	10	250	2550	67.2	420.3	420.3	1.1	-341.7

attract. Therefore in the case of Test 1, b, d and L will have a lesser impact on the variability of F. Alternatively, δ is smaller in Test 1, therefore contributing to a lesser quality test, as defined by Q, although the negative impact is outweighed by the other factors.

To consider the alternative method of running a test, a force-controlled test is now implemented to Q. For the case of a force-controlled test, Equation 3.1 is rearranged for δ as the subject, and substituted into Equation 2.1, resulting in

$$Q_{u,FC} = \frac{1}{5}\left[-\left(\frac{\partial\delta}{\partial E}\frac{E_{avg}}{\delta}\right)^2+\left(\frac{\partial\delta}{\partial F}\frac{F_{avg}}{\delta}\right)^2+\left(\frac{\partial\delta}{\partial b}\frac{b_{avg}}{\delta}\right)^2+\left(\frac{\partial\delta}{\partial d}\frac{d_{avg}}{\delta}\right)^2+\left(\frac{\partial\delta}{\partial L}\frac{L_{avg}}{\delta}\right)^2\right] \tag{3.10}$$

As with the implementation for a displacement-controlled test, all weights are set to one except for the sensitivity of E, which has a weight of negative one. A substitution for the derivatives is made into Equation 3.10, giving

$$Q_{u,FC} = \frac{1}{5}\left[-\left(\frac{-FL}{E^2bd}\frac{E_{avg}}{\delta}\right)^2+\left(\frac{L}{Ebd}\frac{F_{avg}}{\delta}\right)^2+\left(\frac{-FL}{Eb^2d}\frac{b_{avg}}{\delta}\right)^2+\left(\frac{-FL}{Ebd^2}\frac{d_{avg}}{\delta}\right)^2+\left(\frac{F}{Ebd}\frac{L_{avg}}{\delta}\right)^2\right]$$

Finally, an additional substitution of the forward model is made to each of the terms resulting in

$$Q_{u,FC} = \frac{1}{5}\left[-\left(\frac{E_{avg}}{E}\right)^2+\left(\frac{F_{avg}}{F}\right)^2+\left(\frac{b_{avg}}{b}\right)^2+\left(\frac{d_{avg}}{d}\right)^2+\left(\frac{L_{avg}}{L}\right)^2\right] \tag{3.11}$$

As with Equation 3.8, the significance of Equation 3.11 is that Q is independent of output (in this

case δ) and can be easily manipulated and compared.

The construction of Q facilitates the comparison of tests across their specific forms, such as $Q_{u,DC}$ and $Q_{u,FC}$. Empirical proof of the ability to compare the force- and displacement-controlled Q's is provided in Section 3.4. Here Equations 3.8 and 3.11 are compared directly, such that a displacement-controlled test is preferred when $Q_{u,DC} < Q_{u,FC}$, or

$$\begin{aligned} \frac{1}{5}\left[-\left(\frac{E_{avg}}{E}\right)^2+\left(\frac{\delta_{avg}}{\delta}\right)^2+\left(\frac{b_{avg}}{b}\right)^2+\left(\frac{d_{avg}}{d}\right)^2+\left(\frac{L_{avg}}{L}\right)^2\right] \leq \\ \frac{1}{5}\left[-\left(\frac{E_{avg}}{E}\right)^2+\left(\frac{F_{avg}}{F}\right)^2+\left(\frac{b_{avg}}{b}\right)^2+\left(\frac{d_{avg}}{d}\right)^2+\left(\frac{L_{avg}}{L}\right)^2\right] \end{aligned} \tag{3.12}$$

This inequality simplifies to

$$\frac{F}{\delta} \leq \frac{F_{avg}}{\delta_{avg}} \tag{3.13}$$

Equation 3.13 indicates that a displacement-controlled test is preferable when the force-to-displacement ratio (F/δ) is smaller than the average force divided by the average displacement. As can be seen from this relationship, it is not possible to determine the preferred test, force or displacement control, without first knowing values of F_{avg} and δ_{avg}. The range of the testing device, specified by F_{avg}/δ_{avg}, and the stiffness of the material will dictate the choice between a force- or displacement-controlled test. Since $F/\delta = Ebd/L$, for the same sample geometry (b, d, L) a displacement-controlled test tends to be optimal for a less stiff material, whereas a force-controlled test tends to be optimal for a stiffer material. When a less stiff material is tested in a force-controlled test, a minimal perturbation in the force, denoted as ΔF, will induce a large change in the displacement, denoted as $\Delta\delta$, and the sensitivity of δ to F will be high, increasing the susceptibility of the test to error. Alternatively, in a displacement-controlled test of the same sample, $\Delta\delta$ will cause minimal change in the output, ΔF, and therefore have less influence on the calculation of E. This is the same result that was presented for the case of spring extension in Chapter 2.

3.1.3 Uniaxial compression: optimization through minimizing Q

To investigate the application of Q further, it must be cast as an optimization problem. For a displacement-controlled test, this is

$$\begin{aligned}
\min_{F,\delta,b,d,L} Q_{u,DC} =& \frac{1}{5}\left[-\left(\frac{E_{avg}}{E}\right)^2+\left(\frac{\delta_{avg}}{\delta}\right)^2+\left(\frac{b_{avg}}{b}\right)^2+\left(\frac{d_{avg}}{d}\right)^2+\left(\frac{L_{avg}}{L}\right)^2\right] \\
& s.t.\ 100 \leq F \leq 10,000 \text{ N} \\
& s.t.\ 5 \leq \delta \leq 200 \text{ mm} \\
& s.t.\ 10 \leq b \leq 400 \text{ mm} \\
& s.t.\ 10 \leq d \leq 400 \text{ mm} \\
& s.t.\ 20 \leq L \leq 500 \text{ mm} \\
& s.t.\ E = \frac{FL}{\delta bd}
\end{aligned} \tag{3.14}$$

The optimization problem presented in Equation 3.14 is a minimization of the Q presented in Equation 3.9. The optimization is subject to (s.t.) constraints for the material parameter bounds (found in Table 3.1), and the final constraint listed is compliance with the forward model (Equation 3.1). The optimization problem for a force-controlled test is similar to that presented in Equation 3.14, with the substitution for Equation 3.11 in place of Equation 3.9. The material parameter, E, is kept constant in all cases to simulate the design of a test for a specific material type, and all other parameters are optimized by the solver. The solver used in this chapter, with the exception of Section 3.3, for all optimizations is BARON [116], run by AMPL [117]. Note that this solver is not used in all chapters of this thesis which apply optimization solvers, specifically for this chapter Section 3.3 uses KNITRO [118] run by MATLAB for all optimizations, and the reasoning for this is detailed in Appendix B.

Further constraints could be placed on the optimization model to ensure compliance with specific failure modes. For example, if buckling is of concern, the optimization model can be modified

such that the applied force remains less than the critical force (F_{cr}) as computed using Euler's critical load formula,

$$F_{cr} = \frac{\pi EI}{(KL)^2}$$

It is the intention of this chapter to present the methodology and comparisons of implementing Q across various simple tests. This analysis assumes that the material remains within the elastic region in all considered tests, and therefore failure conditions are irrelevant here. The inclusion of any failure conditions would further complicate a already complex analysis. For these reasons, additional constraints (not already listed in Equation 3.14) to ensure compliance with the failure mode are not considered here, and the constraints listed above are constant across all tests and configurations considered in this chapter, aside from the varying forward model.

Optimal configurations for varying E values, computed with the set up in Equation 3.14, are presented in Table 3.3. The results presented in Table 3.3 are significant as they show the complexities that arise in the optimization problem with even such a simple forward model. Each of the columns present an individual optimization. Consider, for example, the optimizations for E = 200 MPa. It was shown in Section 3.1.1 that in all cases a larger parameter leads to a smaller normalized sensitivity, so with the objective of minimizing Q, the normalized sensitivity of all non-material parameters should be maximized. For the force-controlled test, the resulting objective is to maximize the applied force and maximize the size of the sample. Even once F reaches its upper bound, the sample can continue to grow, by decreasing δ to ensure compliance with the forward model. The only constraints that are placed on δ, as the output of the test, are the predetermined parameter bounds.

The assessment of the displacement-controlled test is at first counter-intuitive, as it does not simply reverse the trends of the force-controlled test. The fundamental objective of the displacement-controlled test is to maximize the applied displacement and the size of the sample. However, this creates competing objectives, as maximizing the displacement and sample size both require a larger force, and this cannot be facilitated for a constant E. The result is a compromise between the sample size and displacement. Most significantly, the optimal configurations for both force-

Table 3.3: Optimal configurations in uniaxial compression for force- and displacement-controlled tests. Bold text indicates values kept constant in the optimization.

	Displacement control			Force control		
	1	2	3	1	2	3
E (MPa)	**200**	**1,000**	**5,000**	**200**	**1,000**	**5,000**
F (N)	10,000	10,000	10,000	10,000	10,000	10,000
δ (mm)	18.4	10.8	6.5	5	5	5
b (mm)	36.8	21.5	12.6	70.7	31.6	14.1
d (mm)	36.8	21.5	12.6	70.7	31.6	14.1
L (mm)	500	500	500	500	500	500
Q	-473.2	34	158.1	-506.6	-3.5	83.3

and displacement-controlled tests result in a maximized F, and δ is well below δ_{avg}. This means that Equation 3.13 is not satisfied for this problem, and a force-controlled test is always preferred. This is in contradiction of the previously mentioned ASTM standards, which use displacement-controlled tests. The contradiction is understandable given that the ASTM standards consider the practicality of running a test, and the comparison in this work does not.

More generally, for all optimizations presented in Table 3.3, both the force and sample length are optimized to their maximum every time for both force and displacement control. In all cases of force-controlled tests, δ = 5 mm (the minimum value), and only b and d appear to optimize. The constant δ is due to displacement not being a sensitivity that is optimized for force control (it is the dependent variable of the forward model), and minimizing δ allows other variables such as b and d to increase. Alternatively, for the case of displacement control, the displacement sensitivity is included in the optimization model, and therefore it is not equal to the minimum every time. For the models and constraints specified, no analytical solution could be found, with or without bounds to constrain the problem.

As can be seen from the comparison of the optimal solutions in Table 3.3 and the parameter bounds in Table 3.1, all of the specified optima lie on the upper boundary of the F and L parameters. Without bounds, limiting the solution only by ensuring positive parameters, F and L become increasingly large while δ, b and d increase to ensure compliance with the forward model. There-

fore, bounding the parameters to reasonable limits is necessary to ensure a practical testing setup. Table 3.4 presents the optimization of a displacement-controlled test with variable boundaries, for E = 1000 MPa, corresponding to the second case for displacement control in Table 3.3. With an increase in the upper bound, F and L continue to fall on the upper bound while δ, b and d experience slight increases. This shows that the bounds selected for this analysis do not influence the trends of the optimization.

The values of the parameters in the optimal configurations can be systematically explained through the analysis of the forward model (Equation 3.1). A critical feature of the optimization is the requirement to comply with the forward model, in the form where E is the subject. This point is significant, as all of the trends in the optimized configurations can be explained relative to the positioning of the parameters in this version of the forward model. Consider a displacement-controlled test, where E is constant. The sensitivity of F is not optimized but the value of F is allowed to change, and all other sensitivities are optimized. When E is a the subject of the forward model, F is on the numerator, meaning that maximizing F will allow δ, b and d to be larger. As larger parameters correspond to lower sensitivities (Figure 3.2), this is desirable. Maximizing L to its limit has the same effect on δ, b and d as F does, and therefore is also beneficial in minimizing the sensitivity of L. Furthermore, δ, b and d cannot be maximized due to their position on the denominator and the requirement of a constant E. Then, δ is different from b and d due to differences in the bounds and normalizations. Variables δ, b and d are optimized to as large as they can be whilst still complying with the constant E. A similar analysis can be made for force-controlled tests and most notably, the sensitivity of δ is not optimized. However, the value is allowed to change. With δ, b and d all in the denominator, the result is a minimization of δ so as the values of b and d can be larger and have smaller sensitivities. A practical analysis of each individual parameter would result in maximizing all the input parameters for which one wishes to have minimal influence. Since a small error will have a larger impact on a small parameter when compared to the same error placed on a larger parameter. This analysis does not apply here due to the constraint of a constant E, therefore, parameter values need to be compromised.

Table 3.4: Impact of bounds in uniaxial compression for displacement-controlled tests. Bold text indicates values kept constant in the optimization.

	Original bounds	5% increase in upper bound	10% increase in upper bound	50% increase in upper bound	100% increase in upper bound	Bounded* > 0
E (MPa)	**1,000**	**1,000**	**1,000**	**1,000**	**1,000**	**1,000**
F (N)	10,000	10,500	11,000	15,000	20,000	7.03E8
δ (mm)	10.8	11.1	11.5	14.1	17.1	5E4
b (mm)	21.5	22.3	23	28.2	34.2	9.9E4
d (mm)	21.5	22.3	23	28.2	34.2	9.9E4
L (mm)	500	525	550	750	1000	7.03E8
Q	34	33.6	33	24.5	3.4	-20.4

*optimal not found, greater than 250,000 iterations, CPU time reached.

When viewed from a physical stand point these results make sense. Consider a displacement-controlled test, here is no negative impact on any other parameter of increasing the L. With a larger L, the δ or the cross-sectional area (b x d) could increase for the same F and E. Alternatively, increasing the cross-sectional area (assuming L and F are already maximized) requires a decrease in δ, negatively impacting the Q with an increase in the sensitivity of δ. Furthermore, F is not optimized but allowed to change and a maximized F can facilitate both a larger δ and/or a larger cross-sectional area, both of which are beneficial to the Q. As with the mathematical approach, force control is very similar when assessing practicality, with the notable difference being that the sensitivity of δ is not optimized. A change in δ has not impact on the Q and facilitates a larger cross-sectional area, which is beneficial. Finally, in all cases the larger values are desirable because consider a sample with a slightly longer length than expected, this will have a greater impact on a smaller originally length.

3.1.4 Uniaxial compression: analysis for optimal configuration

Finally, to investigate the effect of sample aspect ratio and its influence on Q, Figure 3.3 presents the trend of the quantitative metric, Q, with a varying slenderness ratio, L/b and for select values of F/δ. The force-to-displacement ratio, F/δ, is essentially sample stiffness. For this analysis,

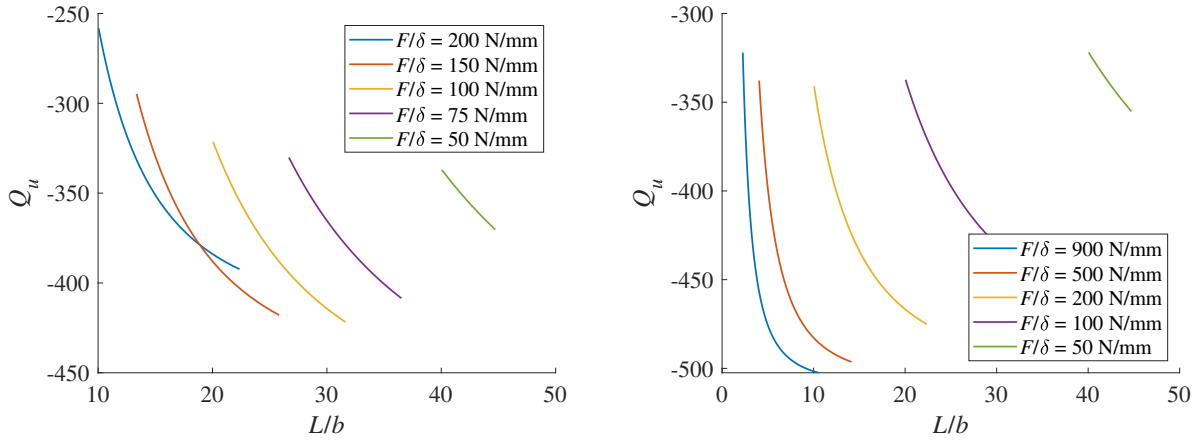

Figure 3.3: Impact of slenderness ratio on test quality for uniaxial compression: (a) displacement control; (b) force control.

E = 200 MPa and $d = b$. In all cases, for both force and displacement control, a more slender sample is more desirable, giving a significantly lower test quality with an increasing slenderness ratio. With the exception of highest F/δ relationship in the displacement-controlled test, as L/b increases Q does not decrease at the same rate of lower F/δ relationships. A decrease in F/δ indicates a more easily deformed sample, and with a constant E this must be achieved through a more slender sample. The F/δ values are selected by setting δ constant in displacement control and F constant in force control, and then selecting a representative range of the other parameter, F or δ respectively.

3.2 Detailed analysis of three- and four-point bending

Similar to uniaxial compression, both the three- and four-point bending are assessed for the most accurate way to determine the elastic modulus, E, by implementing the quantitative metric, Q as proposed in Chapter 2. Both the three- and four-point bending tests consist of a simply supported beam with one (three-point) or two (four-point) loads applied. The magnitude of the deflection of the beam, taken at the midpoint, is used to compute E with the forward models presented in Equations 3.2 and 3.3, respectively. For all analysis presented in this chapter, the material

deformation is assumed to be within the elastic portion of the stress-strain curve.

As with the uniaxial compression test, there is little to no justification in the selection of the sizing of specimens nor is there any formal guidance on selecting a three- or four-point bending test. For the case of three-point bending, ASTM E290 gives a recommendation of the support spacing, referred to in this work as L. However, no reasoning is given for this recommendation. Furthermore, as with the uniaxial compression test, only applied strains are discussed in ASTM E290, implying that a displacement-controlled test is preferred. As a direct comparison of three- and four-point bending, there is informal guidance to suggest three-point bending is more suited for ductile materials and four point for more brittle materials, due to the concentration of stresses under the applied load in three point and a more distributed stress profile in four point.

3.2.1 Three- and four-point bending: parameter sensitivities

Similarly to uniaxial compression, the normalized parameter sensitivities for both three- and four-point bending are summed to use in the assessment of the optimal testing configuration. The parameters assessed include the sample geometry (L, b, d and a) and the force-to-displacement relationship (F and δ). The parameter bounds outlined in Table 3.1 are used for three- and four-point bending, with the addition of a, bounded by zero and one in four-point bending. Equation 3.4 is used to calculate the normalized parameter sensitivities. For the case of a displacement-controlled test $\alpha = F$ and $\beta = [E, \delta, b, d, L]$ in three-point bending and $\beta = [E, \delta, b, d, L, a]$ in four-point bending. For a force-controlled test $\alpha = \delta$ and $\beta = [E, F, b, d, L]$ for three-point bending and $\beta = [E, F, b, d, L, a]$ for four-point bending. The normalized parameter sensitivities for all parameters are presented in Figure 3.4 for three-point bending and Figure 3.5 for four-point bending. As with uniaxial compression, the normalized parameter sensitivities are identical across force and displacement control, as they are independent of the configuration of the test. Finally, the normalized sensitivity of the b parameter falls exactly behind the normalized sensitivity of δ and as with uniaxial compression some plots stop abruptly due to the in-feasibility of configurations beyond that point.

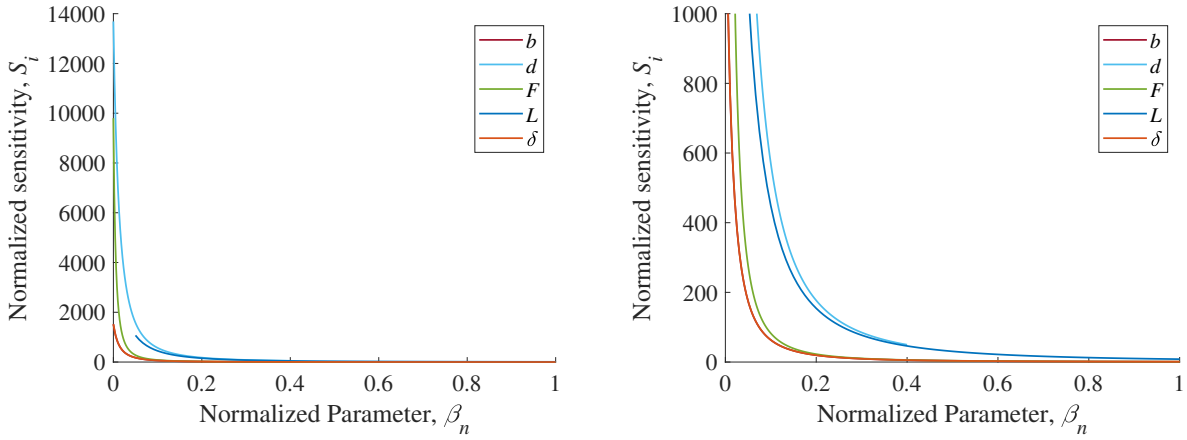

(a) (b)

Figure 3.4: Three-point bending parameter sensitivities: (a) full range of S_i; (b) highlighted range of S_i.

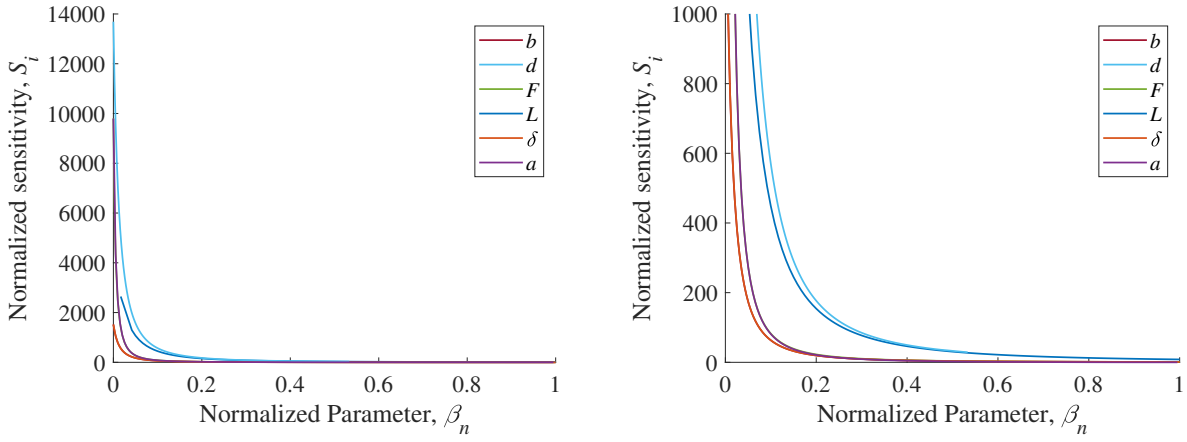

(a) (b)

Figure 3.5: Four-point bending parameter sensitivities: (a) full range of S_i; (b) highlighted range of S_i.

As with uniaxial compression the normalized parameter sensitivity trends show that for the objective of minimizing the sensitivity of all parameters except for E, maximizing all parameters except for E will give the ideal configuration. However, this is not possible due to the requirement to be compliant with the forward model.

3.2.2 Three- and four-point bending: implementation of Q

The combination of the parameter sensitivities for three-point bending, into Q (Equation 2.1), for a displacement-controlled test is

$$Q_{3,DC} = \frac{1}{5}\left[-\left(\frac{\partial F}{\partial E}\frac{E_{avg}}{F}\right)^2 + \left(\frac{\partial F}{\partial \delta}\frac{\delta_{avg}}{F}\right)^2 + \left(\frac{\partial F}{\partial b}\frac{b_{avg}}{F}\right)^2 + \left(\frac{\partial F}{\partial d}\frac{d_{avg}}{F}\right)^2 + \left(\frac{\partial F}{\partial L}\frac{L_{avg}}{F}\right)^2\right] \tag{3.15}$$

As with all previous examples all weights are set at one, intending that sensitivities be to be minimized except negative one for the sensitivity of the material parameter, E, so it is maximized. By substituting Equation 3.2 into Equation 3.15, this becomes

$$Q_{3,DC} = \frac{1}{5}\left[-\left(\frac{4\delta b d^3}{L^3}\frac{E_{avg}}{F}\right)^2 + \left(\frac{4Ebd^3}{L^3}\frac{\delta_{avg}}{F}\right)^2 + \left(\frac{4E\delta d^3}{L^3}\frac{b_{avg}}{F}\right)^2 + \left(\frac{12E\delta bd^2}{L^3}\frac{d_{avg}}{F}\right)^2 + \left(\frac{-12E\delta bd^3}{L^4}\frac{L_{avg}}{F}\right)^2\right]$$

which can be further simplified by making a substitution in each term for the forward model, resulting in

$$Q_{3,DC} = \frac{1}{5}\left[-\left(\frac{E_{avg}}{E}\right)^2 + \left(\frac{\delta_{avg}}{\delta}\right)^2 + \left(\frac{b_{avg}}{b}\right)^2 + \left(\frac{3d_{avg}}{d}\right)^2 + \left(\frac{3L_{avg}}{L}\right)^2\right] \tag{3.16}$$

The final form, as presented in Equation 3.16, further removes the negative from the derivative in the final term, as this is squared and the negative is irrelevant.

For the case of force control the implementation of the quantitative metric, Q, is

$$Q_{3,FC} = \frac{1}{5}\left[-\left(\frac{\partial\delta}{\partial E}\frac{E_{avg}}{\delta}\right)^2+\left(\frac{\partial\delta}{\partial F}\frac{F_{avg}}{\delta}\right)^2+\left(\frac{\partial\delta}{\partial b}\frac{b_{avg}}{\delta}\right)^2+\left(\frac{\partial\delta}{\partial d}\frac{d_{avg}}{\delta}\right)^2+\left(\frac{\partial\delta}{\partial L}\frac{L_{avg}}{\delta}\right)^2\right] \tag{3.17}$$

The substitution of Equation 3.2, rearranged for δ as the subject, modifies this to

$$\begin{aligned} Q_{3,FC} = \frac{1}{5}\Bigg[&-\left(-\frac{FL^3}{4E^2bd^3}\frac{E_{avg}}{\delta}\right)^2+\left(\frac{L^3}{Ebd^3}\frac{F_{avg}}{\delta}\right)^2+\left(-\frac{FL^3}{4Eb^2d^3}\frac{b_{avg}}{\delta}\right)^2 \\ &+\left(-\frac{3FL^3}{4Ebd^4}\frac{d_{avg}}{\delta}\right)^2+\left(\frac{3FL^2}{4Ebd^3}\frac{L_{avg}}{\delta}\right)^2\Bigg] \end{aligned} \tag{3.18}$$

Finally, an additional substitution of the forward model (Equation 3.2) is made to each term, resulting in

$$Q_{3,FC} = \frac{1}{5}\left[-\left(\frac{E_{avg}}{E}\right)^2+\left(\frac{F_{avg}}{F}\right)^2+\left(\frac{b_{avg}}{b}\right)^2+\left(\frac{3d_{avg}}{d}\right)^2+\left(\frac{3L_{avg}}{L}\right)^2\right] \tag{3.19}$$

The final form of Q for force control can be compared to that of displacement control, to see that the only difference is the F and δ terms. The displacement-controlled test is preferred when $Q_{3,DC} < Q_{3,FC}$, or

$$\begin{aligned} &\frac{1}{5}\left[-\left(\frac{E_{avg}}{E}\right)^2+\left(\frac{\delta_{avg}}{\delta}\right)^2+\left(\frac{b_{avg}}{b}\right)^2+\left(\frac{3d_{avg}}{d}\right)^2+\left(\frac{3L_{avg}}{L}\right)^2\right] \\ &\qquad < \frac{1}{5}\left[-\left(\frac{E_{avg}}{E}\right)^2+\left(\frac{F_{avg}}{F}\right)^2+\left(\frac{b_{avg}}{b}\right)^2+\left(\frac{3d_{avg}}{d}\right)^2+\left(\frac{3L_{avg}}{L}\right)^2\right] \end{aligned} \tag{3.20}$$

This inequality simplifies to Equation 3.13, the same as in found in uniaxial compression.

Consider two samples of the same material, presented in Table 3.5. Both are tested under displacement control conditions, and F_{avg}/δ_{avg} = 49.3 N/mm. In comparing the inequality in Equation 3.13 to the final column in Table 3.5, for Test 1 a displacement-controlled test is preferred

Table 3.5: Force- vs displacement-controlled test variable sample size.

Test #	E (MPa)	F (N)	δ (mm)	b (mm)	d (mm)	L (mm)	Q_{FC}	Q_{DC}	F/δ (N/mm)
1	500	100	40	10	10	200	1272.0	763.2	2.5
2	200	10000	6.4	50	50	200	-44.9	6.4	1562.5

and for Test 2 force control is preferred. This is in agreement with the Q values for both tests and force- and displacement-controlled tests. Practically speaking, if one was to imagine running the tests presented, Test 1 has a relatively high displacement and low force, therefore a small fluctuation of δ will have less impact on an experimental output than if F was an input variable subjected to a small fluctuation. Alternatively, in Test 2, the F is relatively high and δ is low, meaning a small fluctuation in F will have less impact on an output.

The same process can be followed to implement the quantitative metric for the four-point bending displacement-controlled test, where Q is

$$Q_{4,DC} = \frac{1}{6}\Bigg[-\left(\frac{\partial F}{\partial E}\frac{E_{avg}}{F}\right)^2 + \left(\frac{\partial F}{\partial \delta}\frac{\delta_{avg}}{F}\right)^2 + \left(\frac{\partial F}{\partial b}\frac{b_{avg}}{F}\right)^2 + \left(\frac{\partial F}{\partial d}\frac{d_{avg}}{F}\right)^2 + \left(\frac{\partial F}{\partial L}\frac{L_{avg}}{F}\right)^2 + \left(\frac{\partial F}{\partial a}\frac{a_{avg}}{F}\right)^2\Bigg] \tag{3.21}$$

The substitution of the forward model, Equation 3.3, results in

$$Q_{4,DC} = \frac{1}{6}\Bigg[-\left(\frac{4\delta b d^3}{L^3 a(3-a^2)}\frac{E_{avg}}{F}\right)^2 + \left(\frac{4Ebd^3}{L^3 a(3-a^2)}\frac{\delta_{avg}}{F}\right)^2 + \left(\frac{4E\delta d^3}{L^3 a(3-a^2)}\frac{b_{avg}}{F}\right)^2 + \left(\frac{12E\delta b d^2}{L^3 a(3-a^2)}\frac{d_{avg}}{F}\right)^2 + \left(\frac{-12E\delta b d^3}{L^4 a(3-a^2)}\frac{L_{avg}}{F}\right)^2 + \left(\left(\frac{8E\delta b d^3}{L^3(3-a^2)^2} - \frac{4E\delta b d^3}{L^3 a^2(3-a^2)}\right)\frac{a_{avg}}{F}\right)^2\Bigg] \tag{3.22}$$

The final substitution made in both the uniaxial compression and three-point bending tests does not apply to the four-point bending. Due to the added complexity of the final term, a, the substitution of the forward model to provide further simplification is not possible.

Finally, the same process is again followed for the four-point bending force-controlled test, where Q is

$$Q_{4,FC} = \frac{1}{6}\Bigg[-\left(\frac{\partial\delta}{\partial E}\frac{E_{avg}}{\delta}\right)^2 + \left(\frac{\partial\delta}{\partial F}\frac{F_{avg}}{\delta}\right)^2 + \left(\frac{\partial\delta}{\partial b}\frac{b_{avg}}{\delta}\right)^2 + \left(\frac{\partial\delta}{\partial d}\frac{d_{avg}}{\delta}\right)^2 + \left(\frac{\partial\delta}{\partial L}\frac{L_{avg}}{\delta}\right)^2 + \left(\frac{\partial\delta}{\partial a}\frac{a_{avg}}{\delta}\right)^2\Bigg] \tag{3.23}$$

The substitution of the forward model, Equation 3.3, rearranged for δ as the subject, results in

$$Q_{4,FC} = \frac{1}{6}\Bigg[-\left(\frac{-FL^3a(3-a^2)}{4E^2bd^3}\frac{E_{avg}}{\delta}\right)^2 + \left(\frac{L^3a(3-a^2)}{4Ebd^3}\frac{F_{avg}}{\delta}\right)^2 + \left(\frac{FL^3a(3-a^2)}{4Eb^2d^3}\frac{b_{avg}}{\delta}\right)^2 + \left(\frac{3FL^3a(3-a^2)}{4Ebd^4}\frac{d_{avg}}{\delta}\right)^2 + \left(\frac{3FL^2a(3-a^2)}{4Ebd^3}\frac{L_{avg}}{\delta}\right)^2 + \left(\left(\frac{FL^3a^2}{2Ebd^3} + \frac{FL^3(3-a^2)}{4Ebd^3}\right)\frac{a_{avg}}{\delta}\right)^2\Bigg] \tag{3.24}$$

3.2.3 Three- and four-point bending: optimization through minimizing Q

The methodology for optimizing the parameter sensitivities by minimizing Q is the same as with uniaxial compression. The optimization problem for three-point bending displacement-controlled test is

$$\begin{aligned}
\min_{F,\delta,b,d,L} Q_{3,DC} =& \frac{1}{5}\left[-\left(\frac{E_{avg}}{E}\right)^2 + \left(\frac{\delta_{avg}}{\delta}\right)^2 + \left(\frac{b_{avg}}{b}\right)^2 + \left(\frac{3d_{avg}}{d}\right)^2 + \left(\frac{3L_{avg}}{L}\right)^2\right] \\
& s.t.\ 100 \leq F \leq 10,000\ \text{N} \\
& s.t.\ 5 \leq \delta \leq 200\ \text{mm} \\
& s.t.\ 10 \leq b \leq 400\ \text{mm} \\
& s.t.\ 10 \leq d \leq 400\ \text{mm} \\
& s.t.\ 20 \leq L \leq 500\ \text{mm} \\
& s.t.\ E = \frac{FL^3}{4\delta bd^3}
\end{aligned} \tag{3.25}$$

The optimization problem presented in Equation 3.25 is a minimization of the Q presented in Equation 3.16. The optimization problem for a force-controlled test is similar to that presented in Equation 3.25, with the substitution for Equation 3.19 in place of Equation 3.16.

The optimization for a four-point bending displacement-controlled test is

$$\begin{aligned}\min_{F,\delta,b,d,L,a} Q_{4,DC} = \frac{1}{6}\Bigg[& -\left(\frac{4\delta bd^3}{L^3a(3-a^2)}\frac{E_{avg}}{F}\right)^2 + \left(\frac{4Ebd^3}{L^3a(3-a^2)}\frac{\delta_{avg}}{F}\right)^2 \\ & + \left(\frac{4E\delta d^3}{L^3a(3-a^2)}\frac{b_{avg}}{F}\right)^2 + \left(\frac{12E\delta bd^2}{L^3a(3-a^2)}\frac{d_{avg}}{F}\right)^2 + \left(\frac{-12E\delta bd^3}{L^4a(3-a^2)}\frac{L_{avg}}{F}\right)^2 + \\ & \left(\left(\frac{8E\delta bd^3}{L^3(3-a^2)^2} - \frac{4E\delta bd^3}{L^3a^2(3-a^2)}\right)\frac{a_{avg}}{F}\right)^2\Bigg] \\ & s.t.\ 100 \leq F \leq 10,000 \text{ N} \\ & s.t.\ 5 \leq \delta \leq 200 \text{ mm} \\ & s.t.\ 10 \leq b \leq 400 \text{ mm} \\ & s.t.\ 10 \leq d \leq 400 \text{ mm} \\ & s.t.\ 20 \leq L \leq 500 \text{ mm} \\ & s.t.\ 0 \leq a \leq 1 \\ & s.t.\ E = \frac{FL^3a(3-a^2)}{4\delta bd^3}\end{aligned} \tag{3.26}$$

where the constraint is added for the bounds of the parameter a. The same process can be used to present the optimization for a force-controlled test.

3.2.4 Three- and four-point bending: analysis for optimal configuration

Optimal configurations for varying E values are presented in Table 3.6 for three-point bending and Table 3.7 for four-point bending. As was the case for uniaxial compression in Section 3.1.4, there are many complexities contained in Tables 3.6 and 3.7 which result from the multi-dimensional optimization. Most of the conclusions drawn through these tables are the same that were found in uniaxial compression, with the addition of the finding that in all cases the four-point bending test

Table 3.6: Three-point bending optimal configurations for force- and displacement-controlled tests. Bold text indicates values kept constant in the optimization.

	Displacement control			Force control		
	1	2	3	1	2	3
E (MPa)	**200**	**1,000**	**5,000**	**200**	**1,000**	**5,000**
F (N)	10,000	10,000	10,000	10,000	10,000	10,000
δ (mm)	28.5	20.7	15	5	5	5
b (mm)	57	41.3	29.9	88.1	58.9	39.4
d (mm)	98.7	71.5	51.9	152.5	102	68.2
L (mm)	500	500	500	500	500	500
Q	-496.6	4.7	46.6	-505.2	-10.2	21.4

optimizes to a three-point bending test. Both F and L are maximized in all cases, meaning their normalized sensitivities are minimized. The sensitivity of δ is not included in the optimization of a force-controlled test, and this results in it minimizing in both three- and four-point bending. Across the various E values included in the table, the b:d ratios are constant within each of the tests and δ:b ratios are constant for displacement-controlled tests. All the trends presented are similar to that with uniaxial compression. In displacement-controlled tests, the larger sample sizes are competing with the increasing δ, whereas in force-controlled tests, increasing F and sample size can be facilitated with a decrease in δ. For the four-point bending test the value of a optimizes to one in all cases. Variable a is a ratio of how far the applied forces are from the support with zero indicating at the support and one at the center. Therefore, the results presented in Table 3.7 show that the four-point bending tests always optimize to three-point bending tests. The values of Q in Tables 3.6 and 3.7 are not the same due to the four-point bending test having two applied forces and including the normalized sensitivity of a in the calculation of Q.

The sample slenderness relationship is further investigated through Figure 3.6, for the case of three-point bending, where the quantitative metric for various F/δ relationships are plotted for varying L/b ratios. Except for the case of high F/δ ratios in the displacement-controlled test, all cases show more slender sample is more desirable. For a given slenderness ratio, a higher F/δ ratio is more desirable. The shape of each of the lines results from the influence of the shape of the

Table 3.7: Four-point bending optimal configurations for force- and displacement-controlled tests. Bold text indicates values kept constant in the optimization.

	Displacement control			Force control		
	1	2	3	1	2	3
E (MPa)	**200**	**1,000**	**5,000**	**200**	**1,000**	**5,000**
F (N)	10,000	10,000	10,000	10,000	10,000	10,000
δ (mm)	32.7	23.7	17.2	5	5	5
b (mm)	65.5	47.5	34.4	104.7	70	46.8
d (mm)	113.4	82.2	59.6	181.4	121.3	81.1
L (mm)	500	500	500	500	500	500
a	1	1	1	1	1	1
Q	-416.5	-1	29.3	-422	-10.8	12.5

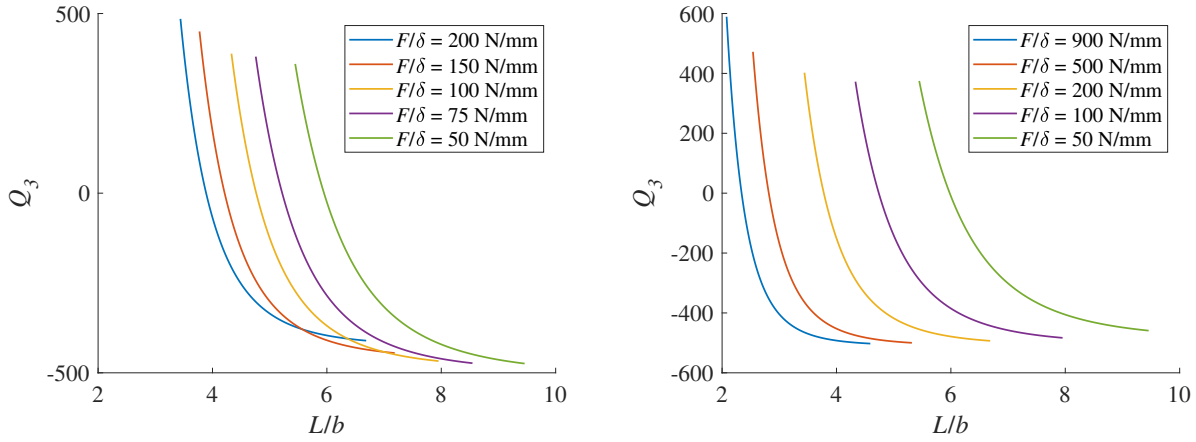

(a) (b)

Figure 3.6: Three-point bending slenderness ratios: (a) displacement control; (b) force control.

normalized sensitivity plots. As the feasible L/b values decrease, b approaches the lower bound and its normalized sensitivity rapidly increases. As with uniaxial compression the F/δ ratios are chosen by holding one parameter fixed and selecting representative values of the other over its respective range. For displacement control δ is fixed and F varied.

3.3 Detailed analysis of cantilever beam

In order to add a level of complexity to the analysis the model for the tip displacement of a rectangular cantilever beam is implemented. As can be seen in Equation 3.27 this model has the same

geometric qualities (b, d, L) and force/displacements (F and δ) of the previously investigated tests. The significant differences are an additional material property (ν) and a slightly more complex model. When assigning weights in the implementation of the quantitative metric all non-material parameters (b, d, L, F and δ) are assigned a value of one, and the material parameters (E and ν) are assigned negative one so their sensitivity is maximized.

$$F = \left(\frac{\delta E b d^3}{4L^3}\right)\left(\frac{1}{1+\left(2+\frac{5\nu}{2}\right)\left(\frac{d}{4L^2}\right)}\right) \tag{3.27}$$

This exact analytical model was first proposed by Livesley [119] and is studied in detail by Muir Wood [120]. This section follows the same structure of previous sections, the parameter sensitives are assessed before the implementation of Q and application to optimization.

3.3.1 Cantilever beam: parameter sensitivities

As with previous implementations, Equation 3.4 is used to determine the individual normalized parameter sensitivities. For the cantilever beam, the parameters which are analyzed include F, δ, b, d, L, E, ν, and in a displacement-controlled test $\alpha = F$ and $\beta = [\delta, b, d, L, E, \nu]$. The bounds used for the cantilever beam test have been changed slightly from the previous tests and are presented in Table 3.8. This change is to facilitate the comparison of a test (in Section 3.4) which is somewhat different to the uniaxial, three- and four-point bending tests. Figure 3.7 presents the normalized parameter sensitivities for all the parameters in this test, these normalized parameter sensitivities are independent of the type of test, force or displacement control.

As with all previous models, all the parameters of the cantilever beam model have maximum sensitivities at their minimum values and minimum sensitivity values at their maximum values. The complexity of the forward model means that the derivatives are now multiple terms and can no longer be reduced with substitution. This is not an issue as no analytical analysis of the optimization is possible due to the complexity of the forward model. The multi-dimensional normalized parameter sensitivities will only impact the optimization complexity, which can be handled by

Table 3.8: Cantilever beam parameter bounds.

Parameter	Lower bound	Upper bound	Average $(\beta_{i,avg})$
E (MPa)	200	20,000	10,100
ν	0.0001	0.5	0.25005
F (N)	100	10,000	5,050
δ (mm)	5	500	252.5
b (mm)	10	1000	505
d (mm)	10	1000	505
L (mm)	20	1000	510

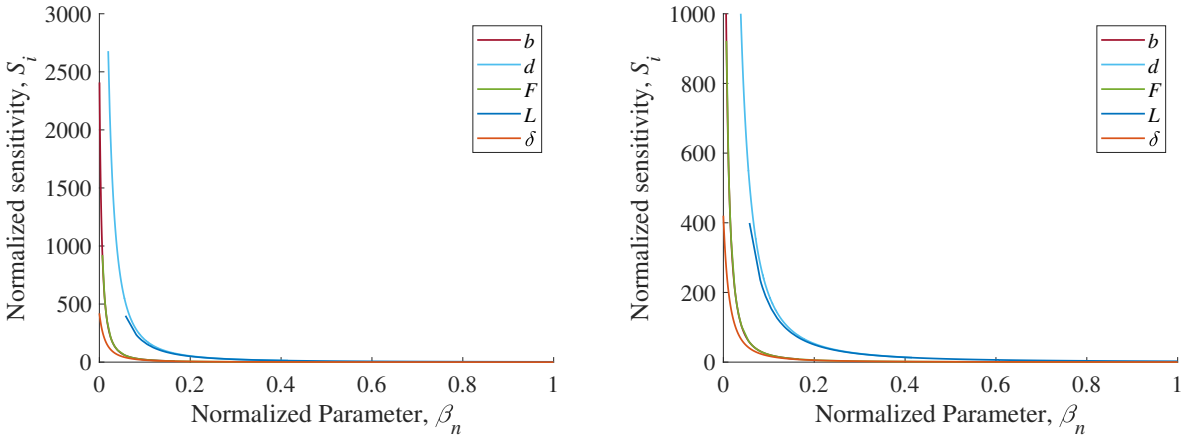

Figure 3.7: Cantilever beam parameter sensitivities: (a) full range of S_i; (b) highlighted range of S_i.

the robust solver selected. All the derivations are completed in MATHEMATICA [121] prior to implementing into the solver.

At this stage it is identified that the sensitivity of the material parameters (E and ν) are independent of the configuration (b, d, L, F and δ). Meaning that the sensitivity of the material parameter to the output is a function of only the material parameter and no other parameters. This can be shown by taking the normalized sensitivity of E,

$$S_E = \left[\left(\frac{\partial E}{\partial F}\right)\left(\frac{E_{avg}}{F}\right)\right]^2$$

and inserting the partial derivative of Equation 3.27 with respect to E and the value of F as Equation 3.27. This results in

$$S_E = \left[\left[\frac{bd^3\delta}{4L^3\left(1+\frac{d(2+5\nu/2)}{4L^2}\right)}\right]\left[\frac{E_{avg}}{\left(\frac{\delta E b d^3}{4L^3}\right)\left(\frac{1}{1+\left(2+\frac{5\nu}{2}\right)\left(\frac{d}{4L^2}\right)}\right)}\right]\right]^2$$

which finally simplifies to $(E_{avg}/E)^2$. As this result is only dependent on the value of E the sensitivity of E can be deemed independent of the configuration of the test. Furthermore, the normalized sensitivity of ν is insignificant in comparison to other normalized sensitivities.

3.3.2 Cantilever beam: implementation of quantitative metric and optimization

The combination of the parameter sensitivities for the cantilever beam model, into Q (Equation 2.1), for a displacement-controlled test is

$$\begin{aligned} Q_{C,DC} = \frac{1}{6}\Bigg[&- \left(\frac{\partial F}{\partial E}\frac{E_{avg}}{F}\right)^2 - \left(\frac{\partial F}{\partial \nu}\frac{\nu_{avg}}{F}\right)^2 + \left(\frac{\partial F}{\partial \delta}\frac{\delta_{avg}}{F}\right)^2 \\ &+ \left(\frac{\partial F}{\partial b}\frac{b_{avg}}{F}\right)^2 + \left(\frac{\partial F}{\partial d}\frac{d_{avg}}{F}\right)^2 + \left(\frac{\partial F}{\partial L}\frac{L_{avg}}{F}\right)^2\Bigg] \end{aligned} \tag{3.28}$$

The derivative implementation of Equation 3.27 is significantly long and is therefore omitted here. The optimization of Q is a minimization, represented as

$$\begin{aligned}
\min_{F,\delta,b,d,L} Q_{C,DC} = \frac{1}{6}\Bigg[& -\left(\frac{\partial F}{\partial E}\frac{E_{avg}}{F}\right)^2 - \left(\frac{\partial F}{\partial \nu}\frac{\nu_{avg}}{F}\right)^2 + \left(\frac{\partial F}{\partial \delta}\frac{\delta_{avg}}{F}\right)^2 \\
& + \left(\frac{\partial F}{\partial b}\frac{b_{avg}}{F}\right)^2 + \left(\frac{\partial F}{\partial d}\frac{d_{avg}}{F}\right)^2 + \left(\frac{\partial F}{\partial L}\frac{L_{avg}}{F}\right)^2 \Bigg] \\
& s.t.\ 100 \leq F \leq 10,000 \text{ N} \\
& s.t.\ 5 \leq \delta \leq 500 \text{ mm} \\
& s.t.\ 10 \leq b \leq 1,000 \text{ mm} \\
& s.t.\ 10 \leq d \leq 1,000 \text{ mm} \\
& s.t.\ 20 \leq L \leq 1,000 \text{ mm} \\
& s.t.\ 0.0001 \leq \nu \leq 0.5 \\
& s.t.\ E = \frac{4FL^3}{\delta b d^3}\left[1 + \left(2 + \frac{5\nu}{2}\right)\left(\frac{d}{4L^2}\right)\right]
\end{aligned} \tag{3.29}$$

Equation 3.29 is similar to previously presented optimization problems with the exception of the new bounds and the requirement to comply with the cantilever beam forward model (the final constraint).

Select optimizations for various (constant) material parameters are presented in Table 3.9 for displacement-controlled tests and Table 3.10 for force-controlled tests. Three different values of E are considered and two values of ν. The values are selected such that they present a representative range of the parameter bounds.

The comparison of the force- and displacement-controlled tests across various material parameters reveals many complexities, with most very similar to the previously presented optimizations. The variation of ν has little to no impact on the optimized configuration and value of Q. This is due to the low sensitivity of ν in all cases. There is a decrease of the sample cross-sectional area and δ for an increasing material stiffness for both force- and displacement-controlled tests,

Table 3.9: Cantilever beam optimal configurations for displacement-controlled tests for varying material parameters. Bold text indicates values kept constant in the optimization.

	1	2	3	4	5	6
E (MPa)	**200**	**2000**	**20,000**	**200**	**2000**	**20,000**
ν	**0.25**	**0.25**	**0.25**	**0.5**	**0.5**	**0.5**
F (N)	10,000	10,000	10,000	10,000	10,000	10,000
δ (mm)	75.2	47.5	29.9	75.2	47.5	29.9
b (mm)	150.4	94.9	59.9	150.4	94.9	59.9
d (mm)	260.5	164.4	103.7	260.5	164.4	103.7
L (mm)	1,000	1,000	1,000	1,000	1,000	1,000
Q	-415.3	19.7	59.6	-415.3	19.7	59.6

Table 3.10: Cantilever beam optimal configurations for force-controlled tests for varying material parameters. Bold text indicates values kept constant in the optimization.

	1	2	3	4	5	6
E (MPa)	**200**	**2000**	**20,000**	**200**	**2000**	**20,000**
ν	**0.25**	**0.25**	**0.25**	**0.5**	**0.5**	**0.5**
F (N)	10,000	10,000	10,000	10,000	10,000	10,000
δ (mm)	5	5	5	5	5	5
b (mm)	296	166.6	93.7	295.8	166.6	93.7
d (mm)	513.2	288.5	162.2	513.2	288.5	162.2
L (mm)	1,000	1,000	1,000	1,000	1,000	1,000
Q	-422.7	2.3	19.8	-422.7	2.3	19.8

as was the case with previous optimizations. Furthermore, in both the force- and displacement-controlled tests, F and L optimize to their upper bounds in all cases presented. This is the same result that was presented for all previously assessed optimizations. As was explained previously, a more desirable Q is achieved with smaller parameter sensitivities—larger parameter values. In a displacement-controlled test for a constant material (E and ν), a larger sample (b, d and L) and larger displacement (δ) both require the force (F) to increase. Once F is maximized the optimization finds a compromise for the sample size and displacement, presented here as the optimized δ, b and d values. Alternatively, for the force-controlled tests, a larger sample and larger force are more desirable and these can be accommodated for with a constant material by decreasing the displacement. Once the displacement is optimized to its minimum then a compromise is found for b and d.

Similar to previous tests investigated, the relationship between sample slenderness and the force-displacement ratio is assessed visually. Figure 3.8 is presented for force- and displacement-controlled tests and shows for a given stiffness (F/δ), a more slender sample is more desirable. Additionally for a given slenderness ratio, a smaller stiffness is more desirable. In contrast to previous slenderness plots, there is a significant plateau showing that for each of the F/δ values, once a sufficient L/b is reached no further improvement in Q will be seen. For each F/δ a decrease in L/b leads to a rapid increase of Q, beyond the critical L/b, and caused by the normalized parameter sensitivities increasing as the parameter approaches its minimum.

3.4 Comparison of tests

The major development that the quantitative metric brings is the ability to compare different tests through an unbiased singular metric. In this section, further comparisons will be made between (1) different configurations of the same test, (2) different testing methods of the same test (force and displacement control) and (3) different tests (uniaxial, three-point and four-point bending and cantilever beam). Section 3.5 provides empirical proof of concept for the ability to compare different tests with the quantitative metric by implementing random error and comparing the error on

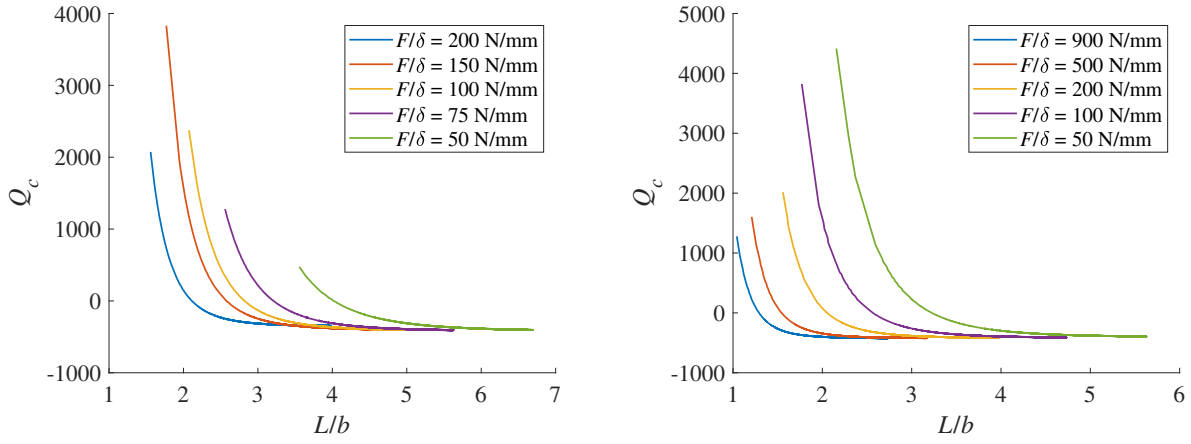

Figure 3.8: Cantilever beam slenderness ratios: (a) displacement control; (b) force control.

the computed material parameter to the quantitative metric across various test configurations and test types.

3.4.1 Comparisons of different configurations of the same test

The optimizations previously presented for uniaxial compression, three-point bending and four-point bending are functions of six (uniaxial compression and three-point bending) and seven (four-point bending) variables. This can be observed by assessing the number of variables in each of the respective Q functions. Therefore, the parameter space of the optimization cannot be easily visualized with basic plotting tactics. The entire six/seven-dimensional parameter space for each test is presented in this section (Figures 3.9 and 3.10) by compressing a cloud of feasible configurations and overlaying it with slices of the multi-dimensional space. This visualization is created by generating random test configurations compliant with the respective forward models and computing a normalized Euclidean distance from the optimal configuration using

$$x = \sqrt{\left(\frac{F_{opt} - F_i}{F_{avg}}\right)^2 + \left(\frac{L_{opt} - L_i}{L_{avg}}\right)^2 + \left(\frac{\delta_{opt} - \delta_i}{\delta_{avg}}\right)^2 + \left(\frac{b_{opt} - b_i}{b_{avg}}\right)^2 + \left(\frac{d_{opt} - d_i}{d_{avg}}\right)^2} \tag{3.30}$$

where the opt subscript defines the optimized parameters, i subscripts defines the terms for the current calculation and the avg subscript is the average value of the parameter bounds outlined in Table 3.1. Here the Euclidean distance is a measure of the distance between the generated testing configuration and the optimal configuration, and it is scaled by the average parameter across the previously presented parameter range. Compliant testing configurations are generated by randomly generating all but one of the parameters within their specified bounds then computing the final parameter using the forward model. A final check is made to ensure the computed value is within the bounds of this parameter (Table 3.1). For example, for uniaxial compression test and a given E, the parameters F, L, b and d can be randomly generated to be within the bounds of the constraints of the optimization (Table 3.1), then δ is computed using the forward model (Equation 3.1), and finally checked to be within its specified bounds. If any of the parameters, randomly generated or computed, are outside of the specific parameter bounds, the testing configuration is not considered. For each compliant test configuration, the quantitative metric is computed. All configurations presented in Figures 3.9 and 3.10 have an E = 1000 MPa.

Overlaid on the randomly generated configurations in Figures 3.9 and 3.10 are a select few slices of this multi-dimensional space, where all parameters except two are kept constant at the optimal and the two non-constant parameters are varied. These select conditions are generated by varying one parameter across its parameter space and re-computing the other parameter with the respective forward model. All other parameters are kept constant as their optimal values, hence all the overlaid functions pass through the zero location for distance and the optimal configuration.

As can be seen in Figures 3.9 and 3.10, all three tests create clouds of varying geometry, with increasing Q as distance from the optimal increases. The clouds presented are for the elastic modulus of E = 200 MPa. In all situations, it is found that there are no local minimums, and the seemingly odd shape of the cloud with almost a plateau in three and four-point bending displacement control is simply created by condensing the six, and seven dimensional plots into a two-dimensional plot. Both lack of local minimums and the multi dimensionality of the plots are highlighted by the convex overlaid functions. Particular similarities can be seen in the three and four-point bending

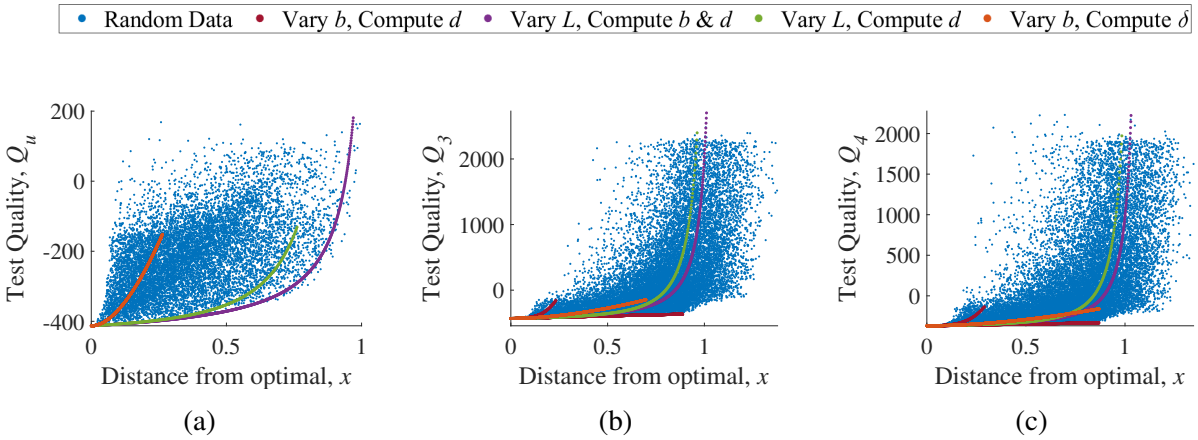

Figure 3.9: Grid search for displacement control and E = 200 MPa: (a) uniaxial compression; (b) three-point bending; (c) four-point bending.

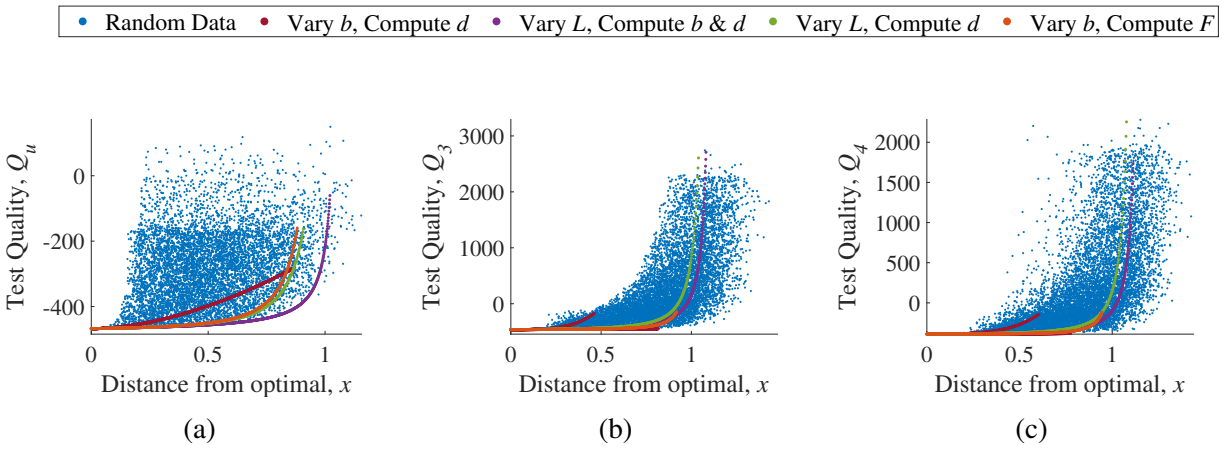

Figure 3.10: Grid search for force control and E = 200 MPa: (a) uniaxial compression; (b) three-point bending; (c) four-point bending.

tests and this is due to the only physical difference between the tests being the positioning of the load, when the load in four-point bending is halved and placed at the mid-span the test becomes the three-point bending test. To highlight the multi-dimensionality of the clouds, consider the overlaid functions. Firstly, the red curve follows a single path in both Figures 3.9a and 3.10a. This is due to the influence of b and d being the same on both axis of the plot and the red curve slits into two paths in Figures 3.9b, 3.9c, 3.10b and 3.10c due to d having a cubic power in the forward model and hence influencing the calculation of Q. All other curves have one of the optimal parameters of interest (in these cases either F or L) on the upper or lower bound, meaning that only one line is produced moving away from the optimal.

3.4.2 Comparison of uniaxial compression and three-point bending

In an effort to compare different tests the direct analytical comparison of Q for uniaxial compression and three-point bending is made. Due to the uniaxial and three-point bending tests having different forward models, testing configurations that are the exactly the same and comply perfectly with both forward models do not exist. This is because F and δ are physically different quantities in the two tests. For this reason, the tests compared here have different displacements in displacement control and different forces in force control. All other parameters are equal. The inequality that must be satisfied for uniaxial compression to be preferred in displacement control is

$$\delta_u^2 \left[0.310836 d^8 L^4 + 0.621672 \delta_u^2 d^2 L^8 + d^4 \left(\delta_u^2 L^6 - 0.0194272 L^8\right)\right] > 0 \tag{3.31}$$

where δ_u is the displacement in the a uniaxial compression test. The inequality for uniaxial to be preferred in force control is

$$F_u^2 d^2 L^2 \left[32 F_u^2 \left(2704 d^4 + 1681 d^2 L^2\right) - 255025 \left(16 d^4 L^2 - L^6\right)\right] > 0 \tag{3.32}$$

where F_u is the displacement in the a uniaxial compression test. These inequalities have been developed by equating Equations 3.9 and 3.16 for displacement control and Equations 3.11 and

3.19 for force control. As can be seen through both Equations 3.31 and 3.32, the equalities are a function of L, d and either δ_u (displacement control) or F_u (force control). This dependence is due to the difference in the two forward models being a function of L and d, therefore influencing the L and d sensitivity terms differently in the two tests. Furthermore, the different δ_u or F_u influence the δ or F sensitivity terms for force and displacement control respectively. In this case, analytical expressions giving the preferred test are available.

3.4.3 Comparison of three- and four-point bending

Furthermore, comparisons are made between three- and four-point bending tests, with emphasis placed on the value of a. When the distance ratio, a, is equal to 1.0 the four-point bending test becomes a three-point bending test, although the force would be double that of an otherwise similar three-point bending test due to the presence of two forces in a four-point bending test. Figure 3.11 presents randomly generated testing configurations for the three- and four-point bending tests, for which the quantitative metric for each test is computed and compared. For a more exact comparison of the two tests, the force in four-point bending is equal to half of the force in three-point bending, and the sensitivity of a is not considered in the computation of Q for four-point bending. This implies 1:1 comparison can be made without the influence of load positioning. As with previous plots presented, the points are generated randomly, and the δ (for force control) and F (for displacement control) are computed for both tests using the forward models. Here a color scale is added to indicate the value of a. The presented figure is for an elastic modulus, E = 200 MPa, which is a material approximately equivalent to a stiff rubber.

As can be seen from Figure 3.11, a three-point bending test is always preferred in displacement control, and for the case of force control, a four-point bending test is always preferred. This is a result of the equating of the two quantitative metrics (for the same configuration aside from force or displacement) subsequently reducing to a comparison of force (for force control) or displacement (for displacement control). To determine when three-point bending is preferred for displacement

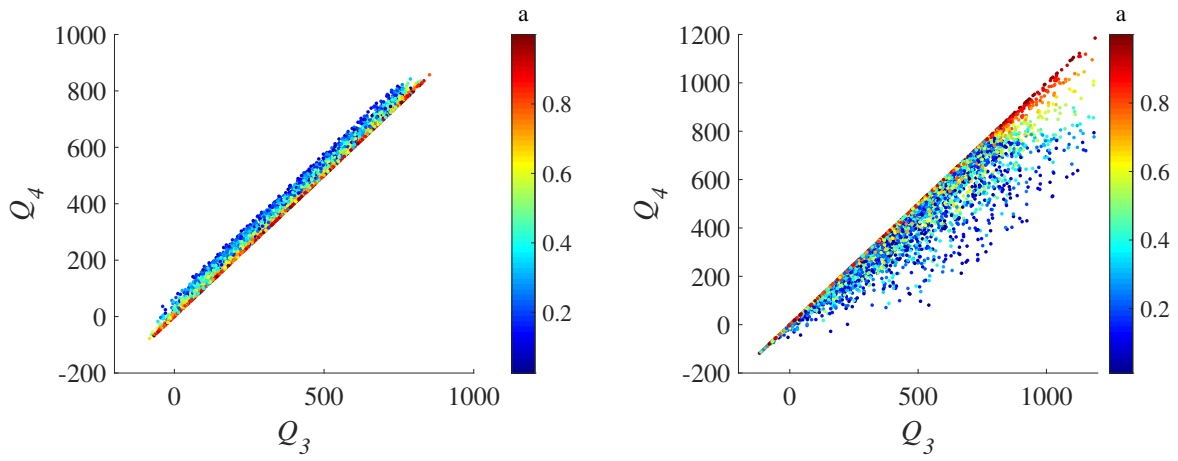

Figure 3.11: Three- and four-point bending comparison: (a) displacement control; (b) force control.

control, Equations 3.16 and 3.22 are compared, without the sensitivity of a in Equation 3.22 this is

$$\begin{aligned}
&\frac{1}{5}\left[-\left(\frac{E_{avg}}{E}\right)^2+\left(\frac{\delta_{avg}}{\delta_{3pt}}\right)^2+\left(\frac{b_{avg}}{b}\right)^2+\left(\frac{3d_{avg}}{d}\right)^2+\left(\frac{3L_{avg}}{L}\right)^2\right] \\
&\quad<\frac{1}{5}\left[-\left(\frac{4\delta_{4pt}bd^3}{L^3a(3-a^2)}\frac{E_{avg}}{F_{4pt}}\right)^2+\left(\frac{4Ebd^3}{L^3a(3-a^2)}\frac{\delta_{avg}}{F_{4pt}}\right)^2+\left(\frac{4E\delta_{4pt}d^3}{L^3a(3-a^2)}\frac{b_{avg}}{F_{4pt}}\right)^2\right. \\
&\quad\left.+\left(\frac{12E\delta_{4pt}bd^2}{L^3a(3-a^2)}\frac{d_{avg}}{F_{4pt}}\right)^2+\left(\frac{-12E\delta_{4pt}bd^3}{L^4a(3-a^2)}\frac{L_{avg}}{F_{4pt}}\right)^2\right]
\end{aligned} \tag{3.33}$$

For the same E, b, d and L, and $F_{4pt} = 0.5\ F_{3pt}$ simplifies to

$$\delta_{4pt} < \delta_{3pt} \tag{3.34}$$

In no case for the same equivalent loads is δ_{3pt} ever less than δ_{4pt}. Therefore three point is always preferred in displacement control. A similar procedure can be followed for determining when

three-point bending is preferred in force control by equating Equations 3.19 and 3.24, resulting in

$$\begin{aligned}
&\frac{1}{5}\left[-\left(\frac{E_{avg}}{E}\right)^2+\left(\frac{F_{avg}}{F_{3pt}}\right)^2+\left(\frac{b_{avg}}{b}\right)^2+\left(\frac{d_{avg}}{d}\right)^2+\left(\frac{L_{avg}}{L}\right)^2\right] \\
&<\frac{1}{5}\left[-\left(\frac{-F_{4pt}L^3a(3-a^2)}{4E^2bd^3}\frac{E_{avg}}{\delta}\right)^2+\left(\frac{L^3a(3-a^2)}{4Ebd^3}\frac{F_{avg}}{\delta}\right)^2+\left(\frac{-F_{4pt}L^3a(3-a^2)}{4Eb^2d^3}\frac{b_{avg}}{\delta}\right)^2\right. \\
&\left.+\left(\frac{-3F_{4pt}L^3a(3-a^2)}{4Ebd^4}\frac{d_{avg}}{\delta}\right)^2+\left(\frac{3F_{4pt}L^2a(3-a^2)}{4Ebd^3}\frac{L_{avg}}{\delta}\right)^2\right]
\end{aligned} \tag{3.35}$$

For the same E, b, d, L and δ, this simplifies to

$$F_{4pt} < F_{3pt} \tag{3.36}$$

Equation 3.36 indicates that four-point bending is always preferred, as the forces applied in four-point bending must always be larger than that of three-point bending in order to achieve the same displacement. Therefore, the choice of conducting a three-point bending or four-point bending test should be entirely based on the control type. If the test is to be force-controlled, a four-point bending test should be used, and if a displacement-controlled test is required, then three-point bending should be used.

To extend this idea to a practical application, consider a force-controlled test with an applied load (applying F in three-point bending or two forces at $0.5F$ in four-point bending) and the same sample. In order to minimise the error on the computed material parameters, it is most desirable to minimize the impact that fluctuations on test inputs (E, b, d, L and F) will have on the output (δ). As the same sample is considered, the same δ needs to be achieved. A larger force will be needed in four-point bending, and this will attract less error. Therefore, four-point bending would be better.

Table 3.11: Optimal test and configuration comparison.

	Uniaxial compression		Three-point bending		Four-point bending		Cantilever beam	
	DC	FC	DC	FC	DC	FC	DC	FC
E (MPa)	200	200	200	200	200	200	200	200
ν	-	-	-	-	-	-	0.25	0.25
F (N)	10,000	10,000	10,000	10,000	10,000	10,000	10,000	10,000
δ (mm)	18.4	5	28.5	5	32.7	5	75.2	5
b (mm)	36.8	70.7	57	88.1	65.5	104.7	150.4	296
d (mm)	36.8	70.7	98.7	152.5	113.4	181.4	260.5	513.2
L (mm)	500	500	500	500	500	500	1,000	1,000
a (mm)	-	-	-	-	1	1	-	-
Q	-473.2	-506.6	-496.6	-505.2	-416.5	-422	-413.3	-422.7

3.4.4 Comparison for the optimal test and configuration

Through the use of the Q presented in this work, all of the tests considered in this chapter can be directly compared. Section 3.5 provides an empirical proof of the ability to make this direct comparison. The comparison of uniaxial compression, three-point bending, four-point bending, and a cantilever beam test is subjected to many considerations, which if desired, could be addressed in optimization constraints. For an E = 200 MPa, Table 3.11 consolidates the force- (FC) and displacement-controlled (DC) test optimizations for the four tests, previously presented in this chapter.

As can be seen in Table 3.11, in all cases the force-controlled test is preferred for each of the individual tests. This is to be expected, because in the cases where it is possible to make a direct comparison between force- and displacement-controlled tests (see Equation 3.13), it is shown that a displacement controlled test is only preferred with a low F/δ ratio. In all of these cases F maximized and δ is low or minimized, presenting a high F/δ ratio. Three- and four-point bending cannot be compared here with the method presented in Section 3.4.3 due to the force in four-point bending not being halved in this section. Although, considering that Q is a function of the sensitivities of the parameters, with an equal force, displacement and length, the

larger cross-sectional area in the four-point bending test will deem it a sub-optimal test. The three remaining tests are significantly different in their setup that their Q values cannot easily be analytically compared. However, it can be seen that the cantilever beam does not have as low of a Q as the uniaxial compression and three-point bending tests. Therefore, with E = 200 MPa and the bounds specified above, the best test is a force-controlled uniaxial compression test, with a force-controlled three-point bending test a close second. Although, with such close Q values, the two tests would likely be equally sufficient.

3.5 Implementation of quantitative metric with random error generation

To assess the practical applicability of the implementation of Q, the comparison of tests is presented with realistic errors implemented in order to compute the resulting error on the material parameter. This method provides a justification of the sensitivities being used as a test comparison tool. A test found to be optimal, through a lower Q value, should also produce less error in the computation of the material parameter when random error is applied to the test inputs, when compared to a test with a higher Q value. This indicates that when a physical test is conducted, and errors are present in the measurement of test inputs, the optimal testing configuration would produce the least variation in the test output and therefore produce the most accurate measurement of the material parameter.

The error on an elastic modulus subjected to random error in a force-controlled uniaxial test is calculated here as

$$E_{error} = E - \frac{(F \pm e_F)(L \pm e_L)}{\delta (b \pm e_b)(d \pm e_d)} \tag{3.37}$$

where e_F, e_L, e_b and e_d are the applied random errors. No error is applied to the δ in this example because it is the function output in a force-controlled test. The error implemented here is designed to mimic absolute error and relative error. Absolute error is used here to refer to a measurement error bounded a predefined parameter value. This could be expected in a practical setting as the accuracy to which a measurement can be made of a dimension using a ruler, for example $\pm$0.5

Table 3.12: Parameter error bounds.

Parameter	Absolute error	Relative error
e_F (N)	$\pm$ 25	$\pm$ 99
e_δ (mm)	$\pm$ 1.25	$\pm$ 1.95
e_b (mm)	$\pm$ 2.5	$\pm$ 3.9
e_d (mm)	$\pm$ 2.5	$\pm$ 3.9
e_L (mm)	$\pm$ 5	$\pm$ 4.8

mm. Alternatively, the relative error referred to here is used to represent the use of an electronic measurement, such as a load cell or linear variable differential transformer (LVDT). In these cases, the expected error is often a percentage of the parameter range or maximum value. In this analysis, the absolute error is assumed as 25% of the lower bound of each parameter, and relative error is assumed at 1% of the parameter range, as presented in Table 3.12. The original bounds for the parameters can be found in Table 3.1

An example of the comparison of Q and the implemented error is shown in Tables 3.13 and 3.14, for two specific tests and configurations. This initial implementation of errors is intended to be simple and is the only case in this section that does not use random error. The errors used in this table are fixed at the upper bound of the error ranges detailed in Table 3.12. The configurations used are presented in Table 3.13, and the comparison in Table 3.14. For the comparison in Table 3.14, the Q's are computed using Equations 3.9, 3.11, 3.16 and 3.19, and the E_{error} is computed using Equation 3.37. Note that error is not applied to the test output for consistency with the variables assessed in Q. In Table 3.14, the three groups of rows correspond to the computed values of Q, the E_{error} computed with absolute error, and with relative error. It can be seen that when comparing the values of Q to those of E_{error}, there is a perfect comparison with the lowest Q corresponding to the lowest of both of the types of E_{error}. The highest values of E_{error} for each types error implementations also corresponds to the highest Q value.

Due to the similarity of the bounds of absolute and relative error and the same implementation method, only relative error is shown in the following analysis.

Table 3.13: Configurations for comparison example.

	Uniaxial	3-point Bending
F (N)	10,000	10,000
E (MPa)	1,000	1,000
δ (mm)	5	125
b (mm)	20	20
d (mm)	50	50
L (mm)	500	500

Table 3.14: Q and E_{error} comparison example.

	Uniaxial	3-point Bending
Q_{FC}	4.1	31.4
Q_{DC}	88.1	31.5
$E_{error,Absolute,FC}$ (MPa)	142.8	206.9
$E_{error,Absolute,DC}$ (MPa)	316.0	316.7
$E_{error,Relative,FC}$ (MPa)	208.5	305.8
$E_{error,Relative,DC}$ (MPa)	436.2	323.1

The random error implementation is expanded to assess a significant number of configurations. Figures 3.12 and 3.13 are a recreation of Figures 3.9 and 3.10, for all three simple tests and both force- and displacement-controlled test. In Figures 3.12 and 3.13, Q is replaced by the average error on the material parameter on the vertical axis. It should be noted each of the data points is the average absolute difference between the true E and E subjected to error, for a randomly generated test configuration for 10,000 generations of random relative error. Calculated using

$$E_{error,avg} = \frac{1}{10000} \sum_{i=1}^{10000} |E_{error,i}| \tag{3.38}$$

$E_{error,avg}$ is plotted against the distance from the optimal configuration for each of the randomly generated testing configurations. The distance is computed using Equation 3.30. The optimal configurations are taken from Tables 3.3, 3.6 and 3.6 for uniaxial compression, three-point bending and four-point bending respectively.

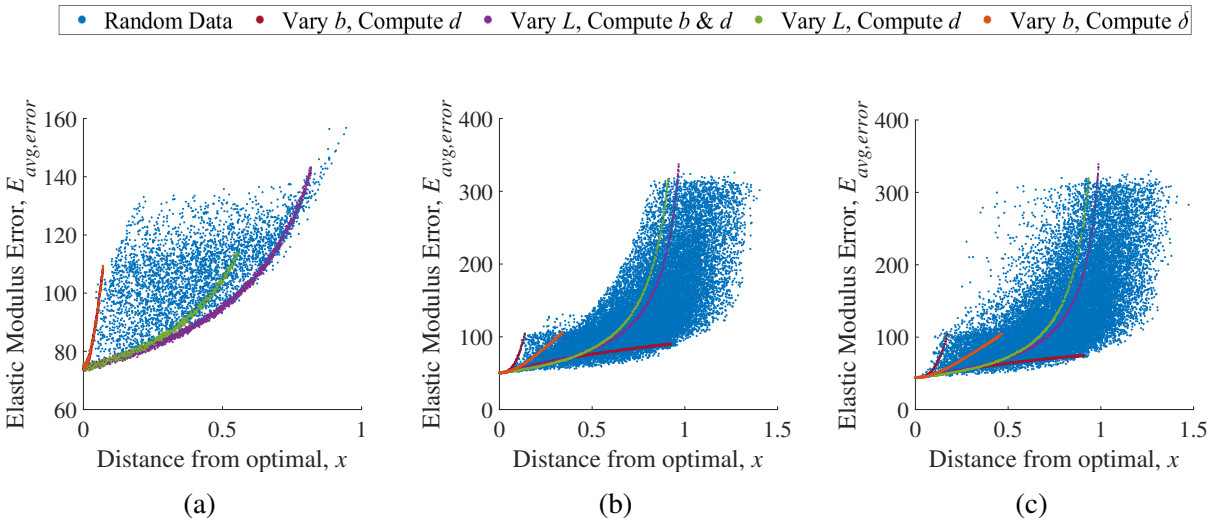

Figure 3.12: Grid search for displacement control and E = 1000 MPa and random error: (a) uniaxial compression; (b) three-point bending; (c) four-point bending.

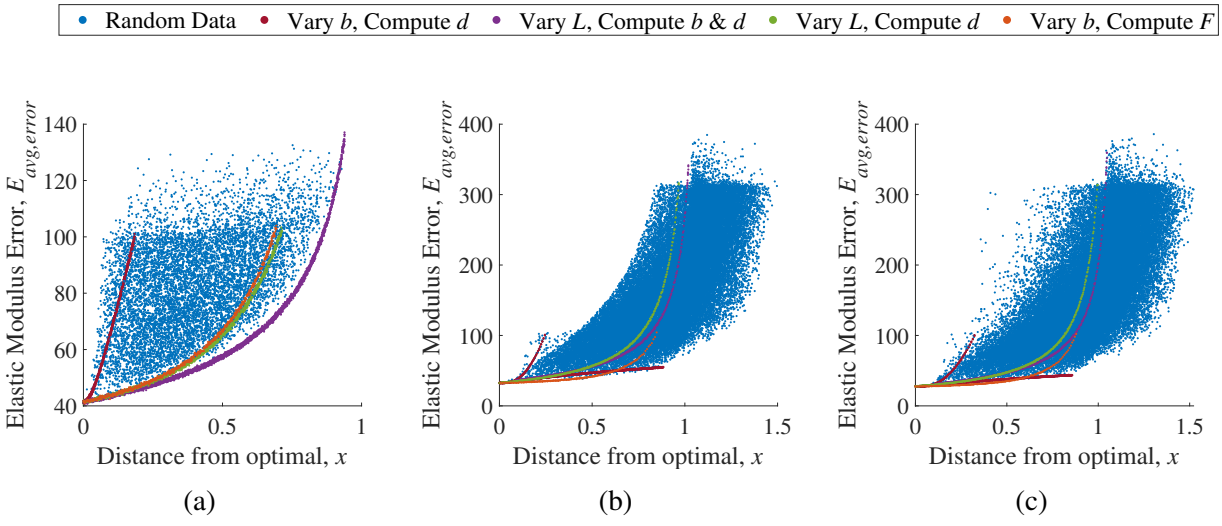

Figure 3.13: Grid search for force control and E = 1000 MPa and random error: (a) uniaxial compression; (b) three-point bending; (c) four-point bending.

Table 3.15: Probability of compared E_{error} values aligning with Q predictions. Where Test 1 is a uniaxial compression force-controlled test for E = 1000 MPa, Test 2 is a four-point bending displacement-controlled for E = 1000 MPa, and Test 3 is a three-point bending displacement-controlled test for E = 5000 MPa

	Test 1 Q = -3.5	**Test 2** Q = -1	**Test 3** Q = 46.6
Test 1 Q = -3.5	-	52.9%	**92.8%**
Test 2 Q = -1	47.8%	-	92.5%
Test 3 Q = 46.6	7.0%	7.5%	-

As can be seen in the comparison of Figures 3.9, 3.10, 3.12, and 3.13, the general trends are the same for force control (Figures 3.10 and 3.13) and displacement control (Figures 3.9 and 3.12) for both the generations of the space and overlaid plots. The increase in scatter in Figures 3.12 and 3.13 is to be expected with the implementation of random error. Furthermore, the general upward trend of $E_{error,avg}$ away from the optimal is indicative of an increase in $E_{error,avg}$ corresponding to an increase of Q.

The comparison of these plots is mostly qualitative, and in order to quantify the comparison, E_{error} values are compared directly to Q values for the same configurations. Table 3.15 compares three specific configurations and the probability of E_{error} matching the prediction of a better test by Q for three select cases. The configurations of the cases presented in Table 3.15 can be found in Tables 3.3, 3.6 and 3.6. A Monte Carlo simulation is used with 100,000 generations of random error to determine the probabilities in Table 3.15, this mathematically show as

$$Probability\, that\, E_y < E_x = \frac{frequency\, of\, E_y < E_x}{100,000} \tag{3.39}$$

where E_y is the E_{error} of the first column and E_x is the E_{error} of the first row.

As can be seen in Table 3.15, a greater difference in the Q values produces a higher probability that the lower Q will produce a lower E_{error} value. Alternatively, as the difference in the assessed Q values decreases, the probability that the lower Q will produce a lower E_{error} value approaches 50%. The upper limit of the probabilities presented in this table does not reach 100% because each

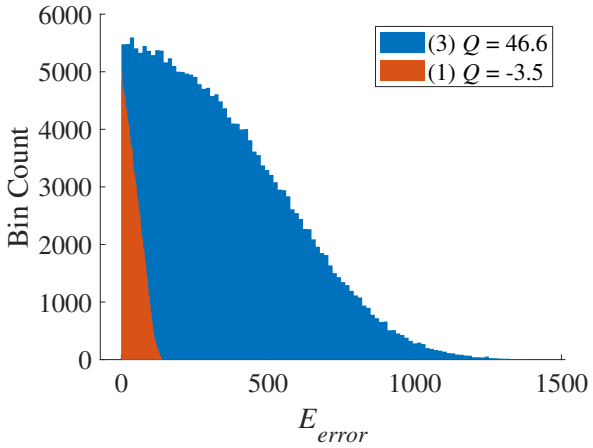

Figure 3.14: E_{error} probability distributions.

comparison of E_x and E_y is generated with random error and the resulting probability distributions of the computed values of E_{error} will always have overlap. This overlap means that there is a small probability of the test deemed suboptimal in terms of Q producing less error. The probability distributions of the values of E_{error} for Tests 1 and 3, from Table 3.15, are presented in Figure 3.14. As can be seen in this figure, the probability distribution of Test 3 presents a significantly larger E_{error} range than that of Test 1. The minimal overlap in probability distributions indicates that the probability of the E_{error} resulting from Test 1 being greater than the E_{error} produced by Test 3 is possible but will be minimal (and calculated as 7.0% probability in Table 3.15).

Finally, to show a comparison of a significantly large number of tests, Figure 3.15 presents the probability that for the comparison of two different tests the test that produces a lower Q value will also produce less error, in the form of E_{error}. This is represented as $E_y < E_x$ and $Q_y < Q_x$ will be true. This is plotted against the difference in the Q values of the two compared tests. Variables x and y denote two different tests, and uniaxial compression, three-point bending, and four-point bending are considered with both force- and displacement-controlled test conditions. Each E_x and E_y are subjected to random error and 10,000 test configurations are considered for comparison. As can be seen in Figure 3.15, an increase in the percentage difference in Q results in an increase in the accuracy of the value of Q as a measure of the better test. With the greatest accuracy approaching 85% at a maximum of approximately 60% difference in Q. The maximum probability does not

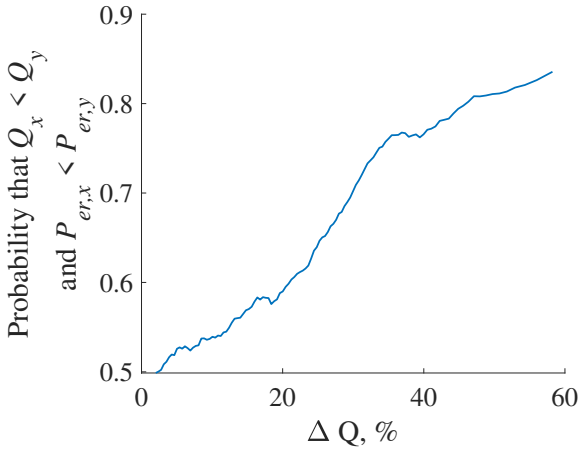

Figure 3.15: Accuracy of Q as a function of change in Q.

reach 100% for the same reasoning Figure 3.14 presents. Figure 3.15 confirms that Q can be used to compare (1) different configurations of the same test and (2) different tests entirely, although with a decrease in the ΔQ the tests approach the same quality and will be an equally good choice as an optimal test.

Furthermore, the same plot is created with the addition of the inclusion of the cantilever beam model, in addition to uniaxial compression, three- and four-point bending. This further shows that Q can be applied to different test types with different parameter choices. As the cantilever beam presents different parameter ranges, the error on the material parameter is now computed as

$$P_{er} = \left(\frac{E - E'}{E_{avg}} \right) \tag{3.40}$$

Here the unprimed material parameter is the true parameter and the primed parameter is subjected to error on the configuration. This equation is a normalized version of Equation 3.37 accounting for the different parameter ranges of the tests. Note that ν from the cantilever beam test is not considered here due to its lack of sensitivity.

Figure 3.16 presents a very similar trend to Figure 3.15, further indicating that an increase in Q will lead to a test more susceptible to error.

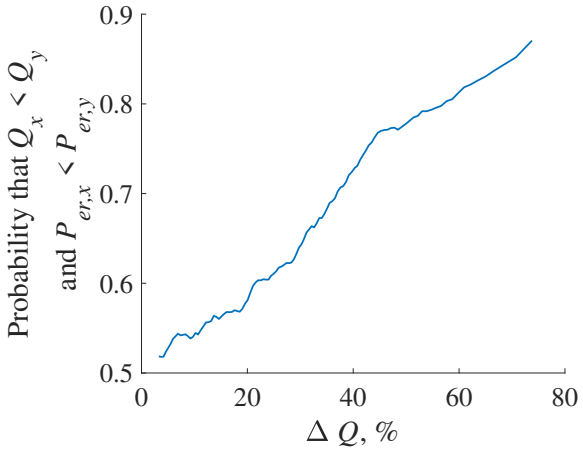

Figure 3.16: Accuracy of Q as a function of change in Q with cantilever beam.

3.6 Concluding remarks

Uniaxial compression, three-point, and four-point bending tests are used to show implementation of the quantitative metric, with each of them investigated individually as well as compared to each other. The simplicity of uniaxial compression and three-point bending allows for a direct analytical comparison of their force- and displacement-controlled test conditions. Presenting that the selection of force or displacement control in these two tests is a function of material stiffness (F/δ), as was the case for the spring extension test.

In the optimization of the quantitative metric, for all test types, three material parameters are investigated and an optimal configuration determined for each test and material type. The normalized sensitivities are found to be independent of the other parameters in the analysis. Significantly, this means that for an optimization with a constant material parameter, the normalized sensitivity of the material parameter is a constant in the quantitative metric equation. Various values of E are assessed for the optimal configuration of the test and show sample cross-section ratios (b/d) are constant within test types (uniaxial compression, three-point bending and four-point bending) while aspect ratios (L/b) increase with increasing E. This shows that for a stiffer sample the optimal configuration is more slender. Furthermore, the optimal force-to-displacement ratios (F/δ) are constant in all force control optimizations (again within each of the test types) as they optimize

to the bounds, while in displacement-controlled tests, the force-to-displacement ratio optimizes and increases with an increasing E. This is due to maximizing of the sample size and maximizing of displacement competing in the displacement-controlled tests. Slenderness ratios are further investigated with a large number of tests considered to show that a more slender sample is always desirable, and for a given slenderness ratio, a higher force-to-displacement ratios (F/δ) is more desirable.

The parameter space for each of the investigated tests is represented in two dimensions, with the normalized distance from the optimal configuration used as a single measure of comparison of quantitative metrics. Overlaid plots shows to convexity of all investigated sections of the space to have no local minimums.

Furthermore, a cantilever beam model is included to present a more complex, yet still analytical, model. The model has two material parameters yet disappointingly the ν is so insensitive that it adds little to no value to the investigation. Different parameter ranges are presented, and one observes the same general trend of an increasing L/b and increasing F/δ being desirable.

Comparisons of different tests begin with the comparison of uniaxial to three-point bending, which is a function of L, d and the output of the function (force or displacement). Lengthy equations are used to show which is preferred and their implementation is somewhat simple with known parameters. Three- and four-point bending comparisons are a function of a and the function output of force or displacement, with a much more simplistic comparison resulting. The comparison shows a direct relation between the preferred test and a, which is to be expected given this is the governing difference between these two tests. A significant conclusion from the comparison of three- and four-point bending is that in a displacement-controlled test, three-point bending is always the preferred test and for force-controlled tests, four-point bending should be used. Ultimately, for the comparison of all tests, it is found that uniaxial compression and three-point bending present very similar values for the quantitative metric. For the sample considered (stiffness similar to a stiff rubber), a force-controlled test is optimal, and uniaxial compression and three-point bending are comparable.

Empirical proof of concept is provided by applying random error to the input parameters and computing impact on the material parameter. This shows that for tests that present a lower Q, a lower error on the material parameter is computed. For the cases shown in this work, an increase in the quantitative metric, corresponding to a suboptimal test, corresponds to a larger expected error on the material parameter calculation with the implementation of random error. The probability of Q accurately predicting a test to produce less error increases as the difference in values of the Q being compared increases.

CHAPTER 4
APPLICATION AND EXPANSIONS OF THE QUANTITATIVE METRIC WITH FINITE ELEMENT ANALYSIS

The overarching objective of this thesis is to develop a methodology to design optimal soil tests. Having proposed a metric for quantifying the quality of a test in Chapter 2, and shown its implementation to simple analytical problems in Chapter 3, the next logical step is to implement the metric to finite element analysis. Finite element analysis allows the manipulation of the model to an infinite number of configurations and therefore is ideal to be able to perform a topology optimization of any material test. This chapter presents the implementation of the proposed Q to finite element analysis and is purposely kept as simple as possible. As with the previous implementation of Q, in Chapter 3, emphasis is placed here on assessing tests for known sets of material parameters. This simulates a problem where the material parameters are known or at least the material type can be estimated, and the objective is to determine the best material test of this specific type of material.

For all work completed in this chapter, a simple indenter is modeled as a force-controlled test, with a Mohr-Coulomb constitutive model and elastoplastic analysis. The analysis is coded in MATLAB and the finite element model is solved with OPTUM G2. The optimization presented uses Artley's KNITRO [118], which is again run by MATLAB. Appendix B includes details for these selections, but most notably, KNITRO is designed to solve large scale nonlinear mathematical optimization problems, with the added feature of a multi-start optimization greater confidence can be given to finding the globally optimal solution. OPTUM G2 is a geotechnical specific finite element solver which can be run from the command window, and hence it is extremely desirable for optimization due to the reduced iteration time. Future work could aim to implement a more complex finite element solver, however, caution should be used to evaluate the increased time required when running optimizations against the increase in available complexity. Finally, MATLAB

is the obvious choice for its user-freindliness and prior implementations with both KNITRO and OPTUM G2.

The intention of this chapter is to provide the next step in advancing the methodology to determine an optimal test through the application of the quantitative metric, Q. By applying Q to the analysis of a simple rectangular indenter, the analysis can remain simple enough that it can be analyzed and interpreted whilst still allowing for an added level of complexity on the work presented in Chapter 3. Section 4.1 covers details of the finite element model. Then the implementation of the quantitative metric is presented in Section 4.2. In Section 4.2, significant points which are addressed with regard to the implementation of Q include, (1) the computation of the numerical sensitivities, (2) the variation of the indenter size and the measurement location, and (3) an error analysis. An expansion for multi-parameter and measurement assessment is provided in Section 4.2. Most significantly, an optimization of the model is provided in Section 4.3. Details on the application to topology optimization are presented in Section 4.5, and a discussion on multi-material assessment is in Section 4.6.

4.1 Finite element model

The model is constructed in OptumG2, where a plane-strain elastoplastic analysis is run. A fixed load is applied to a rigid indenter that is ”wished in place” into a uniform body of soil, and displacements recorded. Simulating a force-controlled test. The bottom model boundary is fixed in the x and y directions and the vertical boundaries are fixed only in the x direction, this is known as standard fixities. The model boundaries are set sufficiently far so that they do not impact the analysis. A Mohr-Coulomb material model is used where E, ν, ϕ, and c are considered as the material parameters. Figure 4.1 shows the model, with an overall size of 30 m wide by 20 m deep. The size of the indenter (width = B and embedment depth = D) varies within the investigation. The red dots on the surface are so called results points: nodes at which simulation data are stored and can be extracted.

Upon constructing and saving the model in OptumG2, the script for running the command line

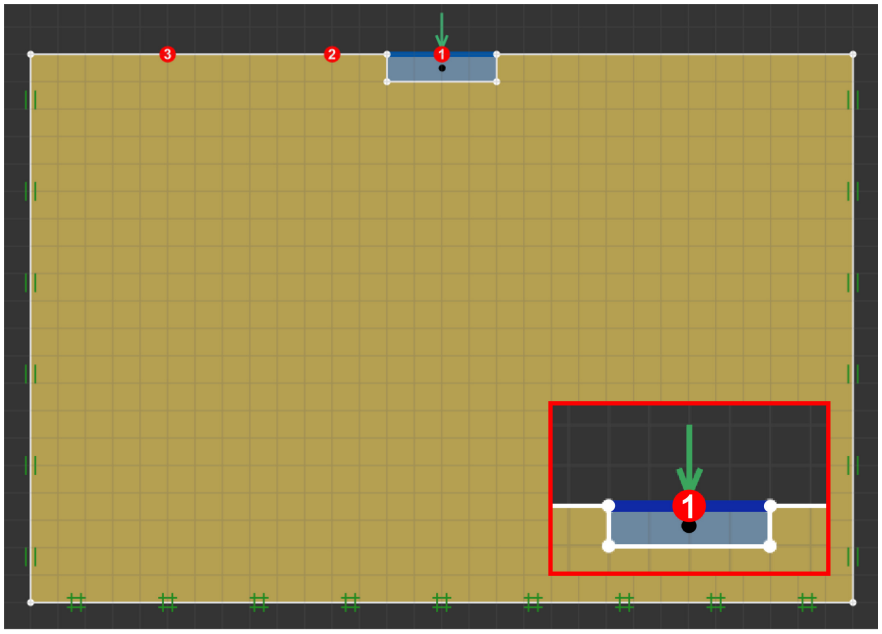

Figure 4.1: Finite element model used for implementation.

version can be accessed from the program files. All of the model parameters that are intended to be used as variables are modified in the script so they can be automatically updated by the code. A separate function is required to replace these variables with their respective values for each iteration of the analysis. Further details on this process are provided in Appendix B. The parameters used as variables in this investigation are listed with their respective bounds in Table 4.1.

For the analysis presented in this section, the material types considered are presented in Table 4.2. Cohesive, frictional and frictional-cohesive material are presented.

4.2 Implementation of optimal test assessment, using quantitative metric, to finite element analysis

Optimizing Q to find the optimal test (B, D, F and δ) to determine the material parameters (E, ν, ϕ and c) becomes significantly complicated when using finite element analysis to solve the forward model. This is in part due to the large number of components impacting the optimization, as well as the significant computation time required. The implementations provided in this section allows future work to be better informed, with expectations of results and trends, and the knowledge to

Table 4.1: Finite element model variable bounds

Parameter	Lower Bound	Upper Bound	Average $(\beta_{i,avg})$
E (MPa)	10	80	45
ν	0	0.5	0.25
ϕ (°)	0	50	25
c (kPa)	0	20	10
F (kN/m)	20	200	110
δ (m)	0.002	0.5	0.501
D (m)	0.02	1	0.51
B (m)	0.01	2	1.005

Table 4.2: Typical material parameters for use in subsections.

Parameter	Loose Sand	Soft Clay	General Fill
E (MPa)	30	15	7
ν	0.2	0.4	0.3
ϕ (°)	30	0	7
c (kPa)	0	17	7

avoid some identified pitfalls.

With no analytical forward model, the sensitivities that make up Q cannot be simply computed from partial derivatives. The computation of the numerical derivatives is outlined in Section 4.2.1. Then the assessment of the quality of various tests are compared and analysed in Sections 4.2.2 and 4.2.4 for the variation of the size of the indenter and location of measurements recorded, respectively. Section 4.2.3 presents an analysis, implementing error to the tests in order to show proof of concept of the use of Q in assessing the quality of a test.

In the subsections below it is convenient to assess a small selection of cases. For this reason, three configurations are selected which are considered representative of the parameter space defined in Table 4.1. The selected configurations are presented in Figure 4.2, where (a) is intended to be a horizontal plate-like indenter with dimensions of D = 0.05 m and B = 2 m, (b) is a vertical plate like indenter with dimensions of D = 2 m and B = 0.05 m, and (c) is intended to present a middle ground between the two, with D = 0.5 m and B = 1 m.

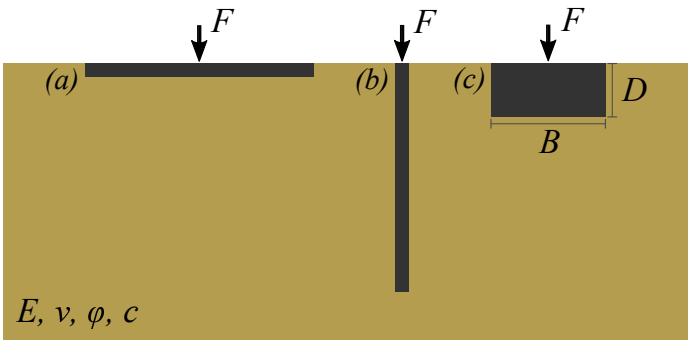

Figure 4.2: Selected indenters used for analysis.

Table 4.3: Specified parameters for selected configurations.

Configuration #	E (MPa)	ν	ϕ (°)	c (kPa)	F (kN/m)	D (m)	B (m)
1	30	0.2	30	0	50	0.05	2
2	30	0.2	30	0	50	1	0.1
3	30	0.2	30	0	50	0.5	1
4	15	0.4	0	17	50	0.05	2
5	15	0.4	0	17	50	1	0.1
6	15	0.4	0	17	50	0.5	1
7	7	0.3	7	7	50	0.05	2
8	7	0.3	7	7	50	1	0.1
9	7	0.3	7	7	50	0.5	1

4.2.1 Computed sensitivities

In order to probe the quality of a test as defined by Q, the selected configurations (Figure 4.2) are analyzed for the predetermined material types (Table 4.2). These are tabulated and numbered in Table 4.3.

The parameter sensitives are the main component of the quantitative metric, Q. Without a known forward model the partial derivatives of the parameters that are used in Q cannot simply be derived. The partial derivatives are now computed numerically, using forward finite differences to compute the slope of the functions. The normalized sensitivities which were previously computed with Equation 3.4 are now computed using

$$S_i = \left(\left(\frac{\alpha - \alpha_i}{\Delta \beta_i} \right) \left(\frac{\beta_{i,avg}}{\alpha} \right) \right)^2 \tag{4.1}$$

where $\alpha = \alpha(\beta_1, \beta_2, ..., \beta_n)$ is the true output at the true material parameters. The variable $\alpha_i = \alpha_i(\beta_1, \beta_2, ..., \beta_i + \Delta\beta_i, ..., \beta_n)$ is the output computed at a location some small distance away, where only the i^{th} parameter is altered in the computation. The variable $\Delta\beta_i$ is the finite step size used create a slightly altered β_i value resulting in a new output.

Consideration is given to specifying $\Delta\beta_i$ as an absolute or relative value, with absolute defined as $\Delta\beta_i = f(\beta_{i,avg})$ and relative defined as $\Delta\beta_i = f(\beta_i)$. Although, given that some parameters can have a zero value, a fraction of the parameter value, β_i is not possible. Therefore, the finite step is specified as a fraction of the previously specified average parameter values (Table 4.1). Trial and error is used to determine that $\Delta\beta_i = 0.05\beta_{i,avg}$ provides the most stable computation of S_i across all parameters and ranges. Figure 4.3 presents the normalized sensitivities of all of the parameters considered, across their respective ranges (Table 4.1). Poisson's ratio, ν, is not considered as a parameter of interest as a maximum of two material parameters are considered at a time and the range of ν for soils is relatively small. With such a small range, a reasonable estimation can be made independent of inverse analysis.

The normalized sensitivity plots (Figure 4.3) present many significant details, important to the implementation of Q. These plots are constructed with the configurations listed in Table 4.3, and only the parameter of interest is varied across its range. A significant complexity that the finite element analysis introduces is that each parameter sensitivity is now dependent on the other parameters. Most significantly this means that now even when the material parameters are fixed, their normalized sensitivities influence the optimization, which was not the case in Chapter 3. For all of the parameters except E, the value of S_i for a given parameter is a function of the configuration of the test, highlighted by the differing plots of S_i within each subplot for the different configurations. For ϕ in Figure 4.3c the general trend remains that typically a lower parameter leads to a higher sensitivity, although some parameters and configurations do not comply with this. Considering the S_i values for ϕ, for example configurations 1 and 3 are the same material and

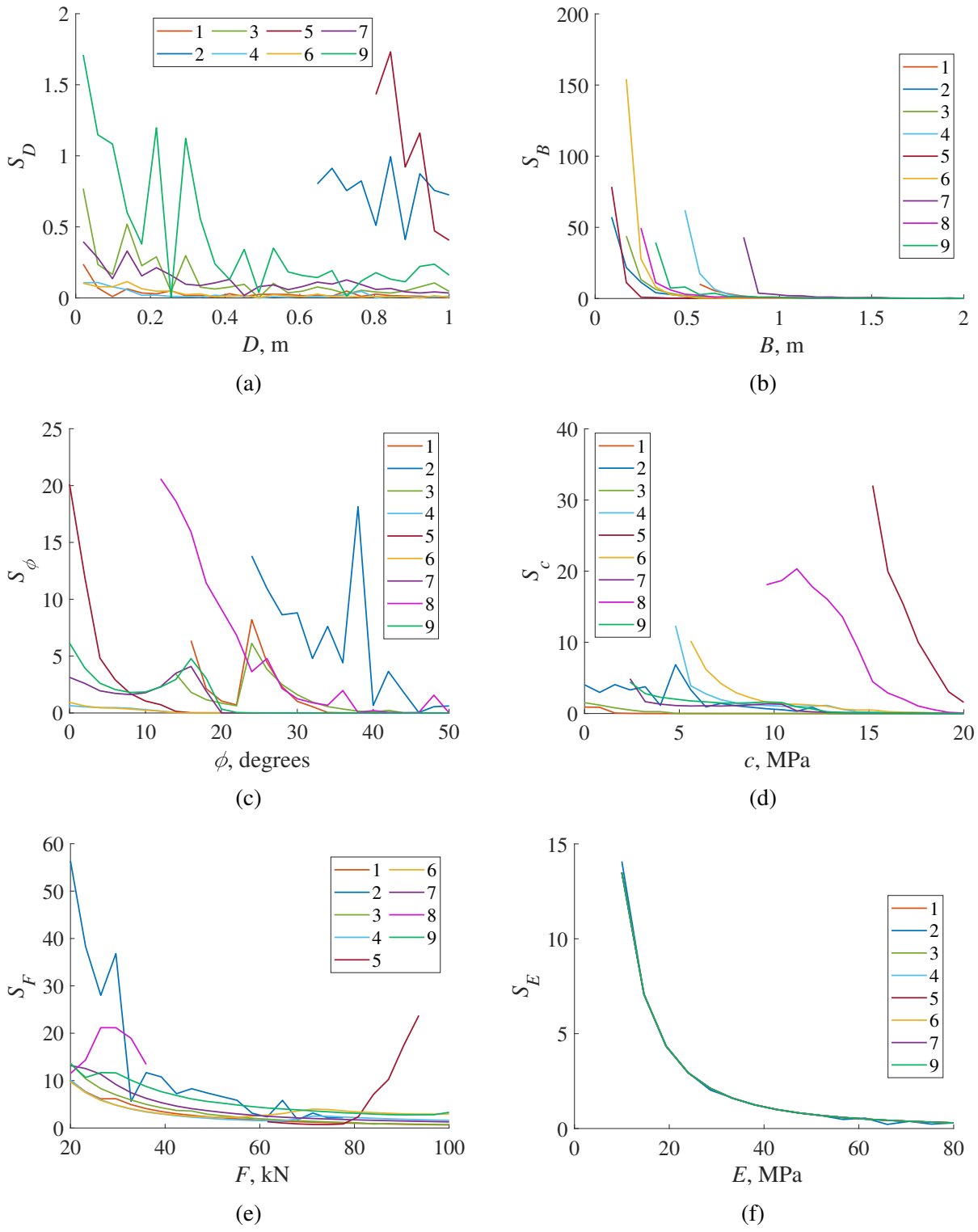

Figure 4.3: Normalized parameter sensitivities for predetermined configurations: (a) D; (b) B; (c) ϕ; (d) c; (e) F; (f) E.

present a sharp peak around 24° while configurations 7 and 9 are another material with a softer peak around 17°. This indicates that for these ϕ values there are other material parameters that are constant across these sensitivity plots and have a strong cross correlation, more than likely with E. As the computation of Q is a function of all of these plots, the comparison between trends in Q and more broadly the optimization of Q, is a non-trivial task.

4.2.2 Computation of the quantitative metric for varying indenter size

The calculation of Q uses weightings to designate parameter sensitivities to be minimized and maximized. All material parameter sensitivities are given a weighting of negative one to be maximized and all non-material parameter sensitivities assigned one such that they are minimized. This results in

$$Q = \frac{1}{7}\Bigg[- \left(\frac{\partial\delta}{\partial E}\frac{E_{avg}}{\delta}\right)^2 - \left(\frac{\partial\delta}{\partial \nu}\frac{\nu_{avg}}{\delta}\right)^2 - \left(\frac{\partial\delta}{\partial \phi}\frac{\phi_{avg}}{\delta}\right)^2 - \left(\frac{\partial\delta}{\partial c}\frac{c_{avg}}{\delta}\right)^2 + \left(\frac{\partial\delta}{\partial F}\frac{F_{avg}}{\delta}\right)^2 + \left(\frac{\partial\delta}{\partial B}\frac{B_{avg}}{\delta}\right)^2 + \left(\frac{\partial\delta}{\partial D}\frac{D_{avg}}{\delta}\right)^2 \Bigg] \tag{4.2}$$

for a case where it is considered that all the material parameters should be determined.

Equation 4.1 can be further broken down to include the details of the calculation of the parameter sensitivities, as presented in Section 4.2, resulting in

$$Q = \frac{1}{7}\Bigg[- \left(\frac{\delta - \delta_{E+\Delta E}}{\Delta E}\frac{E_{avg}}{\delta}\right)^2 - \left(\frac{\delta - \delta_{\nu+\Delta\nu}}{\Delta \nu}\frac{\nu_{avg}}{\delta}\right)^2 - \left(\frac{\delta - \delta_{\phi+\Delta\phi}}{\Delta \phi}\frac{\phi_{avg}}{\delta}\right)^2 - \left(\frac{\delta - \delta_{c+\Delta c}}{\Delta c}\frac{c_{avg}}{\delta}\right)^2 + \left(\frac{\delta - \delta_{F+\Delta F}}{\Delta F}\frac{F_{avg}}{\delta}\right)^2 + \left(\frac{\delta - \delta_{B+\Delta B}}{\Delta B}\frac{B_{avg}}{\delta}\right)^2 + \left(\frac{\delta - \delta_{D+\Delta D}}{\Delta D}\frac{D_{avg}}{\delta}\right)^2 \Bigg] \tag{4.3}$$

However, as was shown in Section 4.2.1, many of the parameter sensitivities are non-smooth and non-convex. Therefore, the assessment of Q as a function of all the parameter sensitivities is very complex. For this reason, Q is computed for the determination of one material parameter at a

Table 4.4: Analysis of Q for determining E. Bold text highlights the values of Q.

Configuration #	δ (m)	Q	S_D	S_B	S_E	S_F
1	0.003	**0.13**	0.08	0.17	-1.7	2.37
2	0.021	**4.54**	0.96	25.12	-1.69	7.22
3	0.004	**0.24**	0.05	0.48	-1.7	2.87
4	0.007	**-0.45**	0.1	0.05	-5.31	2.03
5	0.022	**55.5**	2.93	25.18	-5.33	365.76
6	0.007	**-0.4**	0.01	0.04	-5.33	2.46
7	0.024	**-1.59**	0.29	0.19	-15.31	3.67
8	-	-	-	-	-	-
9	0.029	**-1.23**	0.11	0.62	-15.31	5.94

Table 4.5: Analysis of Q for determining ϕ. Bold text highlights the values of Q.

Configuration #	δ (m)	Q	S_D	S_B	S_ϕ	S_F
1	0.003	**0.24**	0.08	0.17	-0.95	2.37
2	0.021	**3.84**	0.96	25.12	-6.39	7.22
3	0.004	**0.3**	0.05	0.48	-1.29	2.87
4	0.007	**0.22**	0.1	0.05	-0.6	2.03
5	0.022	**54.3**	2.93	25.18	-13.79	365.76
6	0.007	**0.25**	0.01	0.04	-0.72	2.46
7	0.024	**0.38**	0.29	0.19	-1.53	3.67
8	-	-	-	-	-	-
9	0.029	**0.71**	0.11	0.62	-1.71	5.94

time. For ϕ, this is presented as

$$Q = \frac{1}{4}\left[-\left(\frac{\delta - \delta_{\phi+\Delta\phi}}{\Delta\phi}\frac{\phi_{avg}}{\delta}\right)^2 + \left(\frac{\delta - \delta_{F+\Delta F}}{\Delta F}\frac{F_{avg}}{\delta}\right)^2 + \left(\frac{\delta - \delta_{B+\Delta B}}{\Delta B}\frac{B_{avg}}{\delta}\right)^2 + \left(\frac{\delta - \delta_{D+\Delta D}}{\Delta D}\frac{D_{avg}}{\delta}\right)^2\right] \tag{4.4}$$

Tables 4.4, 4.5 and 4.6 present the analysis and computation of Q for all of the configurations in Table 4.3 and for E, ϕ and c, respectively. Note that for each of the tables, δ, S_D, S_B and S_F do not change and are presented in each of the tables to provide ease of comparison.

Table 4.6: Analysis of Q for determining c. Bold text highlights the values of Q.

Configuration #	δ (m)	Q	S_D	S_B	S_c	S_F
1	0.003	**0.27**	0.08	0.17	-0.73	2.37
2	0.021	**4.33**	0.96	25.12	-3.61	7.22
3	0.004	**0.3**	0.05	0.48	-1.27	2.87
4	0.007	**0.29**	0.1	0.05	-0.11	2.03
5	0.022	**54.8**	2.93	25.18	-10.18	365.76
6	0.007	**0.33**	0.01	0.04	-0.17	2.46
7	0.024	**0.45**	0.29	0.19	-1.02	3.67
8	-	-	-	-	-	-
9	0.029	**0.75**	0.11	0.62	-1.39	5.94

In analyzing Tables 4.4, 4.5 and 4.6, trends can be identified in the various tests across the material parameters of interest. Note that in all cases the finite element simulation of configuration 8 failed, due to the applied force exceeding the capacity of the place. In almost all cases, with the exception of configurations 7 and 9 when determining E, the values of Q are ordered such that the wide shallow indenter (configurations 1, 4 and 9) are optimal followed by the box like indenter (configurations 3, 6 and 9). Finally, the least desirable tests are the narrow deep indenters (configurations 3 and 6). This is consistent with the displacement, with a lower Q also meaning a lower displacement. Furthermore, the Q values are ordered such that the tests determining E give the lowest, followed by ϕ, and then c. This is seen in the values of the sensitivities, where S_D, S_B and S_F are the same for all each of the tables, and S_E has the largest values which are constant across material types.

Finally, presented thus far in this chapter are tests where only a single measurement is taken, such that only a single material parameter can be assessed for each test. In order to include alternative/additional measurements, Section 4.2.4 assesses the impact of measurement location on the computation of Q.

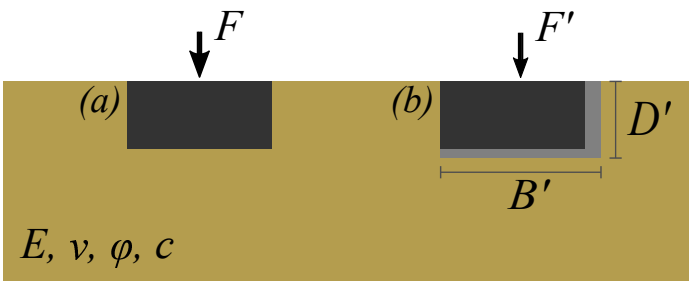

Figure 4.4: Application of quantitative metric.

4.2.3 Error analysis

Similar to Section 3.5, this section is provided to show that Q works as intended, even after the implementation to finite element analysis. The metric Q works to quantify the quality of a test, with a better quality test able to more accurately retrieve the material parameters. For example, consider Figure 4.4, when an inverse analysis is used to determine the material parameters there are many factors which influence the accuracy of the result. The factor that is addressed with Q is that, in the real test, it is assumed that measurements are perfectly accurate (configuration (a) in Figure 4.4). Although, it is likely that these are not perfect, and in reality configuration (b) is more likely, with each parameter in the configuration being different to its actual value. The purpose of Q is to identify tests which are less sensitive to these errors and more sensitive to the material parameters of interest. This means that if the two tests in Figure 4.4 were used in an inverse analysis to determine the material parameters, the difference between the returned material parameters should be comparable to the values of Q. In other words a configuration with a lower Q should also return a lower difference in the computed material parameters. The difference between this section and Section 3.5 is that here an error on a material parameter cannot be directly computed and an inverse analysis is required to complete the same process previously described in Equation 3.37.

Four configurations are selected, based on their Q values, and error is applied to the configurations to determine the resulting error on the material parameter. Configurations 1, 3, 7 and 9 from Table 4.3 are used with the objective of determining ϕ. A error is applied to B, D and F, equal to 10% of the material parameter ranges. A new ϕ is determined, ϕ', which will return the

Table 4.7: Computed material parameter errors for fixed input error.

Configuration	Q	$\lvert\phi - \phi'\rvert$ (°)
1	0.24	0.94
3	0.3	0.48
7	0.38	0.83
9	0.71	0.69

Table 4.8: Probabilistic analysis for proof of concept of Q implementation. Bold text highlights the values of Q.

	1 $Q = 0.24$	**3** $Q = 0.3$	**7** $Q = 0.38$	**9** $Q = 0.71$
1, $Q = 0.24$	-	53%	59%	60%
3, $Q = 0.3$	47%	-	59%	61%
7, $Q = 0.38$	41%	41%	-	54%
9, $Q = 0.71$	40%	39%	46%	-

same displacement for the as the original configuration. The quantity $\phi - \phi'$ is the error on the material parameter caused by the errors applied to the configuration. When a test with a lower Q also reports a lower error, Q is working as it is intended.

As seen in Table 4.7, it appears that Q does not perform as desired for the case of configurations 1 and 3, with 1 reporting a lower Q but higher error. Furthermore, configuration 9 presents the second lowest error but highest Q value. It was found that different errors can have varying effects on the different configurations. To address this, a probabilistic approach is taken. A random error is applied, bounded by $\pm 5\%$ of the material parameter range, to B, D and F. The process of determining the new ϕ' is completed 36 times with the same random errors applied to configurations 1 and 3, and a different set of random errors applied to configurations 7 and 9. Two configurations are compared by assessing the probability that any one of the 36 results in one configuration will be less than any one of the 36 results in the other configuration. The summed probabilities are presented in Table 4.8.

In all cases the test with a lower Q value presents a higher probability that the error will be

Table 4.9: Analysis of Q for determining E with measurement at $0.5B$ from indenter edge. Bold text highlights the values of Q.

Configuration #	δ (m)	Q	S_D	S_B	S_E	S_F
1	0.001	**-0.06**	0.01	0.1	-1.7	1.18
2	0.003	**0.64**	4.44	0.00	-1.63	1.65
3	0.002	**0.01**	0.00	0.30	-1.7	1.46
4	0.004	**-0.49**	0.00	0.12	-5.33	1.78
5	0.011	**0.7**	0.22	3.49	-5.32	6.54
6	0.006	**-0.44**	0.00	0.13	-5.33	2.11
7	0.008	**-2.04**	0.03	0.22	-15.31	0.8
8	-	-	-	-	-	-
9	0.014	**-2.03**	0.00	0.36	-15.31	0.71

lower. Additionally, with an increase in the difference in the Q values there is an increase in the probabilities. However, these probabilities are not too far from 50%, indicating that for the configurations considered, all will give a similar quality estimate of the material parameter. This is to be expected given that they are all similar rectangular indenters.

4.2.4 Variation of measurement location

All displacements presented in this chapter until now refer only to the displacement of the indenter. Different measurements of nodes can be taken from different locations in the model. As these different locations are characterized by different behaviors they can produce different trends that in turn can particularly benefit the multi-parameter assessment.

Tables 4.9, 4.10, and 4.11 present the same analysis as shown in Tables 4.4, 4.5 and 4.6, although now the measurement used to determine the sensitivities is the vertical displacement the surface node located $0.5B$ from the edge of the indenter.

In all cases the tests which use the vertical displacement of a node located $0.5B$ from the edge of the indenter produce a lower Q value. By assessing the values of the sensitivities presented in Tables 4.9, 4.10 and 4.11 in comparison to those in Tables 4.4, 4.5 and 4.6, it can be seen that the main factor influencing the decline in Q values is the significant decrease in the S_D, S_B and S_F

Table 4.10: Analysis of Q for determining ϕ with measurement at $0.5B$ from indenter edge. Bold text highlights the values of Q.

Configuration #	δ (m)	Q	S_D	S_B	S_ϕ	S_F
1	0.001	**0.14**	0.01	0.1	-0.31	1.18
2	0.003	**0.99**	4.44	0.00	-0.33	1.65
3	0.002	**0.25**	0.00	0.30	0.00	1.46
4	0.004	**0.18**	0.00	0.12	-0.64	1.78
5	0.011	**1.03**	0.22	3.49	-3.07	6.54
6	0.006	**0.21**	0.00	0.13	-0.79	2.11
7	0.008	**0.15**	0.03	0.22	0.00	0.8
8	-	-	-	-	-	-
9	0.014	**0.13**	0.00	0.36	-0.16	0.71

Table 4.11: Analysis of Q for determining c with measurement at $0.5B$ from indenter edge. Bold text highlights the values of Q.

Configuration #	δ (m)	Q	S_D	S_B	S_c	S_F
1	0.001	**0.16**	0.01	0.1	-0.13	1.18
2	0.003	**0.92**	4.44	0.00	-0.18	1.65
3	0.002	**0.25**	0.00	0.30	0.00	1.46
4	0.004	**0.26**	0.00	0.12	-0.07	1.78
5	0.011	**1.26**	0.22	3.49	-1.43	6.54
6	0.006	**0.3**	0.00	0.13	-0.16	2.11
7	0.008	**0.13**	0.03	0.22	-0.14	0.8
8	-	-	-	-	-	-
9	0.014	**0.15**	0.00	0.36	0.00	0.71

values. Furthermore, there is a decrease in the values of S_ϕ and S_c although, aside from where these values are zero they are still relatively similar to the other sensitivities included in the computation of Q.

In addition to the analysis presented above for the displacement at $0.5B$, the vertical displacement of a node $2B$ from the edge of the indenter was also considered. The $2B$ location was deemed infeasible, as there was insufficient displacement (< 1 mm). The use of the sensitivity of the parameters to the displacement of a node $0.5B$ from the edge of the indenter is included in Section 4.3 where multiple parameters and measurements are considered simultaneously.

4.3 Multi-parameter assessment and impact of correlation

Additional considerations need to be made before Q is implemented to multi-parameter problems. Multi-parameter can be in the form of multiple measurements (in this case displacements) or assessing a test for its ability to determine multiple material parameters. The previous section assessed only a single material parameter and a single measurement at a time. Complexities arise when more than one material parameter is required to be determined from a test at a time. When two material parameters are assessed and only one measurement is taken, parameters can be non-unique with multiple combinations of the material parameters returning the same test output. The current construction of Q to assess the quality of a test does not account for the correlation of material parameters, although by ensuring as many measurements are taken as material parameters desired, the impact can be minimized. To include multiple measurements in the assessment of test quality with Q the following equation should be used

$$Q = \frac{1}{mn} \sum_{j=1}^{m} \sum_{i=1}^{n} w_i \left[\left(\frac{\partial \alpha_j}{\partial \beta_i} \right) \left(\frac{\beta_{i,avg}}{\alpha_j} \right) \right]^2 \tag{4.5}$$

where m is the number of measurements considered.

For the assessment of ϕ and c using the measurements of indenter displacement, δ_i, and the vertical displacement of a node $0.5B$ from the indenter, δ_n, the quantitative metric is computed

using

$$
\begin{aligned}
Q = \frac{1}{10}\Bigg[& -\left(\frac{\delta_i - \delta_{i,\phi+\Delta\phi}}{\Delta\phi}\frac{\phi_{avg}}{\delta_i}\right)^2 - \left(\frac{\delta_i - \delta_{i,c+\Delta c}}{\Delta c}\frac{c_{avg}}{\delta_i}\right)^2 + \left(\frac{\delta_i - \delta_{i,F+\Delta F}}{\Delta F}\frac{F_{avg}}{\delta_i}\right)^2 \\
& + \left(\frac{\delta_i - \delta_{i,B+\Delta B}}{\Delta B}\frac{B_{avg}}{\delta_i}\right)^2 + \left(\frac{\delta_i - \delta_{i,D+\Delta D}}{\Delta D}\frac{D_{avg}}{\delta_i}\right)^2 - \left(\frac{\delta_n - \delta_{n,\phi+\Delta\phi}}{\Delta\phi}\frac{\phi_{avg}}{\delta_n}\right)^2 \\
& - \left(\frac{\delta_n - \delta_{n,c+\Delta c}}{\Delta c}\frac{c_{avg}}{\delta_n}\right)^2 + \left(\frac{\delta_n - \delta_{n,F+\Delta F}}{\Delta F}\frac{F_{avg}}{\delta_n}\right)^2 + \left(\frac{\delta - \delta_{B+\Delta B}}{\Delta B}\frac{B_{avg}}{\delta}\right)^2 \\
& + \left(\frac{\delta - \delta_{D+\Delta D}}{\Delta D}\frac{D_{avg}}{\delta}\right)^2\Bigg]
\end{aligned}
\tag{4.6}
$$

In order to assess the impact of multiple measurements on correlation, consider the conventional inverse problem. In this inverse problem, the objective is to determine the material parameters (ϕ and c) by minimizing the error between simulated and known measurements (indenter and nodal displacements). The objective function in this case is

$$SSE = \sum_{i=1}^{n}(y_i - y_i')^2 \tag{4.7}$$

where n is the number of measurements (in this case displacements), y_i are the true displacements, and y_i' are the displacements for the trial material parameters.

Figure 4.5 presents an assessment of the inverse problem for configuration 7 (Table 4.3), where the surface is constructed and plotted in 2D using Equation 4.7. In Figure 4.5 red dots indicate the minimum values and the contour lines the value of SSE. For both cases in which only one measurement is used, there is significant cross correlation, and this is reduced when two measurements are included (Figure 4.5c). Furthermore, Table 4.12 presents all of the Q values for the multi-parameter assessment for determining ϕ and c. The same trends are presented as were shown in Tables 4.5 and 4.6 for the single parameter assessments. Appendix A presents preliminary work which considered the shape of the inverse model.

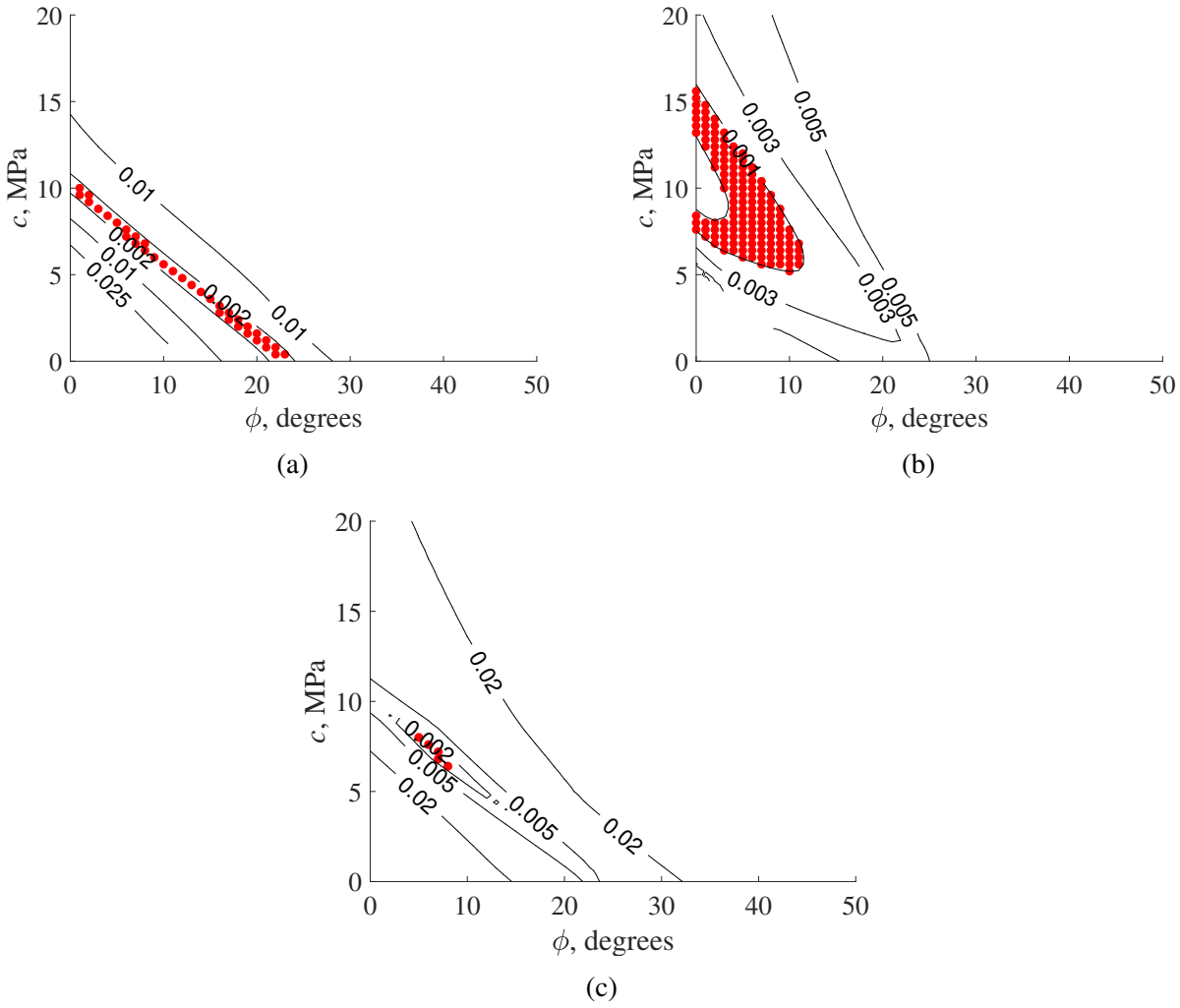

Figure 4.5: Constructed inverse models for: (a) indenter displacement; (b) nodal displacement $0.5B$ from indenter edge; (c) combined indenter and nodal displacement. Contours indicate SSE value from Equation 4.7 and red dots are minima.

Table 4.12: Analysis of Q for determining ϕ and c.

Configuration #	Indenter displacement (m)	Nodal displacement (m)	Q
1	0.003	0.001	0.13
2	0.021	0.003	2.1
3	0.004	0.002	0.19
4	0.007	0.004	0.19
5	0.022	0.011	26.84
6	0.007	0.006	0.21
7	0.024	0.008	0.18
8	-	-	-
9	0.029	0.014	0.32

4.4 Optimization of indenter for material parameter determination

While Q can always be used to compare tests as specified in the sections above, the overarching objective of this analysis is to determine a methodology for specifying optimal material tests. One of the most important steps of implementing Q to finite element analysis is to complete the optimization to find the optimal test for determining the material parameters. As previously stated, the optimization is run through MATLAB, using KNITRO to execute the optimization and OptumG2 to complete the finite element calculations. All the features of this analysis are detailed in Appendix B.

Figure 4.6 gives an overview of the integration between the software for the intended application. The input parameters are delivered to MATLAB which then calls on KNITRO. KNITRO then iterates the parameters, using OptumG2 to compute the updated output each time. Once the specified optimization constraints are met, KNITRO will return the optimized parameters.

An optimization is completed to determine the optimal configuration (B and D) for determining the material parameters, ϕ and c, for the material characterized in Table 4.2 as general fill. The optimization minimizes Q as computed using equation 4.6. The result is an indenter of dimensions B = 1.92 m and D = 0.02 m, which produces an optimum Q of 0.176. This is a significant step in achieving the aims of this chapter and the overarching objective of the thesis.

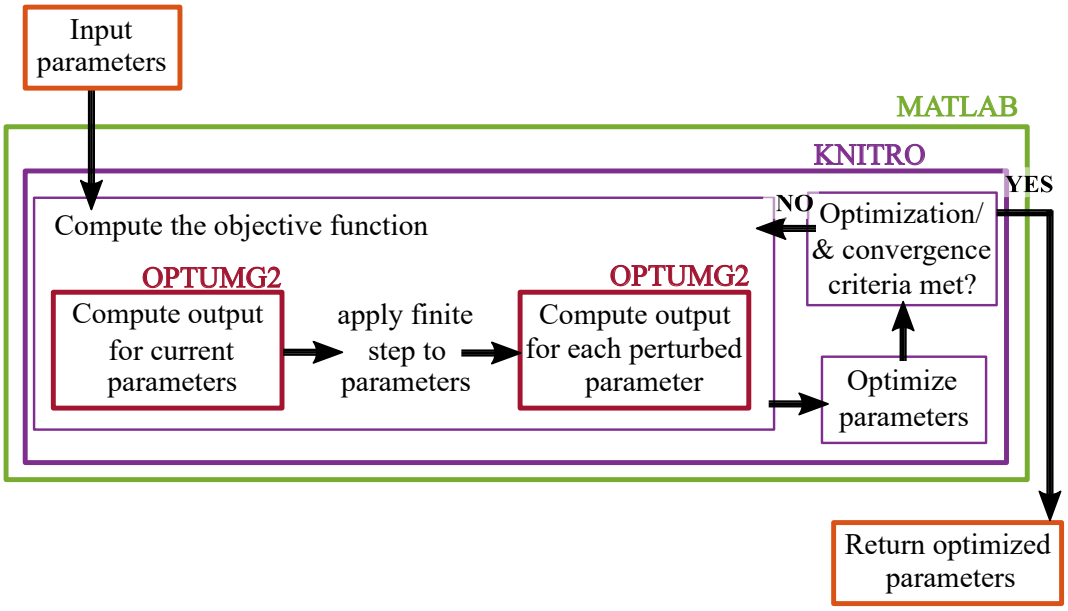

Figure 4.6: Integration of software for optimization.

To expand further, with the dependence of Q on the sensitivities of all the model input parameters, it is difficult to assess the convergence of an optimized configuration, as Q is a function of five variables — the sensitivities of ϕ, c, D, B and F. In order to best assess the optimization space of the optimization presented above, Figure 4.7 shows the variation of Q across the range of the optimized parameters, D and B. Figure 4.7 effectively presents the objective function of the optimization. It can be seen, that as expected a decrease in B leads to a sharp increase in value of Q. This is due to the larger magnitude S_B as presented in Figure 4.3b. Furthermore, the plot does not extend into the lower values of B as the computation was not possible. There are fluctuations throughout the surface causing a noisy function which is represented as the irregular contour lines. The optimal solution as determined above, lies towards the bottom right corner of Figure 4.7. Finally, an interesting finding of this surface is that there is a strong local minimum in the area of B = 2 m and D = 1 m. The total magnitude of the change in Q along the right-hand edge, where B = 2 m, is only about 0.05. With such a small magnitude, it is likely this local minimum is caused by a dip in one of the normalized sensitivity values.

It is acknowledged that Q in the current form cannot account for the cross correlation of parameters. Figure 4.8 presents the objective function of the inverse model of the optimized configura-

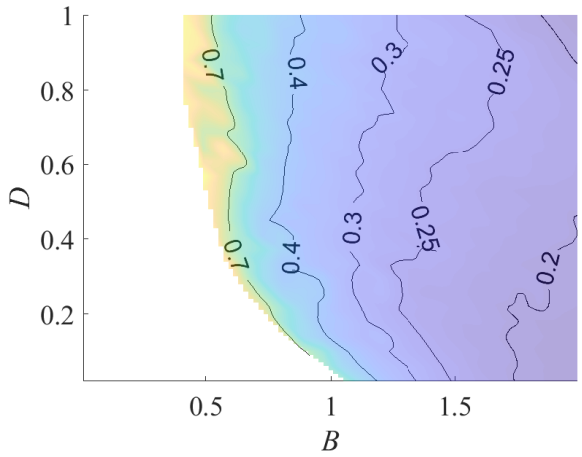

Figure 4.7: Representation of Q across optimization space. Contours give indication to the non-convexity of the surface.

tion, and although there is some cross correlation, indicated by the parallel contour lines, although, there is a unique solution. In Figure 4.8, the filled circle indicates the minimum and the open circles are locations identified to have SSE of less than 0.5 mm.

4.5 Investigation of indenter shape

In order to specify an optimal test for a given set of material parameters, the whole test must be allowed to change in a mostly unrestricted way, removing the constraint that the indenter must be rectangular. This process has objectives that are most similar to those found in the field of topology optimization, where the topology of the problem is varied to achieve the optimal design. To implement topology optimization to the problem of discovering optimal soil tests, how the sensitivity of the shape of the indenter to the model output must be re-framed. Where previously it was simply the indenter dimensions, it would now be convenient to specify the position of each node of the indenter. Previously, β = [E, ν, ϕ, c, D, B] and now, by characterizing the shape of the indenter by the nodes, this is modified to β = [E, ν, ϕ, c, $n_{1,x}$, $n_{1,y}$, $n_{2,x}$, $n_{2,y}$, $n_{3,x}$, $n_{3,y}$, $n_{4,x}$, $n_{4,y}$, $n_{5,x}$, $n_{5,y}$], for an indenter characterized by five nodes. This general configuration is presented in Figure 4.9. In this general form the sensitivity of all of the nodes in both the x and y directions are considered. An attempt was made to complete the optimization of this analysis,

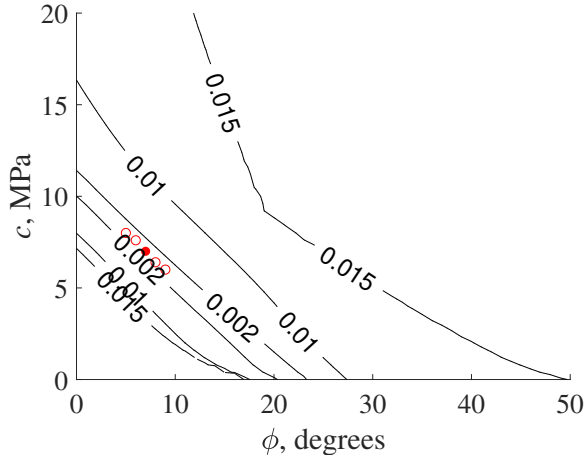

Figure 4.8: Representation of the inverse problem for the optimized configuration. Contours indicate SSE value from Equation 4.7.

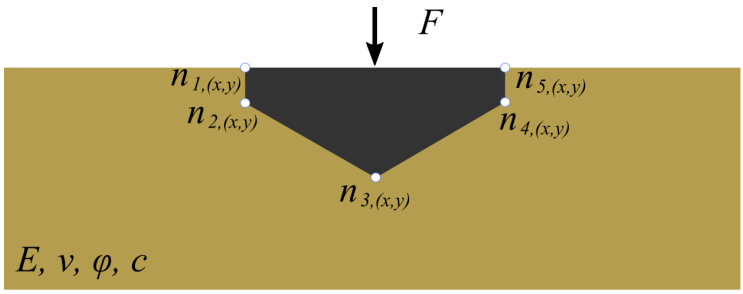

Figure 4.9: Labeling convention used for indenters.

although it was found that this analysis would require immense computational time. In this section, a predetermined six configurations are compared, these are presented in Figure 4.10. Here the indenters are characterized by five nodes and are configured such that for the shapes presented they have a constant area.

Analysis of Q for determining ϕ and c of the indenters presented in Figure 4.10 is shown in Tables 4.13, 4.14, and 4.15. Table 4.13 gives the geometry of the indenters along with the computed displacements and Q values. Tables 4.14 and 4.15 show the individual parameter sensitivities relative to the indenter and nodal displacements, respectively. Where the indenter displacement, δ_i, is the displacement of the indenter and the nodal displacement, δ_n, is the vertical displacement of a node $0.5B$ from the edge of the indenter. The same force is applied to all indenters (F = 50 kN) and the material classified as the general fill shown in Table 4.2. The indenters are centered

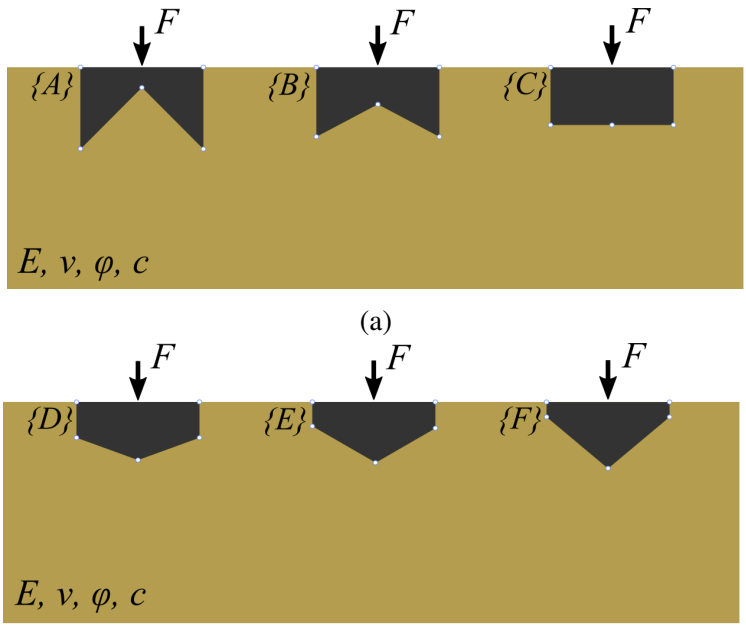

Figure 4.10: Select indenters for analysis of varying shape, indenters: (a) A to C; (b) D to F.

on the upper surface of the model, and with a coordinate system of the bottom left of the model being the origin, the center of the indenter has coordinates of x = 15 m, y = 20 m. The nodes are numbered such that left-hand surface node is n_1 and the nodal numbering follows in an counter-clockwise direction around the indenter, as shown in Figure 4.9. The y coordinates of nodes one and five are not considered in the analysis as they are considered to be fixed in the analysis.

Most significantly, the resulting optimal configuration among the six considered here is configuration D. With constant force, there is an increasing indenter displacement, δ_i, as the indenter

Table 4.13: Analysis of Q for determining ϕ and c: indenter coordinates, displacements and Q.

	$n_{1,x}$ (m)	$n_{2,x}$ (m)	$n_{3,x}$ (m)	$n_{4,x}$ (m)	$n_{5,x}$ (m)	$n_{2,y}$ (m)	$n_{3,y}$ (m)	$n_{4,y}$ (m)	δ_i (m)	δ_n (m)	Q
A	14.5	14.5	15	15.5	15.5	19.4	19.6	19.4	0.028	0.014	0.168
B	14.5	14.5	15	15.5	15.5	19.25	19.75	19.25	0.027	0.014	0.163
C	14.5	14.5	15	15.5	15.5	19.5	19.5	19.5	0.029	0.014	0.155
D	14.5	14.5	15	15.5	15.5	19.6	19.4	19.4	0.031	0.013	0.146
E	14.5	14.5	15	15.5	15.5	19.75	19.25	19.75	0.033	0.013	0.190
F	14.5	14.5	15	15.5	15.5	19.9	19.1	19.9	0.037	0.012	0.216

Table 4.14: Parameter sensitivities to indenter displacement for the analysis of Q for determining ϕ and c.

	$S_{n,1,x}$	$S_{n,2,x}$	$S_{n,3,x}$	$S_{n,4,x}$	$S_{n,5,x}$	$S_{n,2,y}$	$S_{n,3,y}$	$S_{n,4,y}$	S_ϕ	S_c	S_F
A	0.005	0.108	0.001	0.117	0.004	0.007	0.011	0.000	-1.56	-1.29	5.66
B	0.003	0.108	0.000	0.019	0.001	0.006	0.018	0.003	-1.41	-1.21	5.40
C	0.001	0.078	0.000	0.033	0.000	0.007	0.027	0.027	-1.61	-1.30	5.88
D	0.013	0.084	0.000	0.039	0.001	0.000	0.009	0.002	-1.91	-1.51	6.34
E	0.013	0.135	0.006	0.106	0.001	0.037	0.003	0.032	-2.54	-2.03	8.73
F	0.001	0.147	0.007	0.118	0.000	0.063	0.028	0.040	-3.40	-2.60	10.96

Table 4.15: Parameter sensitivities to nodal displacement for the analysis of Q for determining ϕ and c.

	$S_{n,1,x}$	$S_{n,2,x}$	$S_{n,3,x}$	$S_{n,4,x}$	$S_{n,5,x}$	$S_{n,2,y}$	$S_{n,3,y}$	$S_{n,4,y}$	S_ϕ	S_c	S_F
A	0.000	0.323	0.041	0.127	0.023	0.022	0.063	0.057	-0.25	-0.01	0.89
B	0.000	0.357	0.000	0.004	0.002	0.005	0.037	0.015	-0.22	0.00	1.10
C	0.001	0.149	0.000	0.020	0.006	0.057	0.080	0.064	-0.15	0.00	0.66
D	0.040	0.058	0.013	0.008	0.001	0.001	0.000	0.029	-0.10	-0.01	0.69
E	0.021	0.196	0.023	0.040	0.032	0.085	0.025	0.002	0.00	-0.14	0.16
F	0.004	0.074	0.018	0.016	0.025	0.001	0.001	0.002	0.00	-0.13	0.24

moves from a more inverse wedge-like shape (configurations A and B) to a more wedge (configurations D, E and F). With the increase in indenter displacement, there is a decrease in the displacement of the adjacent material node δ_n. As the indenter moves from inverse wedge to wedge, the indenter penetrates with the greatest of ease and creates less disturbance to the surrounding material. This is presented in Table 4.13. This results from the combination of different parameter sensitivities coming from different configurations. For example, in Table 4.14 the normalized parameter sensitivities of ϕ and c, S_ϕ and S_c, present a strong trend towards configuration F being preferred, where as S_F is preferable towards configuration A. While the normalized nodal sensitivities alone are fairly small, when combined they have a comparable magnitude to the other normalized sensitivities, and for the case of Table 4.14, a similar trend to that of S_F is present for the summed nodal sensitivities. The trends presented in Table 4.15 are weaker than those in Table 4.14, due to the lesser impact of the indenter on the movement of the material node. Furthermore, the trends of S_ϕ, S_F and the sum of all the nodal normalized sensitivities are reversed when compared to that presented in Table 4.14.

With the adaption to facilitate topology optimization and a more densely characterized indenter, additional consideration will be needed to assess the impact of increasing the number of the indenter geometry components on overshadowing the sensitivities of the material parameters. This can be overcome with use of the weightings, w_i. Allowing the indenter to be characterized by variable nodes, each with an x and y coordinates, will ensure the indenter has the ability to indicate an optimal shape and with an increasing number of nodal locations considered it is expected that more complex shapes can be considered.

4.6 Further extension to optimize across material types

As was shown in Section 4.3, the most logical use of the optimization of Q in the form presented is to determine the optimal testing configuration (B, D and F) for a given material (E, ν, ϕ and c). However, this does not accommodate a situation where an optimal test is desired to be used with a variety of material types. For example, this could be the desire to have a single *in situ* testing

device that can characterize a range of material types. If the material parameters are allowed to vary in the optimization, the result would be an optimal test with no practical meaning, as it is the optimal test for some previously unknown material type. In order to discover a material test which is more universally applicable across different material types, a simultaneous optimization of the testing configuration over a range of material types is needed. This is achieved by effectively combining the Q values of the different material type and minimizing their sum. This is presented mathematically as

$$Q = \frac{1}{mn} \sum_{j=1}^{m} \sum_{i=1}^{n} w_i \left[\left(\frac{\partial \alpha}{\partial \beta_{(i,j)}} \right) \left(\frac{\beta_{(i,j),avg}}{\alpha} \right) \right]^2 \tag{4.8}$$

where m is the number of material types considered and the resulting β term is a matrix of dimensions m x n.

By incorporating a number of material in types the optimization one must consider all different material types inputted equally and return a configuration which will have the best results across the materials. The resulting configuration will not necessarily present the optimal method for any given material assessed.

4.7 Concluding remarks

This chapter has detailed the process of the implementation of Q to finite element analysis using MATLAB and OptumG2, and ultimately KNITRO when optimization is implemented. A simple finite element model is presented using elastoplastic analysis with a Mohr-Coulomb model.

Numerical differentiation is used to determine the parameter sensitivities required for Q. Sensitivity plots show that while the sensitivity of E is smooth and convex, the others are non-convex and non-smooth, leading to a complex optimization. Single parameter implementation of a select few cases shows that, for the most accurate determination of these individual parameters, the wide shallow indenter is the optimal configuration. Furthermore, E is the optimal parameter to discover, followed by ϕ and then c. The variation of the measurement location showed that the same trends

are found in the selected configurations, with the wide and shallow indenter always performing the best, and the narrow and deep indenter always performing the worst.

To provide proof of concept of the implementation of Q, a simplified error analysis is implemented. Two configurations and two material types are selected to compare, for a total of four tests. A small error is applied to all the configuration parameters, to simulate real-world error. The resulting material parameter is determined, and the test with the lowest Q should also produce the lowest variation in material parameters. It is found that Q will predict the test which will present the highest probability of a lower error. This shows that in this application Q does what it is intended to do.

The assessment of Q to return the quality of a test for determining multiple material parameters leads to cross correlation. It is shown that with multiple measurements recorded, the correlation can be reduced significantly. An optimization is conducted to determine the optimal geometry for the fill-like material considered. The surface of this optimization space shows that there is a strong local minimum in the problem although the reconstruction of the inverse problem indicates that this test has a unique solution.

The metric Q can be expanded to simultaneously optimize the test for multiple material types, allowing more universally applicable tests to be specified. Furthermore, topology optimization can be implemented, by including the nodal coordinates' sensitivities in place of the sensitivities for parameters specifying indenter geometry. This allows the geometry of the indenter to vary beyond a rectangular indenter. A simple example assessing the shape of an indenter reveals that it is most desirable to use the indenter the blunt wedge, for the six configurations considered. Evidence suggests that there is a compromise between the indenter displacement and the surrounding material disturbance which leads to this optimization.

CHAPTER 5
MATERIAL STRENGTH DETERMINATION FROM TOW TESTS

Following the determination of a method for test quality comparison, through the metric Q, one can consider applying this methodology to *in situ* material parameter determination and more specifically *continuous* material parameter determination. Here continuous refers to material parameter determination over an area, compared to at one location. With the development of Q still in progress, the work contained in this chapter takes a step back to investigate the feasibility of retrieving material parameters from simple tests that are already happening in locations which knowledge about the material parameters is desirable. For locations such as construction sites or in the field of trafficality, ground-engaging equipment is present and already deforming the near-surface material.

Geotechnical material parameter testing has traditionally meant identifying the ground conditions at a finite number of locations with testing specific devices. This is usually sufficient for the intended applications as all of these values would be taken into consideration and a some average used for analysis. In almost all cases, it would be advantageous to have a continuous measurement of the ground conditions and, furthermore, preferable to require minimal effort to determine this measurement. The aim of this chapter is to assess the feasibility and effectiveness of tow tests as a novel method for measuring the *in situ* strength of beach sands (near surface), in particular as compared to existing methods for characterizing strength such as penetrometer testing. In this chapter, the data from a field work series is presented and analyzed. Multiple variations of the tow test are conducted and compared, effectively creating a pesudo-topology optimization to assess the optimal tow test.

All apparatus used for the tow tests (Figure 5.1) were designed and built using Northwestern's graduate student workshop over the summer of 2019, and the field work was conducted 4 - 10th of October 2019 at Duck Beach, NC, in association with the U.S. Army Corps of Engineers Field Research Facility (USACE-FRF) in Duck, NC and Virginia Tech (VT). The material testing, using

Figure 5.1: Trailer apparatus.

BlueDrop and SoilSaber devices, was conducted and analyzed with the assistance of Prof. Nina Stark and her Virginia Tech research team, with particular assistance from Ph.D. student Julie Paprocki.

Specific objectives which are addressed in this chapter include developing the methodology for providing a continuous rut profile and assessing the comparison of rut profile measurements to the material tests of the BlueDrop and SoilSaber. The chapter is arranged to provide an overview of the location and field work schedule in Section 5.1, followed by the construction of the testing apparatus in Section 5.2. The results of the testing is presented in Section 5.3. The rut reconstruction process is presented in Section 5.4, and analysis of measured rut depths in Section 5.5. A discussion on the implementation of Q to the determination of optimal continuous material tests is provided in Section 5.6. Finally, Appendix C presents details of the methodology relevant to this chapter.

5.1 Testing site and field work schedule

The USACE-FRF at Duck, NC, lies on the barrier island between Currituck Sound and the Atlantic Ocean. Gallagher *et al.* [122] highlight the random variability in the beach sediments as well as the impact each tidal cycle has on the deposition. This is significant as it shows how there is large variability across the beach.

The site location is pictured in Figure 5.2, where the subtle rolling of the beach can be seen by following the tracks that extend from the lower left of the figure. The topography of the beach, both with respect to the small rolling hills in the long-shore direction and the gradual slope in the cross-shore direction, are shown in Figures 5.3 and 5.4. The satellite image (Figure 5.3a) shows an overview of the area, with the USACE-FRF in the upper left and the stretch of the beach used for testing extending diagonally down the figure. Figure 5.3b shows the topology of the beach and is constructed from LiDAR data collected by researchers from USACE-FRF during the fieldwork. Both images are orientated with North pointing up the page. Figure 5.3b further shows the cross-shore gradient with a steep slope on the left coming down from the dunes, then a gradual downward sloping section along most of the width of the beach before again a steeper section closer to the waters edge. This general trend is also visible in Figure 5.2. Figure 5.4 transforms the results of Figure 5.3b and reduces the vertical range by removing the higher dune sections and lower sections closer to the water, to better focus on the topography of the beach section relevant to this testing. The gradual slope from the dunes to the water can be seen here but more importantly is the variable elevation in the long-shore direction which can be seen more clearly in the middle with the wave-like pattern of the colors. Closer to the waters edge there is an increasing in the magnitude of the elevation differences in the long-shore direction. This topography is significant as the rolling long-shore and gradual cross-shore causes changes in the deposition behavior, resulting in changes in material strength. The difference in the pattern of elevation variation for the dune and water sides of the beach is further investigated in Section 5.5.

In Figure 5.5 the impact of the variable material strength on the tow tests can be seen easily

Figure 5.2: Beach with rut produced by tow test, visible between wheel tracks left by vehicle.

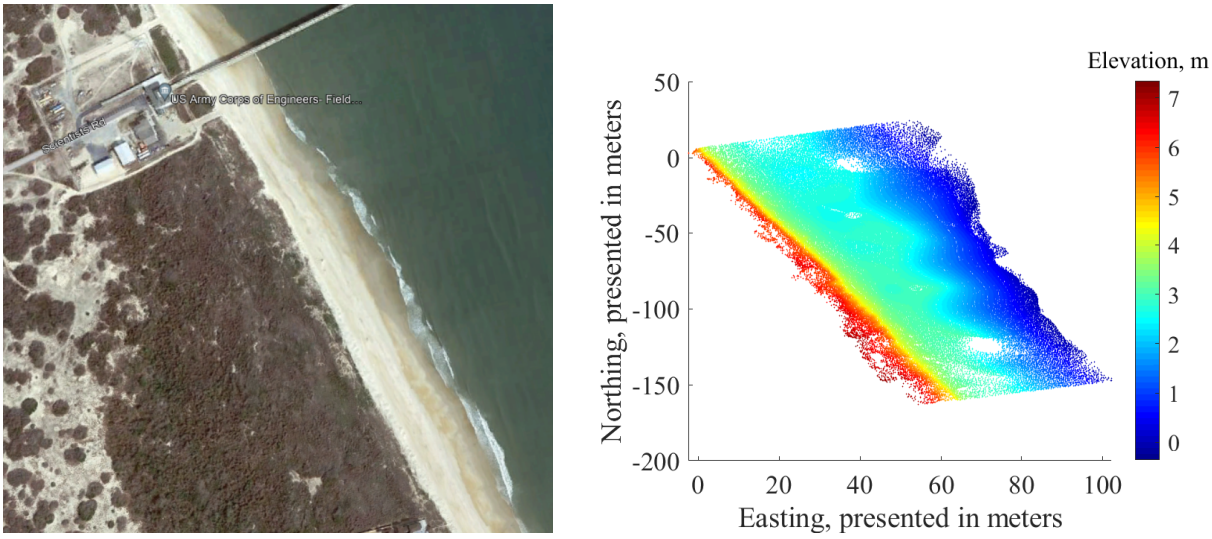

(a) (b)

Figure 5.3: Site location: (a) satellite image of the area; (b) LiDAR showing beach elevations.

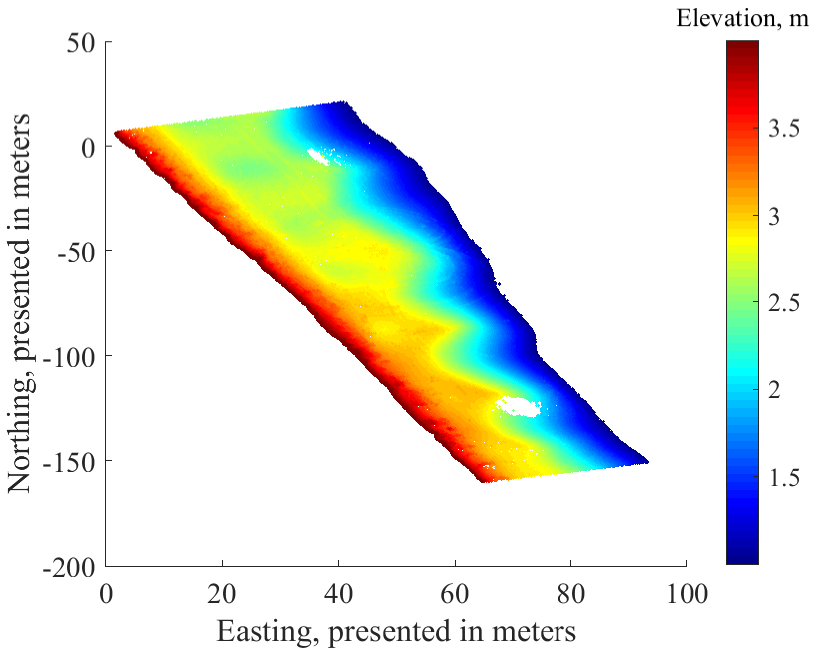

Figure 5.4: Highlighted range of LiDAR showing beach elevation.

by focusing on the rut extending from the middle bottom of the image up to the vehicle and more specifically focusing on the shadow that the left-hand berm casts. The shadow cast by the person (the author) in the photo marks a transition from a stronger material, indicated by a minimal rut, to a weaker material where there is a larger rut and shadow. The rut again returns to much shallower and less of a berm closer to the vehicle.

The overarching objective of the fieldwork is to map the length of the beach section of interest by recording ruts and comparing with results from more conventional testing at locations along the length of the ruts. The schedule of the field work to complete this objective is presented below. In this schedule there are three trailer attachments, (1) the wheel, (2) a wedge attachment with a tip angle of 30°, and (3) a wedge attachment with a tip angle of 45°. A rut is defined as one pass of the beach (approximately 350 m).

- ***Day 1:*** Set-up and apparatus modifications—no recorded data
- ***Day 2:*** 4 ruts, wheel, constant weight
- ***Day 3:*** 4 ruts, wedges (45° and 30°), no applied weight, BlueDrop and SoilSaber data for

Figure 5.5: Beach with indication to material strength.

comparison

- ***Day 4:*** 2 ruts, wheels, constant weight, SoilSaber data for comparison

On Day 1 the objective was to successfully assemble and operate the trailer used for the tow tests, without attaching to a vehicle but rather manually towing the trailer to ensure the trailer worked as intended. Then, on Day 1, the trailer was fitted to the towing vehicle with the wheel attachment installed, and initial rut data was collected. Data from Days 3 and 4, where there are comparisons to other material test methods are further analyzed and presented in the following sections. Note that the BlueDrop was only used on Day 3, due to availability.

5.2 Design and build of tow test apparatus

The testing apparatus is a one wheel trailer for which the wheel width can be varied. The wheel can be swapped out for a wedge of varying width and angle, effectively changing from a roll test to a drag test. The trailer with the wedge attachment and full width is shown in Figure 5.6. The main features which were designed for included, minimizing the transfer of vertical force from

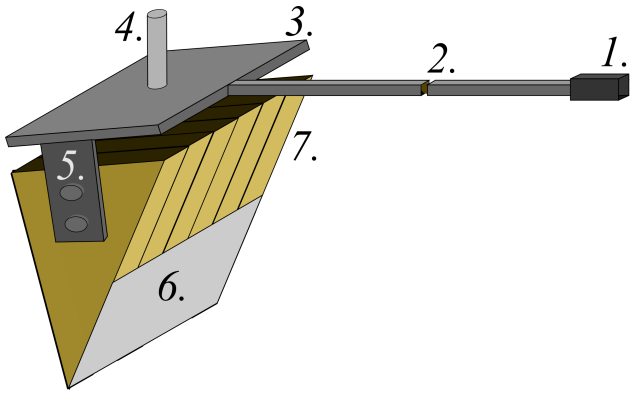

Figure 5.6: Features of attachment trailer, when fitted with wedge for drag testing.

the attachment (wheel or wedge) to the trailer attachment point and allowing for varying widths and applied force with a segmented attachment design and a variable weight system. Figure 5.6 illustrates the key trailer features for the case of the wedge attachment where location 1 is the hitch attachment point to the towing vehicle, location 2 is the hinge, designed to minimize the transfer of vertical force to the hitch, and location 3 is the rigid transfer plate. Furthermore, location 4 is the weight attachment system, with plate weights easily positioned on the small pole and a nut at the top used to secure them. Location 5 refers to the multiple axles, with two axles used to attach wedges. Finally, location 6 is the sheet metal protective guard installed to reduce wear on the wooden wedges, and location 7 refers to the segmented attachments which are combined to form the full width. The trailer was intentionally designed such that the attachment type, applied weight and attachment width could be changed, to facilitate a pseudo topology optimization. This is further detailed in Section 5.6.

The wheel was selected as an attachment for the trailer as it is the shape that provides the least resistance to towing. The wedge, in two different angles, were selected as these provided a slight variation of a similar shape and are significantly different to the wheel. All of these attachments (wheels and wedges) were constructed from a repurposed wooden counter top. Whilst metal attachments would have been more desirable for longevity and stiffness, the wood was freely available and easily shaped. The exactness of the attachment pieces was ensured by first drilling two holes in the board, to secure the attachment piece to the bench. These two attachment points

(a) (b)

Figure 5.7: Construction of attachment pieces: (a) wheel segment; (b) wedge segment.

are shown in the center of the pieces in both Figures 5.7a and 5.7b. These two holes have a known position in the board and from the point of the second hole the drill bit is programmed to router out the shape of the attachment. Special consideration was given to ensure that the roundness of the corners on the wedges was sufficient so as to not cause the corners to chip during construction but also as sharp as possible. This was determined through trial and error. Additionally, the wedge point in contact with the ground was protected through the use of sheet metal designed to reduce wear as well as prevent chipping of the wedge corners. Much of the remainder of the trailer was constructed from aluminium. Simple deflection calculations were made to determine a sufficiently thick transfer/top plate as well as the capacity of the hinge, which would be subjected to a significant axial load. The trailer was connected to the towing vehicle via the hitch point. Prior to construction the height of this point was not known. As it was lower than had been thought, this lead to the trailer leaning slightly forward during testing (Figure 5.1). The final implication of this was not significant to this work, as the work does not intend to provide a model for use in future work, but rather simple provide proof of concept of the methodology used.

The trailer is easily assembled/deconstructed so when required to be taken to the field it can be deconstructed and stowed in a suitcase. Upon arriving at the site in Duck, NC, the trailer was quickly reassembled. This ease of assembly also allows for an ease to change the attachment type. Further details, including some lessons learnt, are included in Appendix C. The system designed to carry the weight was not implemented for the field testing. This was due to the availability of block weights which effectively completed the task, as shown in Figure 5.1. Furthermore, weight was not needed to achieve sufficient penetration of the wedges. The weight of the trailer with the wheel attachment, including the lead weights, was 18.8 kg. The weight of the trailer for the wedges was 7.4 kg for the wedges. The weights presented here are adjusted to account for the attachment angle causing the trailer to lean forward, as can be seen in Figure 5.1, using a scale. The towing speed for testing was approximately 5-10 km/h.

5.3 BlueDrop and SoilSaber material testing and on-site observations

As has been the focus of much of this thesis, existing material testing is well researched and widely used, although it too has its downfalls. Most notably to this chapter, it is traditionally non-continuous and subjected to human error. Often it needs to be repeated multiple times at each location, leading to a very time-consuming method of material parameter determination. The tests conducted for comparison in this chapter include Blue Drop and SoilSaber tests. The BlueDrop is a torpedo like free fall penetration device which was designed for use underwater, characterizing the seabed. Although it is usually deployed off a boat, it can be used on land by lifting the device above the area to be tested and allowing the device to free-fall to the ground surface. A quasi-static bearing capacity can be computed from the resulting penetration using the method proposed by Stark *et al.* [99]. In this work the results from the BlueDrop are reported as penetration. The SoilSaber is a mini shear vane device that gives a digital measurement of shear resistance. This device has been shown to be suitable for a wide range of *in situ* materials, ranging from 0.5 - 500 kPa [98]. The main benefits of both devices is that they are simple to use and rapidly deployable.

The material testing was conducted on two separate days (Day 3 and 4) with the approximate

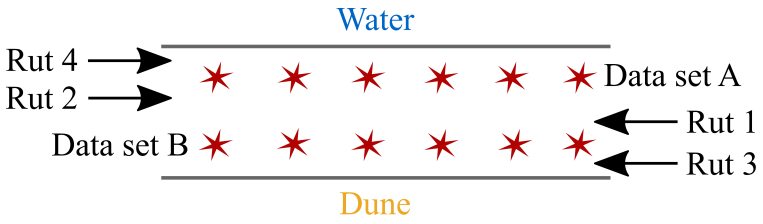

Figure 5.8: Location of testing - Day 3.

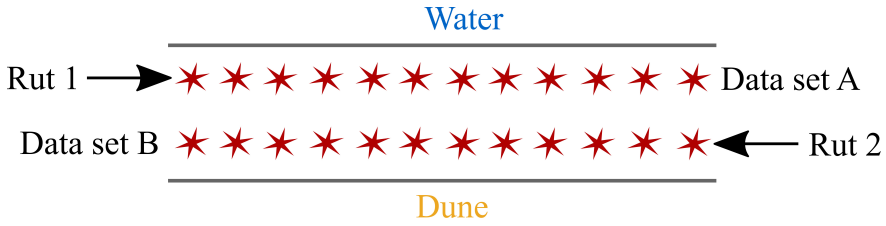

Figure 5.9: Location of testing - Day 4.

locations for testing on each of these days presented in Figures 5.8 and 5.9, as red stars, for each respective day.

The testing locations were selected as they encompassed most of the length of the path of the ruts and accounted for the variable conditions from the dune down to the water. On Day 3, BlueDrop and SoilSaber data was recorded, and on Day 4, only SoilSaber measurements were taken. Material testing was conducted after the ruts had been formed and is numbered such that location 1 commences at the smallest distance and the location numbers increase as the distance increases. All the material was tested *in situ* and could be considered somewhat disturbed, as the location was a public beach with people walking, life guards driving, and other researchers moving about. An effort was made to find the least disturbed and most natural locations for both driving the ruts and conducting the material tests. Furthermore, all testing was limited to one set of passes of the beach per day, due to the tests needing to be conducted at low tide and insufficient less disturbed locations being available following one set of passes.

The data for the tests conducted on Day 3 is presented in Figure 5.10. Figure 5.10 reports all the material testing results from Day 3 of the field work. Note that the y-axis of Figure 5.10b is reversed so as to match the trends of the BlueDrop data in Figure 5.10a. As a higher penetration for both the BlueDrop and rut depth correspond to a weaker soil where as a weaker soil is identified

by a lower shear resistance value. Furthermore, the plotted lines in Figure 5.10 are constructed as the average of three measurements taken at each location. The distance displayed on the x-axis corresponds to an approximate testing location with zero being the approximate start location of the ruts. The trends indicated by the tests in Figure 5.10 are somewhat sparse, although they do align, with both of these tests showing a weaker material to begin with and a stronger, more consistent (yet still fluctuating) material beyond 170 m, with the exception of Track A in the SoilSaber data beyond 240 m, where the material again indicates a weakening.

To further illustrate the strength of the *in situ* material, Figure 5.11 gives a visual of one of Rut 2, with an image at each of the tested locations. Observations from each of the images can then be compared to the material test data. Relative to the six images shown Figure 5.11a presents the largest rut, followed by a similar rut in Figure 5.11b. The locations in Figures 5.11c and 5.11e present the smallest ruts, and Figures 5.11d and 5.11f present ruts somewhere in the middle. These observations can be made by assessing both the shadow the left-hand berm casts as well as the width of the berm visible in the image. The results are consistent with the material testing in that the initial portion of the rut is much deeper than the final portion, indicating that the initial portion of the rut is through a weaker material.

The data for the tests conducted on Day 4 is collected in Figure 5.12. In Figure 5.12, two distinct trends can be seen for Tracks A and B. Track B is generally weak with slightly stronger sections on either ends, and Track A displays a fairly significant oscillation between strong and weak areas. This data can be compared to the rut visuals in Figure 5.13, where an image is presented for Rut 2 at each of the approximate testing locations and is compared to the Track B data set in Figure 5.12. The comparison can be seen by assessing the two ends (Figures 5.13a and 5.13l), which present a slightly shallower rut. Much of the middle is generally the same with a larger rut (Figures 5.13b to 5.13k).

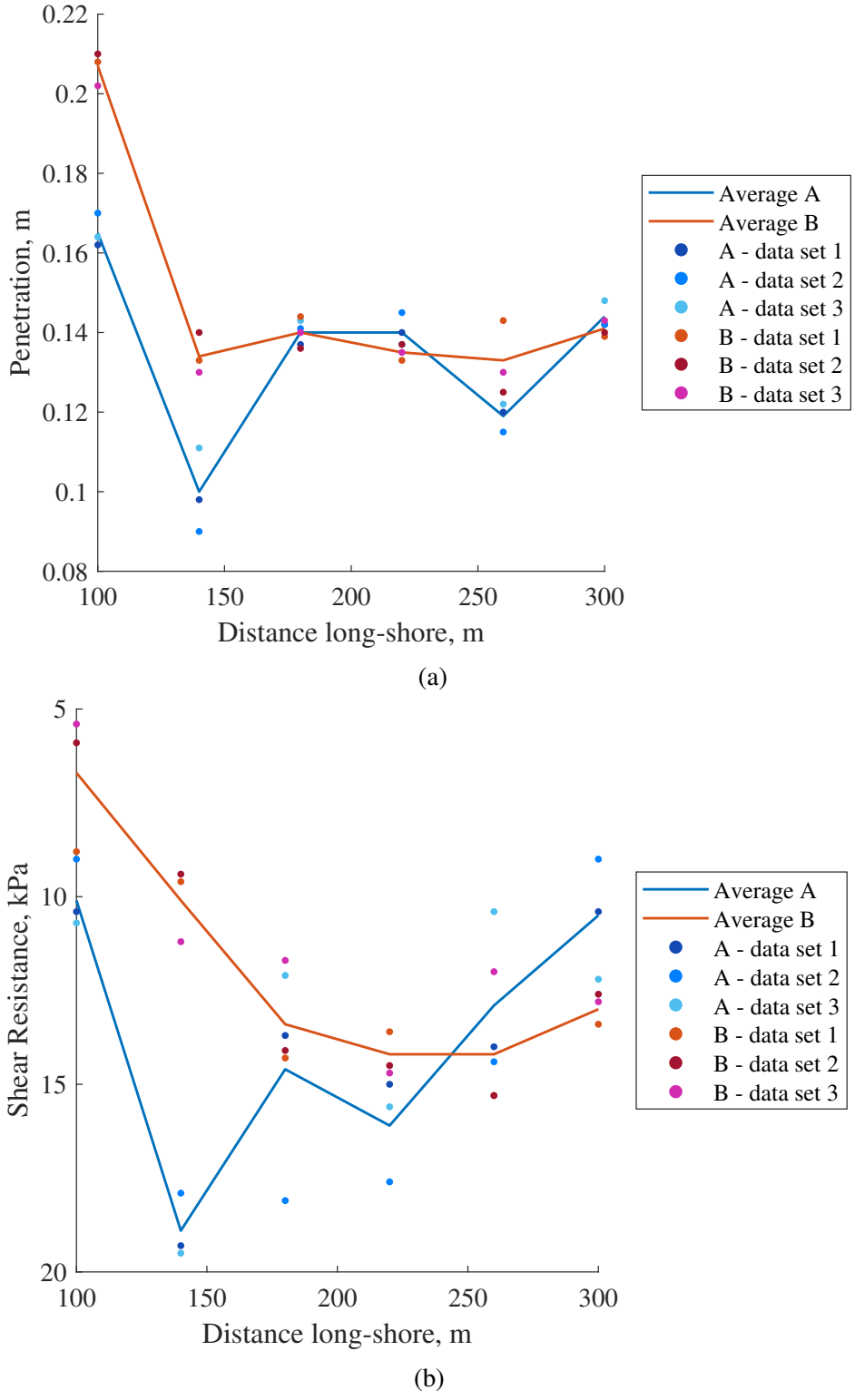

Figure 5.10: Day 3 testing: (a) BlueDrop; (b) SoilSaber.

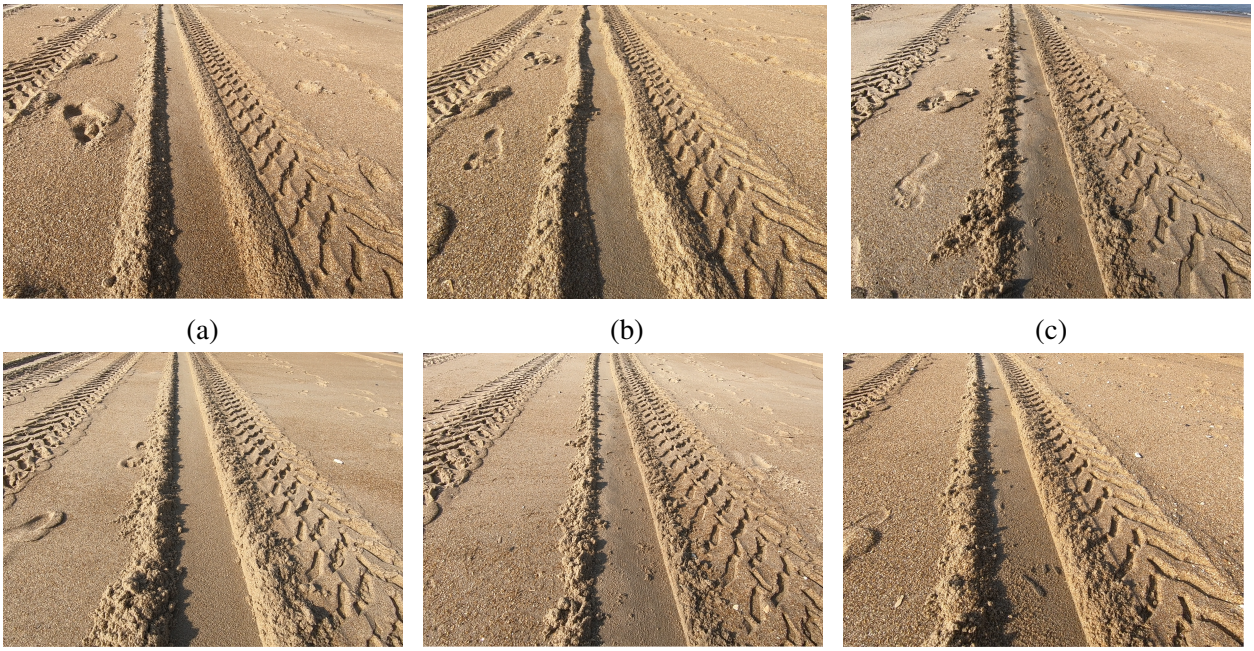

Figure 5.11: Rut Visuals - Day 3 Rut 2. Subfigures (a) through (k) correspond to locations 1 to 6.

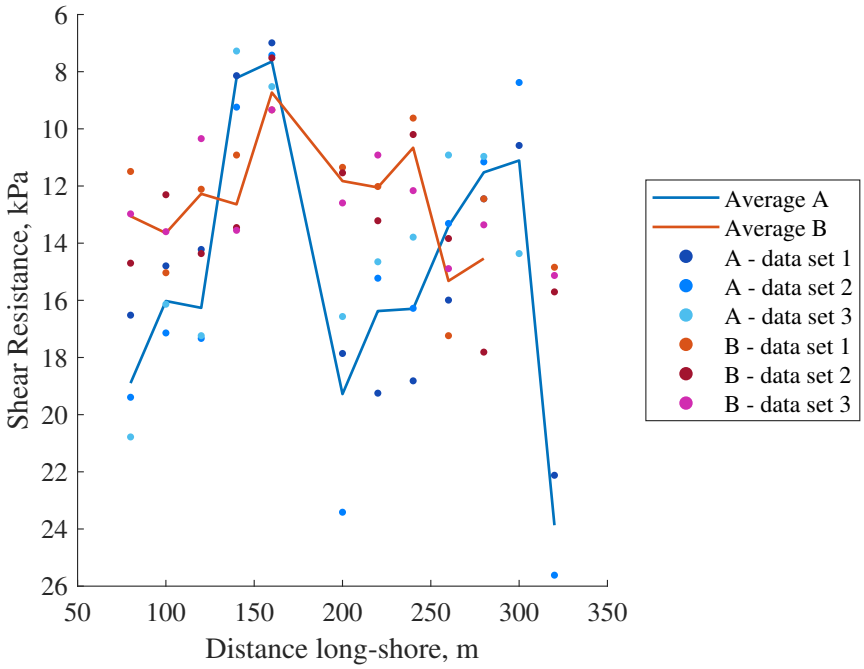

Figure 5.12: Day 4 testing: SoilSaber.

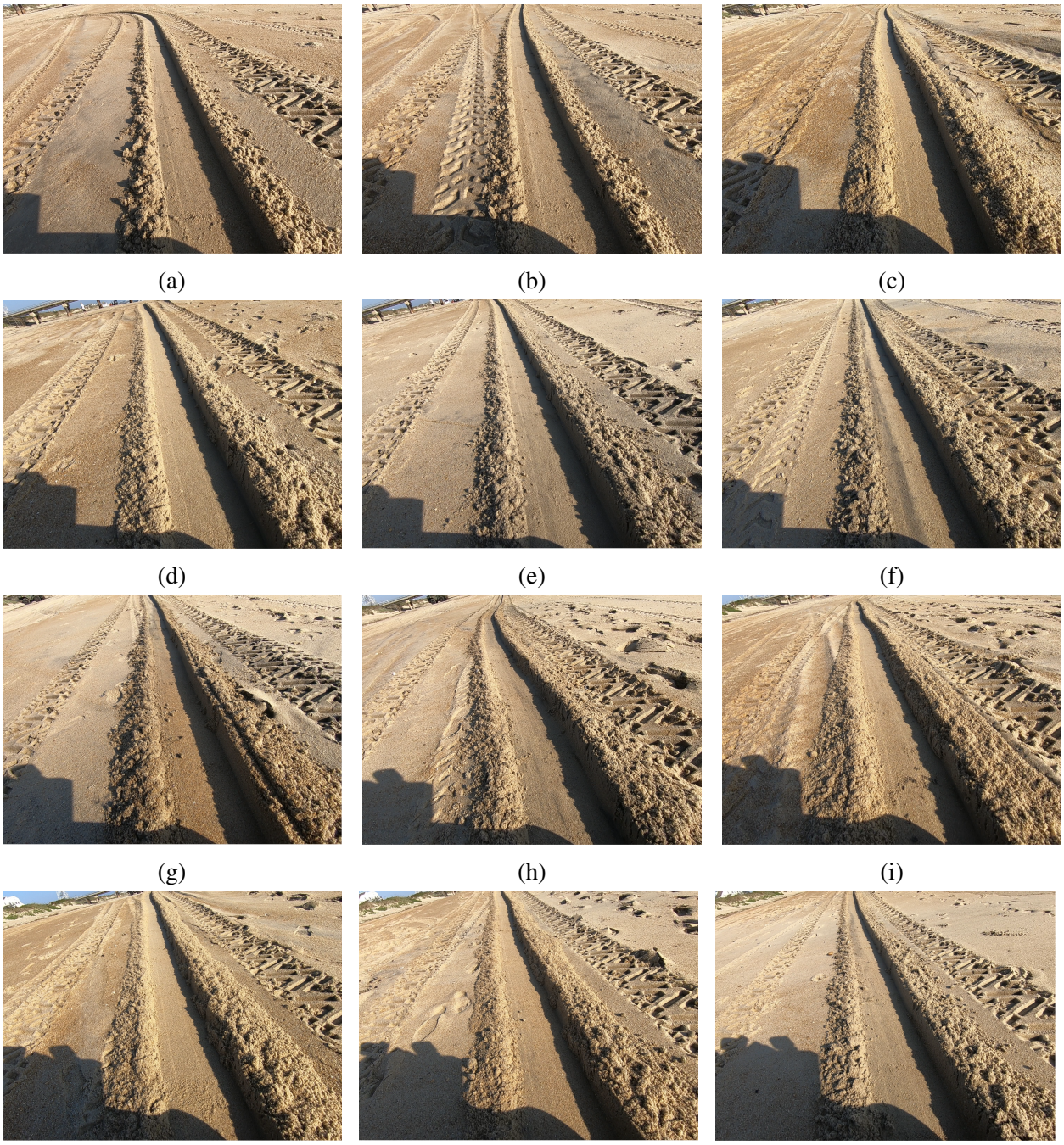

(a) (b) (c)

(d) (e) (f)

(g) (h) (i)

(j) (k) (l)

Figure 5.13: Rut Visuals - Day 4 Rut 2. Subfigures (a) through (l) correspond to locations 1 to 12.

5.4 Rut reconstructions from tow tests

The main goal of this field work excursion was to document, with video, the ruts created by towing objects (a wheel and wedges) through the sand, and from these videos recreate 3D models from which data can be easily extracted. The methodology from documenting the on site data to the production of the final results is detailed in Appendix C. The essential aspects and results from the analysis are presented in the subsections below.

5.4.1 3-D reconstruction of rut

Two GoPro cameras were mounted to the trailer and positioned so they recorded the rut from different angles. This footage was then imported to Pix4Dmapper where frames were extracted at a rate of 5 fps (frames per second). Pix4Dmapper is the photogrammetry software used to process the images. The software allows for the input of the camera details (lens measurements/focus point etc.) and where the reconstruction does not match the inputted camera details, the software optimizes the values and provides recommendations of new values for better results. Following initial reconstructions completed by Pix4Dmapper, results are further manipulated by manually tying points in different frames. This process is further detailed in Appendix C. Adding manual tie points consists of selecting a known point in multiple frames and specifying this as the same point. This process allows the software to better adjust to the conditions presented in the project and optimize the reconstruction. Once the reconstruction in Pix4Dmapper is deemed sufficient by the user, the point cloud is generated. This point cloud often encompasses the vast area that is filmed. In this case, it includes the pier, dunes and water. These areas are removed before exporting the final point cloud. An example of this reconstruction prior to the removal of unwanted areas is shown in Figure 5.14 for a rut driven on Day 4. Here the green line is the images used the in reconstruction (corresponding to the location of the rut). On the left are the dunes and some sky, and on the right is the ocean. At the very top of the image the straight line that can be seen is a section the pier. The two locations where there is less sand presenting close to the image line

are locations where the photogrammetry struggled to produce a reconstruction, and more manual tie points were required to assist the convergence. The location of all the manual tie points used are shown by the added green pins in the area along the rut. Figure 5.14b shows the rut after the removal of the the unwanted features, and Figure 5.14c zooms in on just one section of Figure 5.14b where the rut left by the trailer can be easily identified in the center. In Figure 5.14c the tire tread of the vehicle towing the trailer is visible on either side of the rut.

5.4.2 Analysis of 3-D reconstruction

Upon completion of the rut reconstruction in Pix4Dmapper, the 3-D model is in the form of a point cloud (.las). This is then analysed in MATLAB. Details of the analysis process in MATLAB can be found in Appendix C. The point cloud is effectively a file containing the coordinates of millions of points, which together detail the surface that is the reconstructed rut. From this list of points, slices are taken perpendicular to the direction of travel of the rut, and various geometries of the rut are computed.

The first step in the MATLAB analysis is to reorient the rut so that the long direction, distance long-shore, is in the y-direction. Then slices are taken, which are bounded by a finite width in the long-shore direction. A plane is fitted to these slices using optimization, to create a local coordinate system. The result is presented in Figure 5.15. The x-plane is considered an approximation of the beach surface and used to measure the rut features. The berm height is taken as the maximum positive distance from the plane, and the rut depth is the maximum negative distance from the plane. Measures are taken to reduce the presence of errors in these measurements, such as ensuring the identified points are not outliers and within reasonable distances of each other. However, there are still some imperfections in the rut reconstruction, which are removed with filtering and averaging. A sample of the raw results are presented in Appendix C. The results shown in this chapter are filtered and averaged.

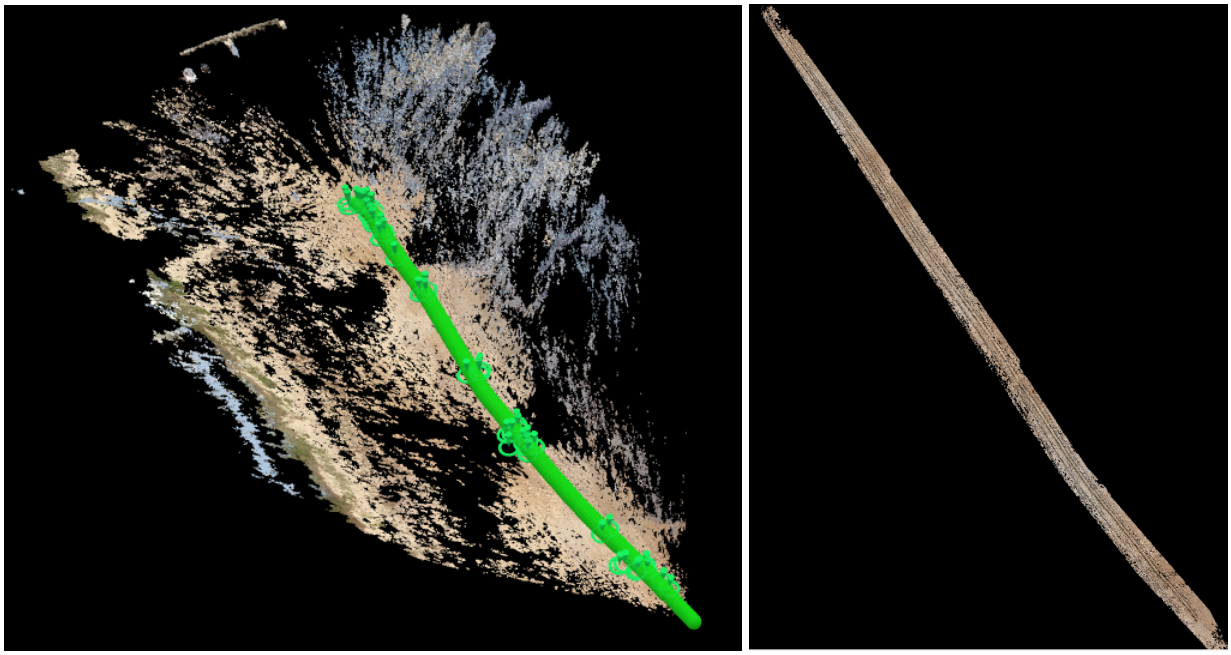

(a) (b)

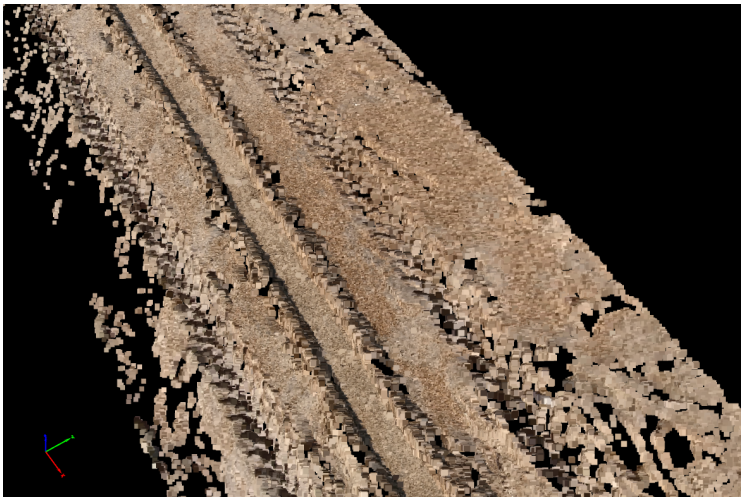

(c)

Figure 5.14: Point clouds from rut reconstruction using Pix4Dmapper: (a) unedited; (b) trimmed; (c) highlighted section.

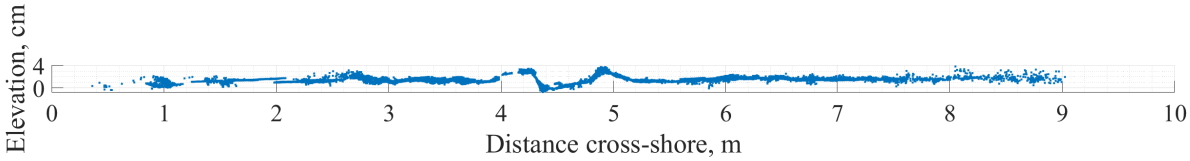

Figure 5.15: Slice of rut sample.

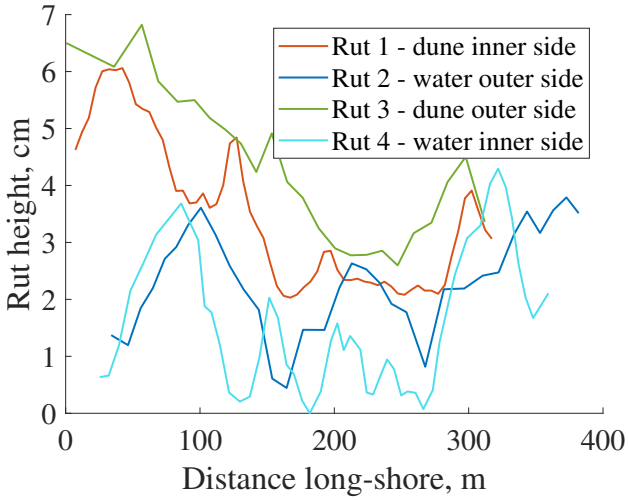

Figure 5.16: Rut reconstructions from Day 3.

5.5 Reconstructed ruts and test comparison

The reconstructed ruts are presented in this section along with a comparison to the the BlueDrop and SoilSaber test data. The ruts which were reconstructed and analyzed correspond to those indicated in Figure 5.8 for Day 3 and Figure 5.9 for Day 4. In all cases, the data presented here is orientated such that the origin is at the north end of the test site (closest to the pier), and the distance extends south, away from the pier.

The four ruts from Day 3 are presented in Figure 5.16. The height reported refers to the total rut height, from the top of the berm to the bottom of the rut. It can be seen that the water side ruts generally present smaller heights, while the dune side reach larger heights. This is consistent with the field observation that the material generally became more consistently soft closer to the dunes. Furthermore, there was more variation in the elevation closer to the water which, in the field, appeared to show a oscillating strength profile. This is present in the rut profiles of the water side ruts, which vary in height from approximately 0 to 4 cm.

Each of the ruts presented in 5.16 are individually presented in 5.17 alongside a comparison to the test data which was taken closest to the ruts. Figure 5.17 presentes the rut heights in a normalized form, as well as normalized BlueDrop and SoilSaber data. The BlueDrop and rut data

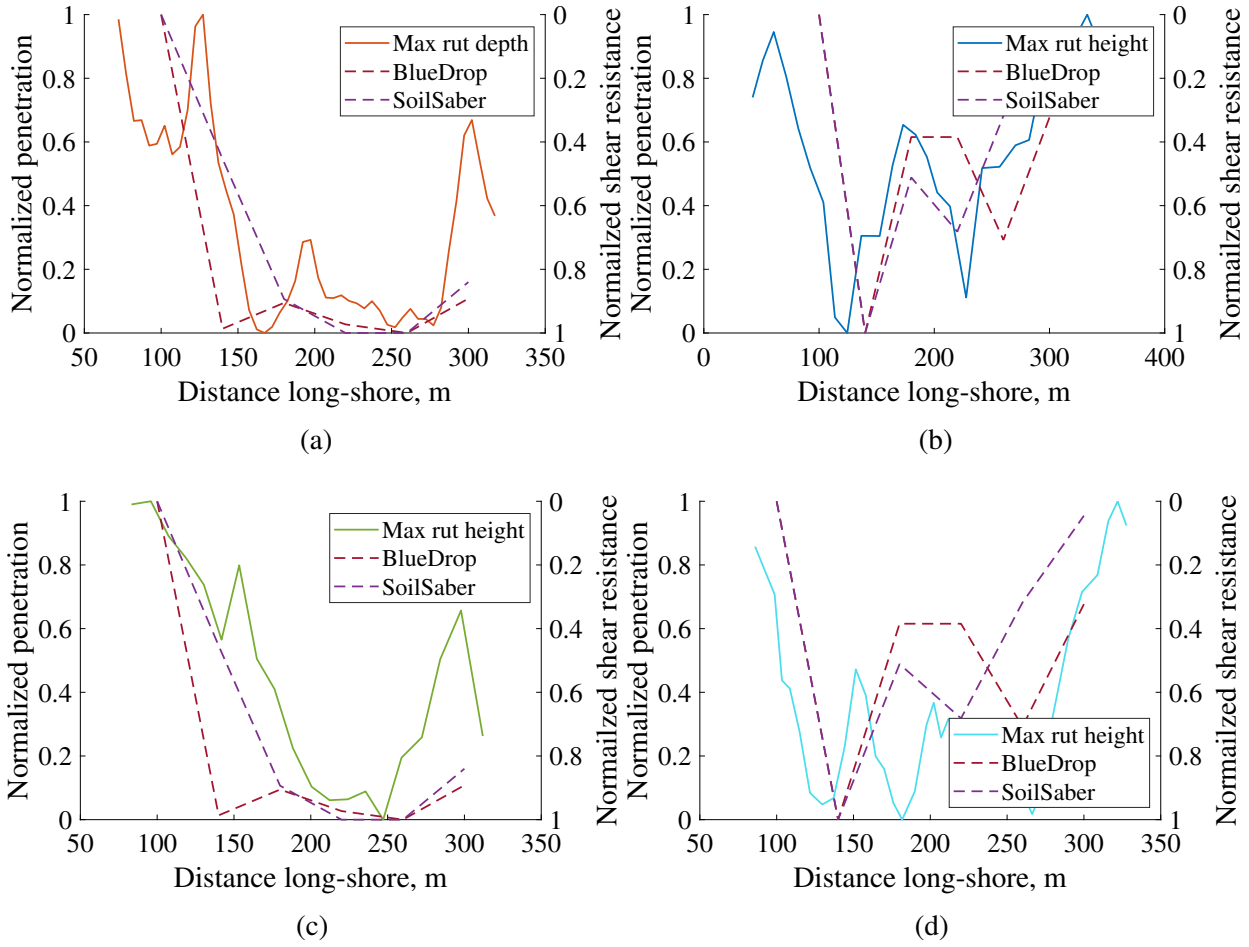

Figure 5.17: Day 3 rut comparisons, for rut: (a) 1; (b) 2; (c) 3; (d) 4.

are plotted on the left-hand axes while the SoilSaber is plotted on the right-hand axes, and the direction is reversed in order to match the meaning of the left-hand axes. All of the comparisons present similarities to the trends of the test data, with a general trend upwards at either end of the plots. Furthermore, there is a low flat section in Ruts 1 and 3, and a upwards hump in the middle of Ruts 2 and 4.

As with Day 3, the reconstructions from Day 4 are firstly presented together in Figure 5.18 and compared to the test data in Figure 5.19. In Figure 5.18, it can be seen that the water side rut (Rut 1) presents the expected oscillating rut height, while the dune side rut has a less consistent profile. Furthermore, there is a very good comparison with the test data for both of these ruts. The better comparison of test data and rut reconstructions presented for Day 4, in comparison to Day

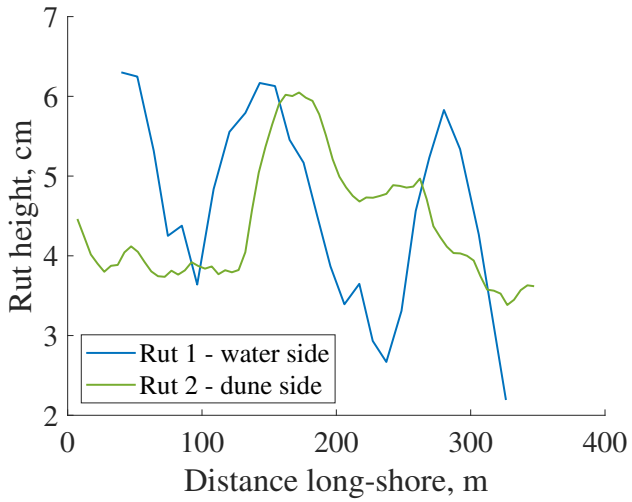

Figure 5.18: Rut reconstructions from Day 4.

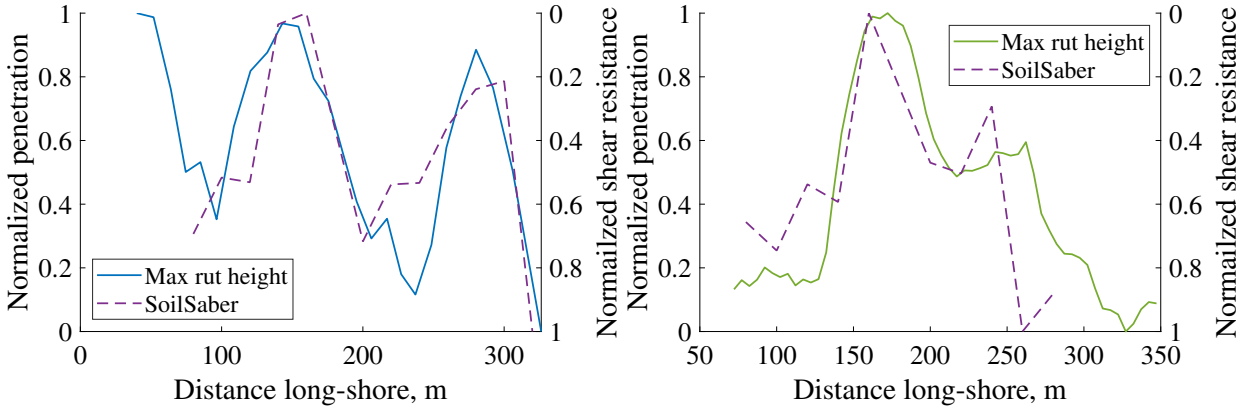

Figure 5.19: Day 4 rut comparisons, for rut: (a) 1; (b) 2.

3, is likely due to the increase in testing locations as well as the testing locations all being directly adjacent to the rut on Day 4.

An additional comparison is made for the rut reconstructions from Day 3, to plot the data from Figure 5.16 as a contour plot. This is presented in Figure 5.20. This figure is significant as it presents a full reconstruction of the beach. The cross-shore distance is measured from the water (0 m) to the dunes (15 m), and as with previous data, the north end is at the long-shore distance of 0 m. The same trends identified in Figure 5.16 are shown here with the added ability to assess the cross-shore variation, with the most significant change at about the 30 m mark and a generally

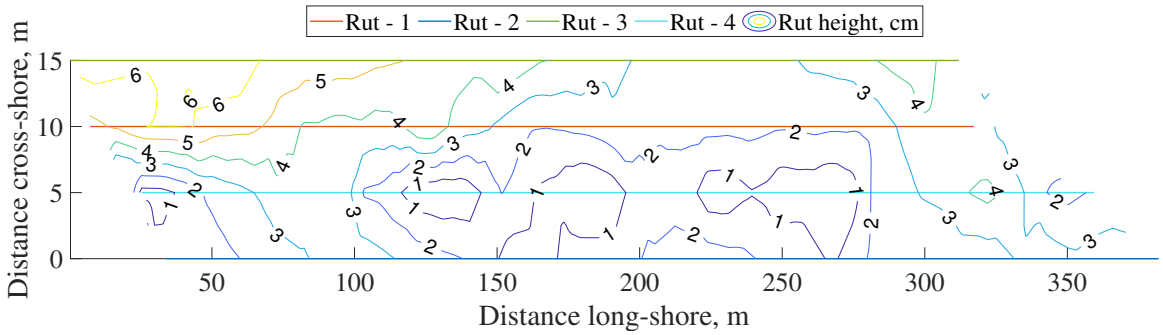

Figure 5.20: Reconstruction of whole beach - Day 3.

uniform section presented at about 225 m. This plot is a reconstruction from only four lines (as shown in the overlaid lines of Figure 5.20) and significant interpolation occurs between the lines. With a denser alignment of the rut height reconstructions, it could be expected that this contour plot could be transformed into a strength profile, with areas of higher strength having a lower rut height and softer material having a higher rut height.

It should be noted that the alignment of the distance long-shore for the various measurements are not exact. The relative locations are determined by identifying key features in the videos filmed, which are then identified in the reconstructions, and finally transformed to a location in the point cloud. It is expected that the lateral alignment could vary by 5-10 m. In future work this could be rectified by placing objects of known location in the space of the reconstructed area.

5.6 Discussion of the application of the quantitative metric to ground-engaging equipment

The work presented so far in this chapter focuses on the ability to infer material strength from deformations induced by ground-engaging equipment. The overarching objective of this track is to determine optimal methods of continuous near-surface characterization. To achieve this, the quantitative metric proposed in Chapter 2 could be implemented in a theoretical analysis inclusive of all movements expected of the ground-engaging equipment. A full theoretical implementation would require modeling capabilities to cover the ground-engaging activities. Even a simple comparison of the attachments used in the fieldwork presented in this chapter would require analytical

or numerical models which can accurately model the movements of the wheel and wedges being dragged through the sand.

The setup of the quantitative metric in this problem would have similarities to that presented in Chapter 4. The sensitivity of the geometric and material parameters, β_i, would be assessed against the measurements, α, such as rut dimensions. Non-material parameters for consideration in β_i and optimization in the analysis could include the geometry of the attachment, applied weight, driving speed, and any movements of the attachment, such as allowing the wheel to rotate.

There is still a conceptual jump between the assessment of a continuous surface characterisation and the optimization of a material test method for ground-engaging equipment. In this chapter three configurations were assessed, a wheel and two wedges. The analysis showed comparable results for all these tests, however, the designed trailer can accommodate other variations such as varying weight, attachment width, and more attachment types. With these variations an experimental campaign can be launched to investigate the optimal configuration in more depth. Furthermore, with the development of generalized numerical models which are inclusive of all movements expected of the ground-engaging equipment, an optimization of Q can be made. The result is an optimal process for material parameter determination.

5.7 Concluding remarks

The work presented here is the first iteration of what has the potential to be a significant development for continuous material parameter determination of the near-surface. A trailer was designed and built with the intention of providing proof of concept that simple interactions of existing equipment can be used to infer material strength. This trailer is towed on the beach to create a series of ruts, then each of these ruts are used to reconstruct a near-surface strength profile. Material test data is collected in the form of BlueDrop and SoilSaber testing and video of driven ruts. The field work contained in this thesis took place at Duck Beach, NC, in association with the USACE-FRF and Virginia Tech.

BlueDrop and SoilSaber testing was conducted on two separate days of the fieldwork. The

results of the BlueDrop and SoilSaber testing are further compared to images at each of the testing locations (extracted from the video recordings of the ruts). Good correlation is shown, with visibly shallower ruts corresponding to higher strength material in the BlueDrop and SoilSaber tests, and deeper ruts to lower strength material in the tests.

The process of reconstructing the ruts uses photogrammetry software and analyzes the resulting point cloud in MATLAB. Initial difficulties were faced in the reconstruction due to some of the methods used in the filming of the ruts (further discussed in Appendix C). The final result presented six reconstructions over two days of testing, and from this a continuous measure of rut height along the rut is determined. In all cases a reasonable correlation is made between the BlueDrop and SoilSaber tests and the rut heights. Higher strength areas identified by the BlueDrop and SoilSaber tests correspond to lower rut heights in the reconstruction. The beach near-surface material is found to be generally weaker (creating larger ruts) closer to the dunes, and both stronger and more variable closer to the water. Ruts closer to the water indicate an oscillating strength profile.

The collected data is insufficient to distinguish between different wedges and the wheel, and BlueDrop and SoilSaber testing locations were too far apart to provide a more definitive assessment of the quality of the continuous material test method. However, in order to achieve the same rut heights, the weight of the trailer with the wheel attachment is more than double that of the trailer with each of the wedge attachments.

Finally, a discussion is provided to make the conceptual link between the work presented in this chapter and all previous chapters. The implementation of the quantitative metric developed in Chapter 2 requires a model which can simulate the test. With the development of models capable of simulating the tests conducted in the field, the quantitative metric developed in Chapter 2 could be used to compare continuous near-surface material profiles and eventually optimize methods of material parameter determination with existing ground-engaging equipment.

CHAPTER 6
CONCLUSIONS AND FUTURE WORK

The work contained in this thesis forms the initial stages of a larger objective to create a methodology to design optimal soil tests. Chapter 2 investigates desirable features of inverse problems and from this, develops a quantitative metric to discriminate between tests. This metric is implemented to simple tests with analytical solutions in Chapter 3. The simplicity of these tests allows a proof of concept for the ability to compare tests. Chapter 4 makes a significant step towards the larger objective by implementing the quantitative metric to finite element analysis and completing an optimization of the geometry of an indenter. Finally, Chapter 5 details a parallel track investigating a continuous material test method, with the intention of incorporating the metric from Chapter 2 in future work.

6.1 Track I: Development of methodology to design optimal soil tests

The proposition is made that *the optimal test is the one which can recover the material parameters closest to the true material parameters given potential errors in non-material parameters*. From this, the quantitative metric, Q, is derived. This quantitative metric is carefully constructed and makes use of a combination of minimization and maximization in a minimization optimization of the sensitivity of all parameters within a forward model to consider all components of a test simultaneously. The use of sensitivity analysis in this way is unique to this thesis and allows for a methodology to be developed which aims to reinvent the design of optimal soil tests. An optimal test can be discovered by minimizing the quantitative metric within a given set of constraints. The quantitative metric is versatile and can be easily reconfigured to a different problem by varying the combinations of minimization and maximization, incorporating weightings to the parameter sensitivities, and modifying constraints placed on the optimization.

The first implementation of the quantitative metric is presented for the case of a spring exten-

sion test. By using the quantitative metric, conclusions can be drawn as to the selection of the test and ideal testing configuration. The choice to run a force-controlled or displacement-controlled test is a direct comparison of the average force-to-displacement ratio, F_{avg}/δ_{avg}, and the spring constant. A similar relationship is found for the comparison of force control and displacement control in uniaxial compression and three-point bending tests. A comparison between all the analytical tests considered presents that uniaxial compression and three-point bending are both comparable as the optimal tests. Proof of concept is provided for the ability to make the comparisons, by completing an error analysis. This shows that, with an increasing Q, there is an increasing probability that computed material parameters will be further from their true values when the non-material parameters are subjected to error.

The final aim of this track is to implement the quantitative metric to finite element analysis. This is completed by using MATLAB to run a KNITRO optimization solver and using OPTUM G2 as the forward model. A rectangular indenter is modeled with three different material types and a Mohr-Coulomb elastoplastic analysis. Consideration is given to the process of implementing the metric in finite element analysis, and it is shown that the optimization of the indenter geometry is highly non-linear. The non-linearity is caused by the combination of multiple non-linear parameter sensitivity plots and results in minima in varying locations across the optimization space. A simplified error analysis, similar to that previously mentioned, is performed for a selection of configurations. As with previous results, the analysis shows that error applied to non-material parameters produces material parameters that are further from their true values for a configuration with a larger Q value. An optimization of the indenter geometry is performed, indicating that the optimal geometry to use in a test to determine ϕ and c is a very wide and shallow indenter. An additional step is taken to implement a version of Q which can accommodate a more generalized characterization of the indenter, in this case by the nodal coordinates rather than dimensions. A select few cases of indenters with different shapes are investigated, indicating that there is an optimal case which is not at the bounds of the cases considered.

The implementation of Q to all situations presented in this thesis shows that for each of the im-

plementation types, analytical and numerical, all tests are reasonably similar. Whilst Q is presented in a normalized form, caution should be used to compare vastly varying tests, such as comparing Q from analytical and numerical models. Ideally, Q would be used in an optimization where the manipulation of the test is a function of the optimization, and this allows the comparison of significantly different tests.

The future work in this track will continue towards implementing the quantitative metric to more complex problems, aiming to solve for optimal soil tests. Added complexities to the implementation include unlimited geometric topology optimization, which would allow for the applied action to be optimized. Examples of possibilities of the applied action include forces, moments, prescribed displacements, and volumetric changes to the test device. This process is demonstrably very computationally intensive.

Furthermore, as is shown in Appendix A, there are other possibilities for qualitative metrics. Future work will aim to implement a metric which can assess the ability of a test to converge to a solution. This addition will make the process of designing a optimal tests more accessible when a robust optimization solver is not available. Additionally, a recommended expansion to the quantitative metric proposed in this work is to include parameter correlations. Designing tests with lower parameter correlations will result in fewer non-unique solutions and easier optimizations.

Additional testing using implemented error to provide proof of concept to the implementation can continue similarly to that completed in Chapter 3, although, it should be noted that this error analysis will be extremely time expensive. Alternatively, proof of concept could be provided through an experimental campaign. Tests with varying ratings classified by the quantitative metric could be completed, and the computed material parameters could be compared.

Finally, modifications can be made to the optimization process in terms of the parameters held constant, minimization and maximization terms, and weightings. This thesis considers the process of optimizing configurations for a given material, although, the quantitative metric can also be turned around to set the configuration as a constant and optimize the best material parameters to be tested with that configuration. It is expected that with the completion of this future work, the

quantitative metric will be capable of designing an optimal soil test for any conditions that the user desires to add.

6.2 Track II: Continuous material testing

The work of Track II is contained entirely in Chapter 5. The aim of this section is to experimentally investigate a continuous material test method, essentially embarking on an experimental campaign in place of a numerical topology optimization. The focus is mechanical parameter determination of near-surface soil and is presented through an experimental campaign of a towed wheel and wedge. The motivation of this aim comes from the idea that in locations that material parameter determination is desired there is often already ground-engaging equipment present, raising the following question: how can one infer material strength from these existing movements?

The continuous test method considered involves a trailer with wheel and wedge attachments towed along a beach. Photogrammetry software is used with videos of the ruts to reconstruct rut profiles, which data is extracted from. The reconstructed model of the rut left by the trailer is then able to provide an indication of the near surface soil strength in the form of rut height.

The rut height reconstructions are compared to two different *in situ* tests, the BlueDrop and SoilSaber testing devices. In all cases, a good correlation is shown, although, due to the limited data locations for the BlueDrop and SoilSaber tests, a detailed comparison cannot be made. The reconstructions are also compared to the themselves, with all cases presenting a weaker surface closer to the dunes and a less uniform and oscillating strength profile closer to the water's edge. This is consistent with the observations made on site.

This work provides proof of concept that simple manipulations of ground-engaging equipment can be used to infer material strength. There is significant potential for future work, in taking this proof of concept to a more robust proposal and practical implementation. Future work will consist of additional field testing, modeling of the continuous rut process, and finally an optimization scheme similar to that presented in Track I. The final result would be the methodology to design optimal continuous field tests for determining the material parameters.

Additional field testing should be conducted, and it is recommended that LiDAR replace the video and photogrammetry process. Small LiDAR systems can be purchased for a similar cost to the video setup and will remove the need for reconstructing the ruts. Furthermore, the errors in reconstruction are expected to be greater than any errors in the LiDAR data, so this change will have no negative impact. Future field testing campaigns should aim to test on less disturbed ground and collect a higher density of data in the sampled area. This could be completed by towing dual- or triple-wheel trailers. The higher density will allow for comparisons between the types of attachments and more certainty in the total beach reconstruction. Additionally, more attachment types, and variable widths and weights should be used to achieve a better pesudo-topology optimization.

Significant numerical analysis is needed, with the development of a model necessary for the computation of Q. The numerical implementation should aim to take a select few cases and compare their quantitative metric values with the performance through a numerical error analysis. Then, ideally a numerical model will be implemented, which can be automatically converted between various geometries and tests, allowing for the optimization to determine the preferred ground-engaging motion.

Finally, in linking this track to the overarching objective presented of thesis, it will be possible with the completion of this future work to design optimal continuous material tests for characterizing large areas of near-surface material.

REFERENCES

[1] Ou, C. Y. & Tang, Y. G. (1994). Soil parameter determination for deep excavation analysis by optimization. *Journal of the Chinese Institute of Engineers*, *17*(5), 671–688. https://doi.org/https://doi.org/10.1080/02533839.1994.9677634

[2] Hashash, Y. M. & Whittle, A. J. (1996). Ground movement prediction for deep excavations in soft clay. *Journal of Geotechnical Engineering*, *122*(6), 474–486. https://doi.org/https://doi.org/10.1061/(ASCE)0733-9410(1996)122:6(474)

[3] Cavello, M. & Finno, R. J. (2004). Selecting parameters to optimize in model calibration by inverse analysis. *Computers and Geotechnics*, *31*(5), 410–424. https://doi.org/https://doi.org/10.1016/j.compgeo.2004.03.004

[4] Hashash, Y. M., Levasseur, S., Osouli, A., Finno, R. & Malecot, Y. (2010). Comparison of two inverse analysis techniques for learning deep excavation response. *Computers and Geotechnics*, *37*(3), 323–333. https://doi.org/https://doi.org/10.1016/j.compgeo.2009.11.005

[5] Rechea, C., Levasseur, S. & Finno, R. (2008). Inverse analysis techniques for parameter identification in simulation of excavation support systems. *Computers and Geotechnics*, *35*(3), 331–345. https://doi.org/https://doi.org/10.1016/j.compgeo.2007.08.008

[6] Zhao, B., Zhang, L., Jeng, D., Wang, J. & Chen, J. (2015). Inverse analysis of deep excavation using differential evolution algorithm. *International Journal for Numerical and Analytical Methods in Geomechanics*, *39*(2), 115–134. https://doi.org/https://doi.org/10.1002/nag.2287

[7] MATLAB. (2019). *R2019b* (Version 9.7.0.1190202). https://www.mathworks.com/products/matlab

[8] Casagrande, A. (1932). Research on the atterberg limits of soils. *Public Roads*, *12*(3), 121–136.

[9] Casagrande, D. R. (1982). Memorial to arthur casagrande 1902-1981. *In Proceedings of the Geological Society of America Annual Report*, *13*(1), 1–4.

[10] Gibson, R. E. & Lumb, P. (1982). Numerical solution of some problems in the consolidation of clay. *In Proceedings of the Institution of Civil Engineers*, *2*(2), 182–198. https://doi.org/https://doi.org/10.1680/iicep.1953.11031

[11] Nordendahl, E. (1928). *Beskrivning over nya lidingobron byggd aren 1917-1926 (description of the new lidingo bridge constructed in 1917-1926)*. Lidingöbrostyrelsen.

[12] Vey, E. & Schlesinger, L. (1949). Soil shear tests by means of rotary vanes. *In Proceedings of the Highway Research Board*, *29*, 552–554.

[13] Lea, N. D. & Benedict, B. D. (1953). Foundation vane tester for measuring in situ shear strength of soil. *National Research Council, Canada, Associate Committee on Soil and Snow Mechanics Technical Memo*, *27*, 60–68.

[14] Cadling, L. & Odenstad, S. (1950). The vane borer, an apparatus for determining the shear strength of clay soils directly in the ground. *Royal Swedish Geotechnical Institute Proceedings*, *2*(2), 98–182.

[15] Morton, J. P., O'Loughlin, C. D. & White, D. J. (2016). Estimation of soil strength in fine-grained soils by instrumented free-fall sphere tests. *Géotechnique*, *66*(12), 959–968. https://doi.org/https://doi.org/10.1680/jgeot.15.P.038

[16] Randolph, M. F., Stanier, S. A., O'Loughlin, C. D., Chow, S. H., Bienen, B., Doherty, J. P., Mohr, H., Ragni, R., Schneider, M. A., White, D. J. & Schneider, J. A. (2018). Penetrometer equipment and testing techniques for offshore design of foundations, anchors and pipelines. *In Proceedings of the 4th International Symposium on Cone Penetration Testing*, *4*, 3–23.

[17] Thompson, D., March, R. & Herrmann, H. (2002). Ground truth results for dynamic penetrometers in cohesive soils. *In Proceedings of OCEANS 2002, MTS/IEEE—Marine Frontiers: Reflection of the Past, Visions of the Future*, *4*, 2117–2123. https://doi.org/https://doi.org/10.1109/OCEANS.2002.1191958

[18] Peterson, D. L., Siekmeier, J. & Nelson, C. R. (2006). Intelligent soil compaction technology: Results and a roadmap toward widespread use. *In Proceedings of OCEANS 2002, MTS/IEEE—Marine Frontiers: Reflection of the Past, Visions of the Future*, *1975*(1), 81–88. https://doi.org/https://doi.org/10.1177/0361198106197500109

[19] Chang, G., Xu, Q., Rutledge, J., Horan, B., Michael, L., White, D. & Vennapusa, P. (2011). *Accelerated implementation of intelligent compaction technology for embankment subgrade soils, aggregate base, and asphalt pavement materials* (tech. rep.). US Department of Transportation.

[20] Altese, E., Bolognani, O., Mancini, M. & Troch, P. A. (1996). Retrieving soil moisture over bare soil from ers 1 synthetic aperture radar data: Sensitivity analysis based on a theoretical surface scattering model and field data. *Water Resources Research*, *32*(3), 653–661. https://doi.org/https://doi.org/10.1029/95WR03638

[21] Stark, N., Sheppard, J., Graber, H. C., McNinch, J. E. & Wadman, H. M. (2018). Geotechnical characterization of beach sediments using sar: Ideas, challenges and preliminary data. *In Proceedings of EUSAR*, 1316–1319.

[22] Stark, N., McNinch, J. E., Wadman, H. M., Graber, H. C., Albatal, A. & Mallas, P. A. (2017). Friction angles at sandy beaches from remote imagery. *Géotechnique Letters*, *7*(4), 292–297. https://doi.org/https://doi.org/10.1680/jgele.17.00053

[23] Stark, N., Hay, A. E. & Trowse, G. (2014). Cost-effective geotechnical and sedimentological early site assessment for ocean renewable energies. *In Proceedings of Oceans - St. John's*. https://doi.org/https://doi.org/10.1109/OCEANS.2014.7003004

[24] Paprocki, J., Stark, N., Graber, H. C., McNinch, J. E. & Wadman, H. M. (2019). Use of multispectral imagery for geotechnical characterization of sandy beach sediments. *In Proceedings of Coastal Sediments*, 2553–2565. https://doi.org/https://doi.org/10.1142/9789811204487_0220

[25] Gelin, J. C. & Ghouati, O. (1994). An inverse method for determining viscoplastic properties of aluminium alloys. *Journal of Materials Processing Technology*, *45*(1), 435–440. https://doi.org/https://doi.org/10.1016/0924-0136(94)90378-6

[26] Gavrus, A., Massoni, E. & Chenot, J. L. (1996). An inverse analysis using a finite element model for identification of rheological parameters. *Journal of Materials Processing Technology*, *60*(1), 447–454. https://doi.org/https://doi.org/10.1016/0924-0136(96)02369-2

[27] Inoue, H., Harrigan, J. J. & Reid, S. R. (2001). Review of inverse analysis for indirect measurement of impact force. *Applied Mechanics Reviews*, *54*(6), 503–524. https://doi.org/https://doi-org.turing.library.northwestern.edu/10.1115/1.1420194

[28] Bolzon, G., Maier, G. & Panico, M. (2004). Material model calibration by indentation, imprint mapping and inverse analysis. *International Journal of Solids and Structures*, *41*(11), 2957–2975. https://doi.org/https://doi.org/10.1016/j.ijsolstr.2004.01.025

[29] Yin, Z. Y., Jin, Y. F., Shen, J. S. & Hicher, P. Y. (2017). Optimization techniques for identifying soil parameters in geotechnical engineering: Comparative study and enhancement. *International Journal for Numerical and Analytical Methods in Geomechanics*, *42*(1), 70–94. https://doi.org/https://doi.org/10.1002/nag.2714

[30] Zentar, R., Hicher, P. Y. & Moulin, G. (2001). Identification of soil parameters by inverse analysis. *Computers and Geotechnics*, *28*(2), 129–144. https://doi.org/https://doi.org/10.1016/S0266-352X(00)00020-3

[31] Obrzud, R. F., Vulliet, L. & Truty, A. (2009). Optimization framework for calibration of constitutive models enhanced by neural networks. *International Journal for Numerical and*

Analytical Methods in Geomechanics, *33*(1), 71–94. https://doi.org/https://doi.org/10.1002/nag.707

[32] Zhang, Y., Gallipoli, D. & Augarde, C. (2013). Parameter identification for elasto-plastic modelling of unsaturated soils from pressuremeter tests by parallel modified particle swarm optimization. *Computers and Geotechnics*, *48*, 293–303. https://doi.org/https://doi.org/10.1016/j.compgeo.2012.08.004

[33] Yu, Y., Zhang, B. & Yuan, H. (2007). An intelligent displacement back-analysis method for earth-rockfill dams. *Computers and Geotechnics*, *34*(6), 423–434. https://doi.org/https://doi.org/10.1016/j.compgeo.2007.03.002

[34] Vardakos, S., Gutierrez, M. & Xia, C. (2012). Parameter identification in numerical modeling of tunneling using the differential evolution genetic algorithm (dega). *Tunnelling and Underground Space Technology*, *28*(0), 109–123. https://doi.org/https://doi.org/10.1016/j.tust.2011.10.003

[35] Moreira, N., Miranda, T., Pinheiro, M., Fernandes, P., Dias, D., Costa, L. & Sena-Cruz, J. (2013). Back analysis of geomechanical parameters in underground works using an evolution strategy algorithm. *Tunnelling and Underground Space Technology*, *33*(0), 143–158. https://doi.org/https://doi.org/10.1016/j.tust.2012.08.011

[36] Constantinescu, A. & Tardieu, N. (2001). On the identification of elastoviscoplastic constitutive laws from indentation tests. *Inverse Problems in Engineering*, *9*(1), 19–44. https://doi.org/https://doi.org/10.1080/174159701088027751

[37] Nakamura, T. & Gu, Y. (2007). Identification of elastic–plastic anisotropic parameters using instrumented indentation and inverse analysis. *Mechanics of Materials*, *39*(4), 340–356. https://doi.org/https://doi.org/10.1016/j.mechmat.2006.06.004

[38] Zhang, Y., Hart, J. D. & Needleman, A. (2019). Identification of plastic properties from conical indentation using a bayesian-type statistical approach. *Journal of Applied Mechanics*, *86*(1). https://doi.org/https://doi.org/10.1115/1.4041352

[39] Cao, Z. & Wang, Y. (2013). Bayesian approach for probabilistic site characterization using cone penetration tests. *Journal of Geotechnical and Geoenvironmental Engineering*, *139*(2), 267–276. https://doi.org/https://doi.org/10.1061/(ASCE)GT.1943-5606.0000765

[40] Ben-Dor, G., Dubinsky, A. & Elperin, T. (2010). Some inverse problems in penetration mechanics. *Mechanics Based Design of Structures and Machines*, *38*, 468–480. https://doi.org/https://doi.org/10.1080/15397734.2010.501274

[41] Oberai, A. A., Gokhale, N. H. & Feijóo, G. R. (2003). Solution of inverse problems in elasticity imaging using the adjoint method. *Inverse Problems*, *19*. https://doi.org/https://doi.org/10.1088/0266-5611/19/2/304

[42] Bonnet, M. & Constantinescu, A. (2005). Inverse problems in elasticity. *Inverse Problems*, *21*, R1–R50. https://doi.org/https://doi.org/10.1088/0266-5611/21/2/R01

[43] Eschenauer, H. A. & Olhoff, N. (2001). Topology optimization of continuum structures: A review. *Applied Mechanics Reviews*, *54*(4), 331–390. https://doi.org/https://doi.org/10.1115/1.1388075

[44] Sigmund, O. & Maute, K. (2013). Topology optimization approaches. *Structural and Multidisciplinary Optimization*, *48*, 1031–1055. https://doi.org/https://doi.org/10.1007/s00158-013-0978-6

[45] Camp, C. V. & Akin, A. (2011). Design of retaining walls using big bang–big crunch optimization. *Journal of Structural Engineering*, *138*(3), 438–448. https://doi.org/https://doi.org/10.1061/(ASCE)ST.1943-541X.0000461

[46] Talatahari, S. & Sheikholeslami, R. (2014). Optimum design of gravity and reinforced retaining walls using enhanced charged system search algorithm. *KSCE Journal of Civil Engineering*, *18*(5), 1462–1469. https://doi.org/https://doi.org/10.1007/s12205-014-0406-5

[47] Ponterosso, P. & Fox, D. S. J. (2000). Optimization of reinforced soil embankments by genetic algorithm. *International Journal for Numerical and Analytical Methods in Geomechanics*, *24*(4), 425–433. https://doi.org/https://doi.org/10.1002/(SICI)1096-9853(20000410)24:43.0.CO;2-V

[48] Basudhar, P. K., Vashistha, A., Deb, K. & Dey, A. (2008). Cost optimization of reinforced earth walls. *Geotechnical and Geological Engineering*, *26*(1), 1–12. https://doi.org/https://doi.org/10.1007/s10706-007-9143-6

[49] Basha, B. M. & Babu, G. S. (2009). Optimum design for external seismic stability of geosynthetic reinforced soil walls: Reliability based approach. *Journal of Geotechnical and Geoenvironmental Engineering*, *136*(6), 797–812. https://doi.org/https://doi.org/10.1061/(ASCE)GT.1943-5606.0000289

[50] Khajehzadeh, M., Taha, M. R., El-Shafie, A. & Eslami, M. (2012). Optimization of shallow foundation using gravitational search algorithm. *Research Journal of Applied Sciences*, *4*(9), 1124–1130.

[51] amd A R Kashani, A. H. G. (2017). Construction cost minimization of shallow foundation using recent swarm intelligence techniques. *IEEE Transactions on Industrial Informatics*, *14*(3), 1099–1106. https://doi.org/https://doi.org/10.1109/TII.2017.2776132

[52] Kashani, A. R., Chiong, R., Mirjalili, S. & Gandomi, A. H. (2021). Particle swarm optimization variants for solving geotechnical problems: Review and comparative analysis.

Computational Methods in Engineering, *28*, 1871–1927. https://doi.org/https://doi.org/10.1007/s11831-020-09442-0

[53] Cheng, Y. M., Li, L., Lansivaara, T., Chi, S. C. & Sun, Y. J. (2008). An improved harmony search minimization algorithm using different slip surface generation methods for slope stability analysis. *Engineering Optimization*, *40*(2), 95–115. https://doi.org/https://doi.org/10.1080/03052150701618153

[54] Samui, P. (2008). Slope stability analysis: A support vector machine approach. *Environmental Earth Sciences*, *56*(2), 255–267. https://doi.org/https://doi.org/10.1007/s00254-007-1161-4

[55] Zhao, H., Yin, S. & Ru, Z. (2012). Relevance vector machine applied to slope stability analysis. *International Journal for Numerical and Analytical Methods in Geomechanics*, *36*(5), 643–652. https://doi.org/https://doi.org/10.1002/nag.1037

[56] Rubio, E., Hall, J. W. & Anderson, M. G. (2004). Uncertainty analysis in a slope hydrology and stability model using probabilistic and imprecise information. *Computers and Geotechnics*, *31*(7), 529–536. https://doi.org/https://doi.org/10.1016/j.compgeo.2004.09.002

[57] Sengupta, A. & Upadhyay, A. (2009). Locating the critical failure surface in a slope stability analysis by genetic algorithm. *Applied Soft Computing*, *9*(1), 387–392. https://doi.org/https://doi.org/10.1016/j.asoc.2008.04.015

[58] Gao, W. (2015). Determination of the noncircular critical slip surface in slope stability analysis by meeting ant colony optimization. *Journal of Computing in Civil Engineering*, *30*(2), 06015001.1–06015001.10. https://doi.org/https://doi.org/10.1061/(ASCE)CP.1943-5487.0000475

[59] Nejad, F. P., Jaksa, M. B., Kakhi, M. & McCabe, B. A. (2009). Prediction of pile settlement using artificial neural networks based on standard penetration test data. *Computers and Geotechnics*, *36*(7), 1125–1133. https://doi.org/https://doi.org/10.1016/j.compgeo.2009.04.003

[60] Das, S. K. & Basudhar, P. K. (2006). Undrained lateral load capacity of piles in clay using artificial neural network. *Computers and Geotechnics*, *33*(8), 454–459. https://doi.org/https://doi.org/10.1016/j.compgeo.2006.08.006

[61] Pal, M. & Deswal, S. (2010). Modelling pile capacity using gaussian process regression. *Computers and Geotechnics*, *37*(7), 942–947. https://doi.org/https://doi.org/10.1016/j.compgeo.2010.07.012

[62] Ardalan, H., Eslami, A. & Nariman-Zadeh, N. (2009). Piles shaft capacity from cpt and cptu data by polynomial neural networks and genetic algorithms. *Computers and Geotechnics*, *34*(4), 616–625. https://doi.org/https://doi.org/10.1016/j.compgeo.2008.09.003

[63] Tarawneh, B. (2013). Pipe pile setup: Database and prediction model using artificial neural network. *Soils and Foundations*, *53*(4), 607–615. https://doi.org/https://doi.org/10.1016/j.sandf.2013.06.011

[64] Castillo, E., Gutierrez, J. M. & Hadi, A. S. (1997). Sensitivity analysis in discrete bayesian networks. *IEEE Transactions on Systems, Man, and Cybernetics: Systems*, *27*(4), 412–423. https://doi.org/https://doi.org/10.1109/3468.594909

[65] Saltelli, A., Chan, K. & Scott, E. M. (2000). *Sensitivity analysis: Gauging the worth of scientific models*. Wiley, New York.

[66] Hill, M. C. (2010a). *Methods and guidelines for effective model calibration* (tech. rep.). US Geological Survey Water-Resources Investigations Report 98-4005.

[67] Taguchi, G., Chowdhury, S. & Taguchi, S. (2000). *Learn how to boost quality while reducing costs and time to market*. McGraw–Hill, New York.

[68] Park, G. J., Lee, T. H., Lee, K. H. & Hwang, K. H. (2006). Robust design: An overview. *American Institute of Aeronautics and Astronautics*, *44*(1), 181–191. https://doi.org/https://doi.org/10.2514/1.13639

[69] Eschenauer, H. A., Kobelev, V. V. & Schumacher, A. (1994). Bubble method for topology and shape optimization of structures. *Structural Optimization*, *8*, 42–51. https://doi.org/https://doi.org/10.1007/BF01742933

[70] Novotny, A. A., Feijoo, R. A., Taroco, E. & Padra, C. (2003). Topological sensitivity analysis. *Computer Methods in Applied Mechanics and Engineering*, *192*(7-8), 803–829. https://doi.org/ttps://doi.org/10.1016/S0045-7825(02)00599-6

[71] Hill, M. C. (2010b). *A computer program (modflowp) for estimating parameters of a transient, three-dimensional, ground-water flow model using nonlinear regression* (tech. rep.). US Geological Survey Water Resources Investigations Report 98-4005.

[72] Anderman, E. R., Hill, M. C. & Poeter, E. P. (1996). Two-dimensional advective transport in ground-water flow parameter estimation. *Ground Water*, *34*(6), 1001–1009. https://doi.org/https://doi.org/10.1111/j.1745-6584.1996.tb02165.x

[73] Poeter, E. P. & Hill, M. C. (1997). Inverse models, a necessary next step in groundwater modeling. *Ground Water*, *35*(2), 250–260. https://doi.org/https://doi.org/10.1111/j.1745-6584.1997.tb00082.x

[74] Gooseff, M. N., Bencala, K. E., Scott, D. T., Runkel, R. L. & McKnight, D. M. (2005). Sensitivity analysis of conservative and reactive stream transient storage models applied to field data from multiple-reach experiments. *Advances in Water Resources*, *28*(5), 479–492. https://doi.org/https://doi.org/10.1016/j.advwatres.2004.11.012

[75] Barlebo, H. C., Hill, M. C., Rosbjerg, D. & Jensen, K. H. (1998). Concentration data and dimensionality in groundwater models: Evaluation using inverse modelling. *Hydrology Research*, *29*(3), 149–178. https://doi.org/https://doi.org/10.2166/nh.1998.0009

[76] Mehl, S. W. & Hill, M. C. (2001). A comparison of solute-transport solution techniques and their effect on sensitivity analysis and inverse modeling results. *Ground Water*, *39*(2), 300–307. https://doi.org/https://doi.org/10.1111/j.1745-6584.2001.tb02312.x

[77] Foglia, L., Hill, M. C., Mehl, S. W. & Burlando, P. (2009). Sensitivity analysis, calibration and testing of a distributed hydrological model using an error-weighted objective function. *Water Resources Research*, *45*(6), W06427.1–W06427.18. https://doi.org/https://doi.org/10.1029/2008WR007255

[78] Phadke, M. S. (1995). *Quality engineering using robust design*. Prentice Hall PTR Upper Saddle River NJ United States.

[79] Kontoravdi, C., Asprey, S. P., Pistikopoulos, E. N. & Mantalaris, A. (2005). Application of global sensitivity analysis to determine goals for design of experiments: An example study on antibody-producing cell cultures. *Biotechnology Progress*, *21*(4), 1128–1135. https://doi.org/https://doi.org/10.1021/bp050028k

[80] Morris, M. D. (1991). Factorial sampling plans for preliminary computational experiments. *Technometrics*, *33*(2), 161–174. https://doi.org/https://doi.org/10.2307\%2F1269043

[81] Sobol, I. M. (2001). Global sensitivity indices for nonlinear mathematical models and their monte carlo estimates. *Mathematics and Computers in Simulation*, *55*(1), 271–280. https://doi.org/https://doi.org/10.1016/S0378-4754(00)00270-6

[82] Gupta, S. R. H. V. (2015). What do we mean by sensitivity analysis? the need for comprehensive characterization of "global" sensitivity in earth and environmental systems models. *Water Resources Research*, *51*(5), 3070–3092. https://doi.org/https://doi.org/10.1002/2014WR016527

[83] Iooss, B. & Lemaître, P. (2015). A review on global sensitivity analysis methods. *Uncertainty Management in Simulation-Optimization of Complex Systems*, *59*, 101–122. https://doi.org/https://doi.org/10.1007/978-1-4899-7547-8_5

[84] Vajda, S., Valko, P. & Turányi, T. (1985). Principal component analysis of kinetic models. *International Journal of Chemical Kinetics*, *17*(1), 55–81. https://doi.org/https://doi.org/10.1002/kin.550170107

[85] Bekker, G. (1956). *Theory of land locomotion*. University of Michigan Press.

[86] Bekker, G. (1960). *Off the road locomotion*. University of Michigan Press.

[87] Bekker, G. (1969). *Introduction to terrain-vehicle systems*. University of Michigan Press.

[88] Wong, J. & Reece, A. (1967). Prediction of rigid wheel performance based on the analysis of soil-wheel stresses, part i and part ii. *Journal of Terramechanics*, *4*(1), 81–98. https://doi.org/https://doi.org/10.1016/0022-4898(67)90105-X

[89] Nohse, Y., Hashuguchi, K., Ueno, M., Shikanai, T., Izumi, H. & Koyama, F. (1991). A measurement of basic mechanical quantities of off-the-road traveling performance. *Journal of Terramechanics*, *28*(4), 359–371. https://doi.org/https://doi.org/10.1016/0022-4898(91)90017-Z

[90] Shmulevich, I., Ronai, D. & Wolf, D. (1996). A new field single wheel tester. *Journal of Terramechanics*, *33*(3), 133–141. https://doi.org/https://doi.org/10.1016/S0022-4898(96)00014-6

[91] Rathje1, E. M., Woo, K. & Crawford, M. (2006). Spaceborne and airborne remote sensing for geotechnical applications. *In Proceedings of GeoCongress*. https://doi.org/https://doi.org/10.1061/40803(187)2

[92] Baumann, P. (2019). Dc-10 - aerial photography: History and georeferencing. *The Geographic Information Science and Technology Body of Knowledge*, *2*. https://doi.org/https://doi.org/10.22224/gistbok/2019.2.5

[93] Schaefer, V. R., Burckhard, S. R. & Boomer, J. A. (2005). Landslide mapping with airborne laser swath mapping (alsm): Accuracy assessment. *In Proceedings of Geo-Frontiers Congress*, 2001–2012. https://doi.org/https://doi.org/10.1061/40785(164)1

[94] Rathje, E. M. & Franke, K. (2016). Remote sensing for geotechnical earthquake reconnaissance. *Soil Dynamics and Earthquake Engineering*, *91*, 304–316. https://doi.org/http://dx.doi.org/10.1016/j.soildyn.2016.09.016

[95] Hashash, Y., Oliveira, F. J., Su, Y. Y. & Liu, L. Y. (2005). 3d laser scanning for tracking supported excavation construction. *In Proceedings of Geo-Frontiers Congress*, 2013–2022. https://doi.org/https://doi.org/10.1061/40785(164)2

[96] Manduchi, R., Castano, A., Talukder, A. & Matthies, L. (2005). Obstacle detection and terrain classification for autonomous off-road navigation. *Autonomous Robots*, *18*, 81–102. https://doi.org/https://doi.org/10.1023/B:AURO.0000047286.62481.1d

[97] Stimson, G. W. (1983). *Introduction to airborne radar*. University of Michigan Press.

[98] Stark, N., Brilli, N., Paprocki, J. & Florence, M. (2021). In situ and remotely sensed data collection for geotechnical site characterization of intertidal environments with regards to extreme events. *In Proceedings of Geo-Extreme*, 382–392. https://doi.org/https://doi.org/10.1061/9780784483688.038

[99] Stark, N., Wilkens, R., Ernstsen, V. B., Lambers-Huesmann, M., Stegmann, S. & Kopf, A. (2021). Geotechnical properties of sandy seafloors and the consequences for dynamic penetrometer interpretations: Quartz sand versus carbonate sand. *Geotechnical and Geological Engineering*, *30*(1), 1–14. https://doi.org/https://doi.org/10.1007/s10706-011-9444-7

[100] Zekkos, D., Greenwood, W., Lynch, J., Manousakis, J., Athanasopoulos-Zekkos, A., Clark, M., Cook, K. L. & Saroglou, C. (2018). Lessons learned from the application of uav-enabled structure-from-motion photogrammetry in geotechnical engineering. *International Journal of Geoengineering Case Histories*, *4*(4), 254–274. https://doi.org/http://doi.org/10.4417/IJGCH-04-04-03

[101] Stark, N., Wilkens, R., Ernstsen, V. B., Lambers-Huesmann, M., Stegmann, S. & Kopf, A. (2016). Reconnaissance of two liquefaction sites using small unmanned aerial vehicles and structure from motion computer vision following the april 1, 2014 chile earthquake. *Journal of Geotechnical and Geoenvironmental Engineering*, *143*(5). https://doi.org/https://doi.org/10.1061/(ASCE)GT.1943-5606.0001647

[102] Greenwood, W., Zekkos, D., Clark, M. K., Lynch, J. P., Bateman, J. & Chamlagain, D. (2016). Uav-based 3-d characterization of rock masses and rock slides in nepal. *In Proceedings of 50th US Rock Mechanics/Geomechanics Symposium*.

[103] Zekkos, D., Manousakis, J., Greenwood, W. & Lynch, J. (2016). Immediate uav-enabled infrastructure reconnaissance following recent natural disasters: Case histories from greece. *In Proceedings of 1st International Conference on Natural Hazards and Infrastructure*.

[104] Nally, A., Shi, Z. & Hambleton, J. P. (2019). Optimal deformation modes for estimating soil properties. *In Proceedings of GeoCongress*. https://doi.org/https://doi.org/10.1061/9780784482124.055

[105] ASTM. (2018). E9-09: Standard test methods of compression testing of metallic materials at room temperature. https://doi.org/https://doi.org/10.1520/E0009-09

[106] ASTM. (2016). E290-14: Standard test methods for bend testing of material for ductility. https://doi.org/https://doi.org/10.1520/E0290-14

[107] Heppell, S. S., Caswell, H. & Crowder, L. B. (2000). Life histories and elasticity patterns: Perturbation analysis for species with minimal demographic data. *Ecology*, *81*(3), 654–665. https://doi.org/https://doi.org/10.1890/0012-9658(2000)081[0654:LHAEPP]2.0.CO;2

[108] Link, W. A. & Doherty, P. F. (2002). Scaling in sensitivity analysis. *Ecology*, *83*(12), 3299–3305. https://doi.org/https://doi.org/10.2307/3072080

[109] Pianosi, F., Beven, K., Freer, J., Hall, J. M., Rougier, J., Stephenson, D. B. & Wagener, T. (2016). Sensitivity analysis of environmental models: A systematic review with practical

workflow. *Environmental Modelling and Software*, *79*, 214–232. https://doi.org/https://doi.org/10.1016/j.envsoft.2016.02.008

[110] E, D. T. (1986). A comparison of forecasts from least absolute value and least squares regression. *Journal of Forecasting*, *5*(3), 189–195. https://doi.org/https://doi.org/10.1002/for.3980050305

[111] Ge, M. (1997). Comparison of least squares and absolute value methods in ae/ms source location: A case study. *International Journal of Rock Mechanics and Mining Sciences*, *34*(3-4), 93.el–93.e7. https://doi.org/https://doi.org/10.1016/S1365-1609(97)00077-4

[112] ASTM. (2010). D2166-06: Standard test method for unconfined compressive strength of cohesive soil. https://doi.org/https://doi.org/10.1520/D2166-06

[113] ASTM. (2020a). D4767-11: Standard test method for consolidated undrained triaxial compression test for cohesive soils. https://doi.org/https://doi.org/10.1520/D4767-11R20

[114] ASTM. (2020b). D7181-20: Standard test method for consolidated drained triaxial compression test for soils. https://doi.org/https://doi.org/10.1520/D7181-20

[115] Darvell, B. W. (1990). Uniaxial compression tests and the validity of indirect tensile strength. *Journal of Material Science*, *25*, 757–780. https://doi.org/https://doi.org/10.1007/BF03372161

[116] The Optimization Firm. (2019). *Baron*. https://minlp.com/baron-solver

[117] AMPL. (2019). https://ampl.com

[118] Artelys. (2021). *Knitro* (Version 12.3.0). https://www.artelys.com/solvers/knitro

[119] Livesley, R. K. (1983). *Finite elements: An introduction for engineers*. Cambridge University Press.

[120] Wood, D. M. (2004). *Geotechnical modelling*. CRC Press.

[121] WOLFRAM. (2021). *Mathematica* (Version 12.1). https://www.wolfram.com/mathematica

[122] Gallagher, E., Wadman, H., McNinch, J., Reniers, A. & Koktas, M. (2016). A conceptual model for spatial grain size variability on the surface of and within beaches. *Journal of Marine Science and Engineering*, *4*(2). https://doi.org/https://doi.org/10.3390/jmse4020038

[123] Bentley. (2017). *Plaxis2d* (Version 2017). https://www.bentley.com/en/products/product-line/geotechnical-engineering-software/plaxis-2d

[124] Finno, R. J. & Cavello, M. (2005). Supported excavations: Observational method and inverse modeling. *Journal of Geotechnical and Geoenvironmental Engineering*, *131*(7), 826–836. https://doi.org/https://doi.org/10.1061/(ASCE)1090-0241(2005)131:7(826)

[125] Rachea, C. (2006). *Inverse analysis of excavations in urban environments* (tech. rep.). Northwestern University, Evanston, IL.

[126] Winston, P. H. (1992). *Artificial intelligence (3rd ed.)* Addison-Wesley Longman Publishing Co., Inc.

[127] Chung, C. J. & Reynolds, R. G. (1998). Caep: An evolution-based tool for real-valued function optimization using cultural algorithms. *International Journal on Artificial Intelligence Tools*, *7*(3), 239–291. https://doi.org/https://doi.org/10.1142/S0218213098000135

[128] Jin, R., Chen, W. & Simpson, T. W. (2001). Comparative studies of metamodelling techniques under multiple modelling criteria. *Structural and Multidisciplinary Optimization*, *23*, 1–13. https://doi.org/https://doi.org/10.1007/s00158-001-0160-4

[129] Doherty, J. & Hunt, R. (2009). Two statistics for evaluating parameter identifiability and error reduction. *Journal of Hydrology*, *366*(1), 119–127. https://doi.org/https://doi.org/10.1016/J.JHYDROL.2008.12.018

Appendices

APPENDIX A
ALTERNATE METRIC FOR THE CLASSIFICATION OF TEST QUALITY

The work presented in this appendix was completed prior to the work contained in the main body of this thesis. This work is not included in the main body of the thesis as it forms the beginning of an alternative track, which was not further investigated.

The first stage in this alternative track is contained in Nally *et al.* [104]. In this publication, the aim is to directly compare select cases of a direct simple shear test, modeled in PLAXIS [123], with the objective of investigating an optimal test. The intention of this work is to use the non-uniform stress and strain fields induced in the test as a means of enhancing the interpretation of material properties. The following question is asked: if more information can be extracted from a test, can better estimates of the material parameters be made? For the direct simple shear test, two models are defined: (1) the *simplified interpretation model* (SIM), as the test where only the resultant forces are measured and (2) the *extended interpretation model* (EIM), as the test where stresses (or displacements) are measured at multiple locations along the top boundary. Furthermore, two sample aspect ratios (sample width (w) to height (h)) are considered, 1:1 and 3:1. For each of the models (SIM and EIM) and aspect ratios, a set of known material parameters (E, ν, ϕ, c and ψ) are selected. An inverse analysis is then used to attempt to accurately return the true material parameters. This process is shown in Figure A.1 and is similar to process that was developed by Finno & Cavello [124] and Rechea [125]. Here an optimization process is started with an initial guess of the material parameters which are used to compute an output in PLAXIS. MATLAB's optimization toolbox uses the output from PLAXIS to inform new material parameters to be sent back to PLAXIS. This process continues until the convergence criteria is met.

To better inform the analysis, the sensitivity of parameters and their dependence on each other is assessed. A parameter sensitivity analysis is completed in order to determine the parameters which are most likely to significantly impact the convergence and are therefore most efficient to

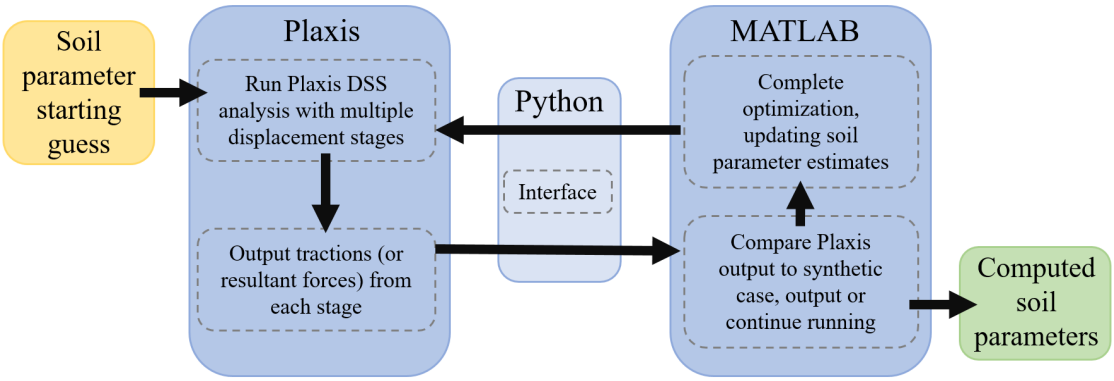

Figure A.1: Inverse analysis procedure.

optimize. An analysis of the correlation between parameters is conducted to determine whether multiple parameters can be optimized simultaneously [73]. The composite scaled sensitivity (CSS) and parameter correlation coefficient (PCC) are both calculated as per the procedure outlined by Poeter & Hill [73].

Figure A.2a presents the CSS for all four of the analyzed models. In all models, the friction angle has the highest sensitivity, closely followed by the elastic modulus, and these are therefore determined as the critical parameters. Although Poisson's ratio is the next most sensitive parameter, the cohesion is selected as another parameter to be further analyzed. This is because the Poisson's ratio of soils often varies within a relatively narrow range, and accordingly a reasonable estimation can be readily made. Figure A.2b gives the computed values of PCC considering the elastic modulus, cohesion and friction angle. A large value of PCC identifies a pair of parameters that have higher correlation, and thus are hard to identify simultaneously. This analysis suggests that the simultaneous identification of the elastic modulus with either cohesion or friction angle through optimization would have a higher chance of retrieving the true parameters than that of an attempt to identify cohesion and friction angle simultaneously. A key objective of this analysis is to identify which of the two models, EIM and SIM, is preferable for discovering the true soil properties. From Figure A.2, one can infer that the EIM could be expected to perform better than the SIM, and the aspect ratio of $w/h = 1$ is presumed to be slightly better than $w/h = 3$. For both aspect ratios, the CSS is generally higher for the EIM, and the PCC is lower for all parameters,

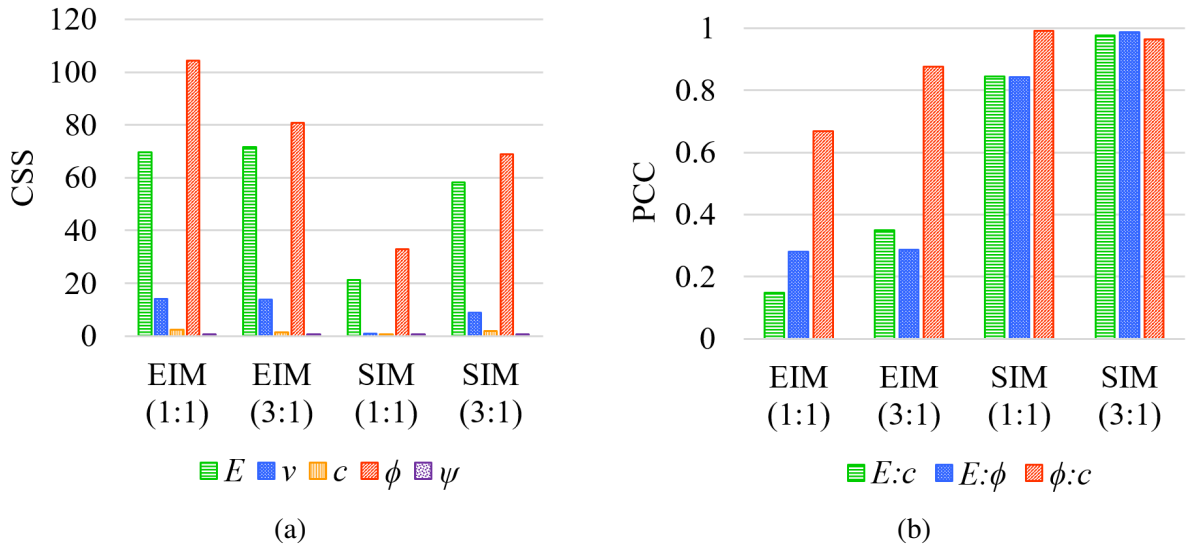

(a) (b)

Figure A.2: Assessment of test at true material parameters: (a) sensitivities; (b) parameter correlations.

which should indicate a better ability to identify the true parameters.

The objective function of the inverse problem (depicted in Figure A.1) is defined as the sum of squared errors, similar to that presented in Equation 4.7. It is postulated that a smooth objective function with a single, well-defined minimum is desired as there is less chance for the optimization to diverge, or to converge to a local minimum. For this analysis the objective functions are plotted for two material parameters (E and ϕ) and all the assessed models, shown in Figure A.3. In these inverse problems only one material parameter is considered unknown at a time, meaning that the objective function is a two-dimensional line. In Figure A.3, it can be seen that in both cases the EIM models have a steeper objective function, and the 3:1 aspect ratio appears to be more impacted by noise. The assessment into the optimal aspect ratio was inconclusive because they had no impact on the accuracy of the predictions of the material parameters. The objective function is greatly impacted by the specimen aspect ratio (Figure A.3), which may ultimately imply that one aspect ratio is preferable to another, although this remained unproven from the analyses conducted.

All optimizations completed in this appendix were run in MATLAB, using the MATLAB optimization toolbox. Optimizations were run for single, two and three-parameter optimization. The analysis was run in PLAXIS as an elastoplastic analysis with a Mohr-Coulomb constitutive model,

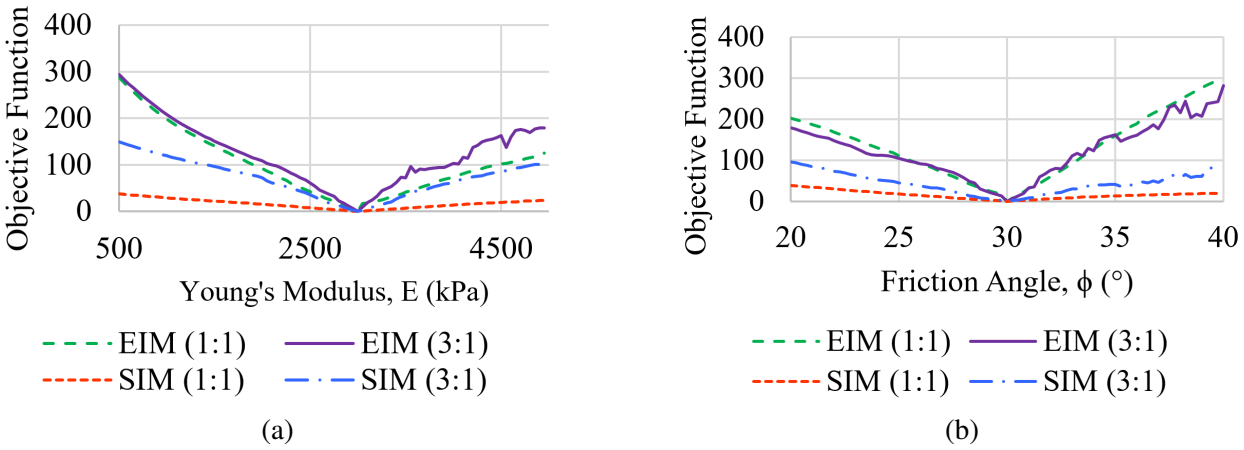

Figure A.3: Objective functions, computed for variation in: (a) E; (b) ϕ.

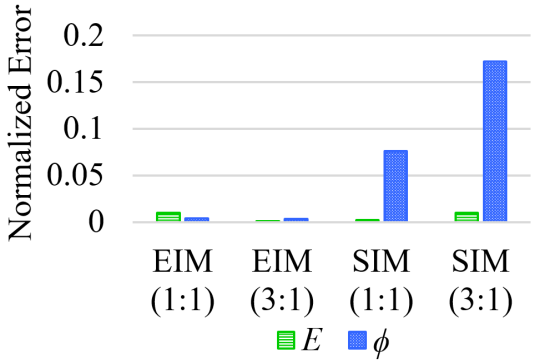

Figure A.4: Normalized error for two-parameter optimizations.

and the material parameters investigated were E, ϕ and c. In single-parameter optimization, when E, ϕ and c are optimized independently, all models and all parameters converge back to the true parameters. In two-parameter optimization, when E and ϕ are optimized together, the models presented reasonable convergence to true parameters. Both EIMs converged to the true parameters and in SIM ϕ presented some error. This is shown in Figure A.4. Finally, in three-parameter optimization, when E, ϕ and c are all optimized together, convergence is heavily dependent on the starting guesses, and the EIM generally performed better. Figure A.5 presents a representative sample of the analysis. In all cases E converged to the true parameters, c presented the largest errors and for the case of Starting Guess #3 the EIM was also able to converge ϕ to the true parameters.

These findings conclude that the treatment of a direct simple shear test as a boundary value

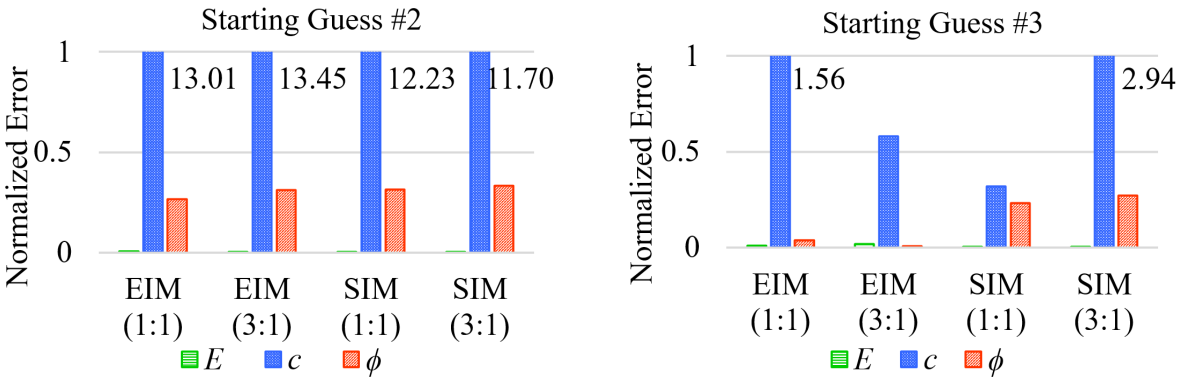

Figure A.5: Normalized error for three-parameter optimizations (the numbers in the plot show values of variables that are outside the range of the axis). Each plot represents the results from different starting guesses

problem rather than the traditional elemental test can potentially lead to a more accurate determination of soil parameters. Further details of the analysis can be found in in the paper by Nally *et al.* [104].

Beyond this analysis, an investigation continued into the quality of the test by assessing the shape of the objective function. The aim was to classify the quality of the test, based on features that help and hinder an optimization. Inspiration comes from multiple works [126–128] that have explored the classification of functions by their features, such as basins, valleys, and parameter correlations. To assess the shape of the objective function's impact on test quality, functions were invented to display a variety of desirable and undesirable features, often referred to as "test functions" for optimization. These invented functions replace the inverse model which is required for an inverse analysis. An example function is presented in Figure A.6.

The proposed metric to compute the quality of the invented functions takes slices of the invented function (IF), which are then fitted with a continuous convex function—a highly desirable function (DF). An optimization is used to fit the DF to the IF, ensuring that the DF remains continuous and convex. The final measure of the test quality is an average of the R^2 of the DF to the

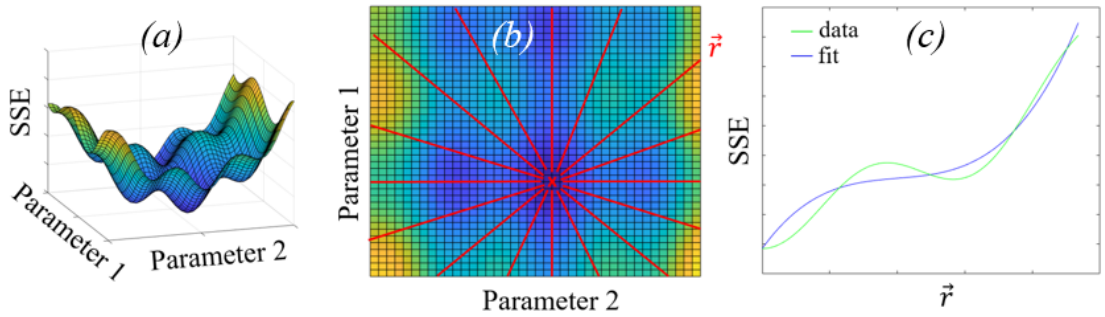

Figure A.6: Test quality measure computation method. (a) function to be assessed, the invented function (IF), (b) slices taken of the IF, and (c) desirable function (DF)—fit, fitted to the invented function (IF)—data.

slice of the IF for all of the slices. This is represented mathematically as

$$Q_{alt} = \frac{1}{n}\sum_{i=1}^{n} w_i a_i \tag{A.1}$$

where n is the number of slices assessed and w_i is a weighting factor applied to each of the slices. The alt subscript is used here to distinguish between this Q and the Q proposed in the body of this thesis. Quantities a_i are the coefficients of determination between the IF data and DF data, and they are computed with

$$a_k = 1 - \frac{\sum_{k=1}^{p}(y_k - y'_k)^2}{\sum_{k=1}^{p}(y_k - \bar{y})^2} \tag{A.2}$$

where p is the step size for computing R^2, y_k are the values of the IF, $\bar{y}$ is the mean of the IF, and y'_k are the DF values. Prior to computing Q_{alt}, an optimization must be used to fit the DF to the IF. This quality measure should be maximized to find the ideal test, with the maximum value of 1.0.

To test the implementation of this proposed metric, inverse analyses are run on the invented functions. In these analyses the true minimum is known, and random starting locations are specified. The inverse analysis works to minimize the SSE and return the location of the true minimum. This analysis showes promising results, suggesting for a higher test quality (indicating a more desirable objective function), the ability to converge was higher. This is further presented in Figure A.7, where each point represents a different invented function (and hence different objective function). The percentage converged was computed over 100 inverse analyses with randomized

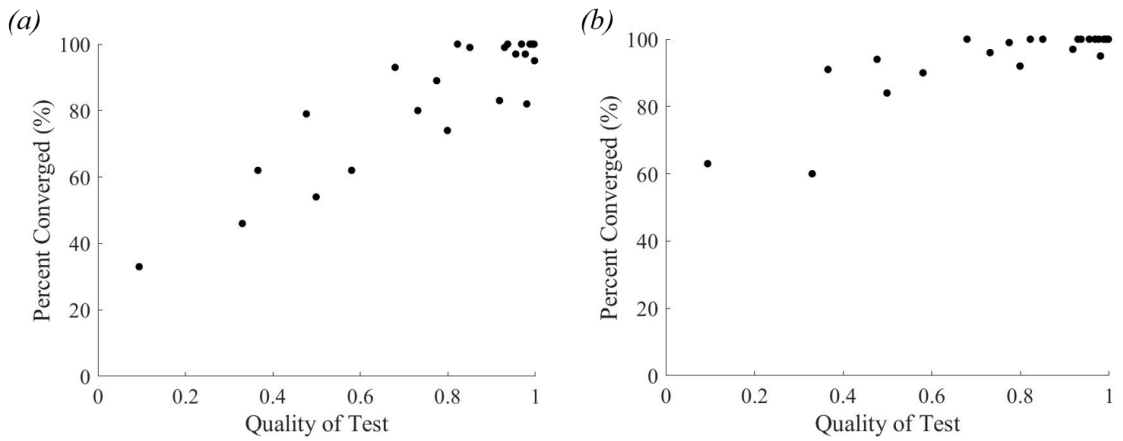

Figure A.7: Test quality measure implementation, assessing convergence using multi-start optimization with (a) 10 starting locations and (b) 20 starting locations.

starting parameters. The two plots present different numbers of starting locations in the multi-start optimization (10 and 20, respectively).

This classification metric for assessing test quality has considerable potential. In addition to the metric described in this appendix, future work in this focus area could incorporate the use of parameter sensitivity and correlation analysis. This can be done by using factors similar to the composite scaled sensitivity (CSS) and parameter correlation coefficient (PCC) simultaneously. When used together, the CSS/PCC analysis can provide considerable information on the ability of a model to identify parameters [129].

This line of work is particularly applicable to the work presented in this thesis, as it is assessing various tests for the quality of the test. However, the work contained in this appendix focuses only on discovering the test that can most easily return the material parameters and does not assess for accuracy of these material parameters. It is expected that future work will aim to incorporate the assessment of the ability of a test to return the material parameters into the metric assessing the quality of the test.

APPENDIX B
SOFTWARE IMPLEMENTATION OF OPTIMIZATION WITH MATLAB, KNITRO, AND OPTUM G2

This appendix outlines the process of implementing the quantitative metric to finite element analysis for the optimization used to determine optimal tests for computing material parameters.

The steps to implement this optimization require various software. A main driver (in this case MATLAB) is used to construct the code, combine other software, and arrange the results. An optimization solver (Artely's KNITRO) is used to iterated between configurations and direct the analysis until it finds a solution. During each iteration, a finite element solver (OPTUM G2) is used to execute the forward model and inform the main driver and optimization solver of the model results.

This appendix details the selections of the software used, including reference to other known options of comparable software. Following this is a detailed account of the implementation and integration of the three software.

B.1 Selection of software—MATLAB, KNITRO and OPTUM G2

The combination of software used in this analysis was selected through assessing the various features of each of the software and through trial and error. This may not be the best combination to solve the problems presented, however, it is well and truly sufficient. It has been proven to work, runs efficiently, and can be modified with ease.

OPTUM G2 is a geotechnical finite element analysis software that is fast and user-friendly. It is aimed at providing advanced finite element analysis packages that are accessible to engineering practitioners. The most significant feature of OPTUM G2 to this thesis is that it can be run from the command window without opening the program. In optimization the function (in this case Q) needs to be called 100s to possibly 1000s of times, and each function call will need multiple calls

to OPTUM G2. Therefore the time it takes to open a program (10-20 seconds) can add significant time to the optimization run time. Furthermore, OPTUM G2 has a very user-friendly integration with MATLAB. The script for executing the OPTUM G2 analysis is saved for all projects when the model is created, and all model parameters can be easily adjusted by replacing their respective values in this script with variables. OPTUM G2 offers 12 constitutive models, all of which can be modified from MATLAB. Both PLAXIS and ABAQUS were trialed prior to OPTUM G2, however any increase they provided in additional features was far outweighed by OPTUM G2's ability to save time and run through the command window. Finally, an open source finite element solver was briefly trialed before it was determined that the benefit in the ability to manipulate the solver was not beneficial to the aims of this work. It is expected that future work could require the implementation of this work into a more robust solver in order to allow for more complex manipulation of the constitutive model. Provided the new solver can integrate with MATLAB, this change would not require significant modification.

For the optimization solver, preference was given to Artelys Knirto (Knirto) for its ability to solve highly non linear problems. Other solvers such as the optimization or global optimization toolbox in MATLAB were initially considered but deemed infeasible in their ability to solve the problems presented in this work. Furthermore, BARON by The Optimization Firm, was used on some of the simple analytical optimizations as it is a very powerful global optimization solver. However, BARON cannot work with a black box solver and therefore could not be integrated with a finite element solver.

Finally, the selection of MATLAB as the driver for the whole setup was simple. Both KNITRO and OPTUM G2 have existing documentation on their application in MATLAB. Furthermore, MATLAB is so universally known and heavily used that even someone who has not used it before could continue the work started here with minimal difficulty. An alternative to MATLAB would be constructing the script in Python.

B.2 Integration of software for optimization—MATLAB, KNITRO and OPTUM G2

A simplified layout of software integration is presented in Figure 4.1. The general movement through the code commences with a MATLAB main driver, which engages the Knirto solver. Then, within the KNITRO solver, the object function is computed, which is facilitated by a MATLAB function and requires $n + 1$ calls to OPTUM G2 (where n is the number of parameter sensitivities included in the analysis). In order to run OPTUM G2, three MATLAB functions are used to update the run script, run the program, and read the results file. Finally, during the whole optimization process KNITRO ensures that predetermined constraints are enforced before a solution is specified. The actual optimization the process requires many internal repetitions prior to specifying a solution.

The following subsections expand on each of the software specifics, covering a more detailed assessment of each aspect of the optimization process within the integration of these three programs.

B.2.1 Specifics for MATLAB

MATLAB is the main driver of this analysis, and this consists of six main code/functions. An overview of the layout of these six code/functions is presented in Figure B.1. The script $Maindriver$ runs the whole program and ultimately calls the KNITRO solver, which in turn calls the function $Objectivefunction$. Within $Objectivefunction$, the function $RunOPTUMG2$ is called. It is within this function both $UpdateOPTUMG2script$ and $Readresultsfile$ are executed. Finally, the function $Optimizationconstraints$ is called by the KNITRO solver. Details of each of these code/functions are presented below.

Main driver: Used to initialize the variables and specify the bounds placed on the variables. This code also contains the KNITRO specifications and the call to solve the optimization with KNITRO. All of the constant parameters such as bounds and fixed parameters are written to text files so as they can be retrieved in the subsequent functions. The main driver can also include

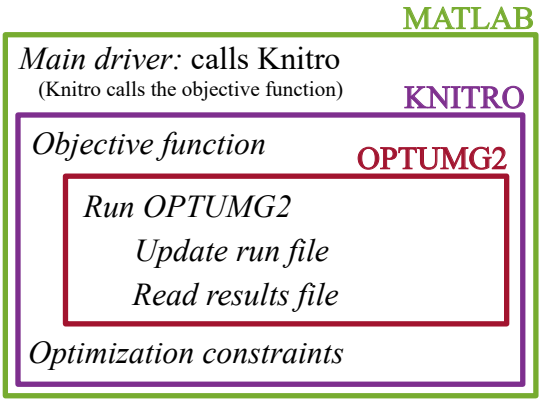

Figure B.1: Layout of MATLAB process.

a loop to solve multiple optimizations in a single run, for example if the objective is to find the optimal configurations for multiple different material types individually.

Objective function: This function is called by KNITRO many times during the optimization. It must retrieve the required constants and fixed parameters from the text files and specify the weights to be used in the computation of the quantitative metric. An excerpt of the code used to compute the objective function is inserted below.

```
Δ = compOptum(paras); % true displacement for parameter set
% Loop to compute each of the objective function terms
for i=1:n
    parameter_s(i) = paras(i)+steps(i); % applies a perturbation to ...
       each parameter
    parameter_t = paras;
    parameter_t(i) = parameter_s(i); % replace the parameter of ...
       interest with the stepped parameter
    Δstepped = compOptum(parameter_t); %compute new displacement
    % computation of normalized weighted parameter sensitivity
    term(i) = ((((Δstepped-Δ)/steps(i)).*(para_avgs(i)./Δ))^2).*w(i);
end
% Objective function
Q = (1/n)*sum(term);
```

In this excerpt of code, n refers to the number of parameters whose sensitivity is included in the objective function. This excerpt of the code begins by calling the function to run OPTUM G2 and compute the function output for the set of parameters. Then, one by one, each of the parameters are stepped by a set amount and a new function output is computed. The two functions outputs (from original parameters and stepped parameters) and the size of the step are used to compute a gradient. This gradient is the sensitivity and it is normalized and weighted, forming each of the terms within the quantitative metric. All weightings and step sizes are constant and predetermined. Details on the selections of each of these can be found in Chapter 4.

Run OPTUM G2: This is a function which acts as the main driver to determine the function output. All of the information needed for the execution of OPTUM G2 is delivered to the function as the input. The indenter dimensions must be used to compute the nodal coordinates and then these coordinates, the material parameters, and applied force are converted directly to an array to be used in modifying the model script. For each of the variables in the array there is a character in the model script that it will replace. For example the elastic modulus, E, will have a numeric value in the array which will replace a variable, '$\$E\$$'. Each of the variables in the model script are enclosed by $ to ensure they are unique in the model script. After the script is updated (details of how this is completed are below), the model script is executed by the dos command in MATLAB. Following the completion of the finite element analysis, OPTUM G2 saves the results in a .g2x file which can again be read by MATLAB. Details of how this file is read are provided below and the results obtained by reading the file are returned by the function.

Update OPTUM G2 script: The script used to run the model is copied each time the model is run from a template. In this template all of the variables are in their non-numeric form and the template is originally created by constructing the model in OPTUM G2 and saving the file. The function used to replace all of the non-numeric variables with their numeric values uses the MATLAB function $strfind$. The function used in this work has been adapted from the version developed by Kristian Krabbenhoft and available at $http://bit.ly/2xr7h51$.

Read results file: The function used to read the results file is called by the function used to run

OPTUM G2. The input of the function to read the results is the file name and the results points numbers. The results points are preset locations where OPTUM G2 is specified to record nodal data. The function is specified to search the results file for a known string identifying the location of the data. Then with the knowledge of the structure of the file the correct numerical result can be extracted, such as the displacement of a result point.

Optimization constraints: In addition to bounding all of the parameters an optimization constraint is used to ensure that the output of the function (in this case the finite element solver) is within a set of bounds. This is achieved in a MATLAB function by determining the finite element output and using the result in as inequality constraint, as presented in the simplified code exert below. If this function is not satisfied then the optimization will not return the parameters as a feasible solution.

```
function [c,ceq] = nonlcon(parameters)
    Δ = compOptum(parameters);
    c = [0.002-Δ;Δ-1];
    ceq = []; % No equality constraint
end
```

B.2.2 Specifics for Artelys KNITRO

Artelys KNITRO is a powerful nonlinear optimization solver. It includes seven different algorithms, with each containing state-of-the-art methods for solving the optimization. The software provides a wide variety of options to customize the solver, as detailed below, and the interface is very user-friendly. An additional feature that is particularly appealing to this work is that it is derivative-free, meaning the software provides options to compute the first and second derivatives needed for the optimization process.

KNITRO has a large variety of options to customize the optimization process, these options are categorized into 11 topics. Included below is a brief description of each of these categories and

their applicability to this work. Note that options not explicitly mentioned here were not set and therefore KNITRO's default value was used.

General options: These options make up the initial set up of the optimization problem and cover options applicable to the problem in general. Below is a list of the options used and their direct application.

- *algorithm:* The Sequential Quadratic Programming (SQP) algorithm is selected for use in this problem. The major appeal of this algorithm is it is targeted towards problems with expensive function evaluations and where derivatives are computed with finite-differences. Prior to its selection all algorithms were trialled with the tuner feature.

- *honorbnds:* This option is used to determine if KNITRO will enforce compliance with the specified variable bounds. Due to the nature of the problem being reliant on the parameters remaining within the bounds it is specified that KNITRO enforces the bounds.

Derivatives options: KNITRO uses the derivatives, both first and second, to inform the optimization process. When exact derivatives cannot be provided KNITRO provides a few options as to how to compute approximations. In the approximate cases first derivatives are finite-difference approximations for the gradient of the objective function and second derivatives are represented by an approximation of the Hessian matrix.

- *gradopt:* As KNITRO requires the gradients of the objective function, this options allows the user to specify how they will be supplied or should be calculated. As they are not known in this case, it is specified that KNITRO should calculate them using forward finite differences.

- *hessopt:* Similar to above, KNITRO also requies the hessian matrix. There are multiple options available although it is specified that KNITRO should compute a limited-memory quasi-Newton BFGS Hessian. This is most suited to this problem as the function evaluations are very expensive.

- *lmsize:* This option is used to specify the number of limited memory pairs to store when computing the hessian. The larger the value the more accurate, but also more expensive in computation time. Trial and error was used to determine a value of 10.

Termination options: As the name suggests, the termination options guide the termination of the solver. Generally smaller tolerances result in a longer time to solve the optimization and a more accurate solution. All of the default values were left for this section.

Barrier options: This set of options contains multiple applicable options. Most options, if left unspecified, will indicate that KNITRO will select the option it deems most applicable. This is the case for all the options of interest in this section.

Active-set options: The active-set options guide the use of sub-problems used to assist in solving the optimization. Through the use of the tuner option, it was determined that the default constraints were sufficient in solving the analysis.

MIP options: Mixed integer programming (MIP) constrains at least one of the variables to be an integer. None of the variables in this work require a constraint to be an integer and therefore this set of options was not used.

Multi-algorithm options: There are seven different algorithms to select from in KNITRO. The multi-algorithm options allow for a section of these algorithms to used to solve the optimization. Although, multi features cannot be used in series in MATLAB, they must be run in parallel and therefore multi-algorithm is not needed as running multiple algorithms can be achieved with the $algorithm$ option.

Multi-start options: KNITRO is a local optimization solver, meaning it finds a local minimum and cannot guarantee that the local minimum is also a global minimum. Although, with the use of multi-start the final result can be more confidently treated as a global optimal. Multi-start was used in this work with the options specified below.

- *m-enable:* Multi-start is enabled through this option and therefore it is required.

- *ms-maxsolves:* The max solves indicates how many starting locations will be used by the

solver. In this work 50 was specified.

- *ms-terminate:* This option allows the user to specify when to terminate the optimization, such as when the first local minimum is found or after the $ms - maxsolves$. After $ms - maxsolves$ was selected.

Parallelism options: This set of options allows computations of the optimization to be simultaneously run. However, KNITRO in MATLAB cannot be run in parallel, therefore, this set of options is not applicable to the work outlined in this thesis.

Output options: These allow the optimization output to be customized. All options were left as the default options and within the MATLAB functions, the desired data was manually recorded in text files. Data was recorded this way as it was important to the analysis to retain the normalized parameter sensitivities which make up the objective function, and these values are not known to the solver.

Tuner options: The tuner in KNITRO should be run at the commencement of a project. It provides recommendations on the options to use and what settings of these options to implement. This was used at the beginning of this project and assisted in informing some of the settings previously described.

Each of the above specified options were used in the optimization included in Chapter 4. Note that most optimizations prior to Chapter 4 were solved with the global optimization solver BARON, run in AMPL. Although as outlined at the beginning of this appendix, BARON and AMPL were not compatible with the more complex problem involving the finite element analysis.

B.2.3 Specifics for OPTUM G2

The finite element analysis is intended to be the first step beyond the analytical implementation of the quantitative metric, and for this reason, it is kept relatively simple. As previously detailed, OPTUM G2 is a geotechnical finite element analysis software that is particularly desirable to this application due to the ability to run the analysis from the command window, saving significant time

during the optimization. A Mohr-Coulomb model is used, characterized by E, ν, ϕ, and c. The model size is 30 m wide and 20 m deep to ensure the boundaries do not influence the the analysis. A fixed load is applied to a rigid body, and this is this is achieved by creating a rigid body the size of the indenter and placing a plate on the top edge. A fixed load is then applied to the plate.

The major modification to this finite element analysis, beyond running this simple analysis, is the automation component, where MATLAB is able to manipulate the OPTUM G2 run file and retrieve outputs from new configurations of the indenter or for different material parameters. An excerpt of the run file, detailing the geometry of the simulation, that is modified is presented below to provide an example of how the automatic modifications are made.

```
<Bounds>0,0,30,20</Bounds>
<Nodes>
  <!--Node #, X, Y-->
  <Node ID="1" IsConnector="0">0,0,0</Node>
  <Node ID="2" IsConnector="0">0,20,0</Node>
  <Node ID="3" IsConnector="0">30,20,0</Node>
  <Node ID="4" IsConnector="0">30,0,0</Node>
  <Node ID="5" IsConnector="0">$x5$,$y5$,0</Node>
  <Node ID="6" IsConnector="0">$x6$,$y6$,0</Node>
  <Node ID="7" IsConnector="0">$x7$,$y7$,0</Node>
  <Node ID="8" IsConnector="0">$x8$,$y8$,0</Node>
  <Node ID="9" IsConnector="0">$r1$,20,0</Node>
  <Node ID="10" IsConnector="0">$r2$,20,0</Node>
</Nodes>
```

Here the geometry of the indenter is characterized by nodes 5 - 8 (see Chapter 4 and Figure 4.1) and the variables encapsulated by $ signs are replaced by their respective numeric values by the *Update OPTUM G2 script* (described above). Furthermore, nodes 9 and 10 refer to the location of results points, the location of these points are updated to be $0.5B$ and $2B$ from the edge of the indenter. These results points were used to determine the impact of varying the measurement

location in Section 4.2.

Further details of the impact of changing variables on the OPTUM G2 output are provided in the main body of the thesis (Section 4.2) as these have a direct impact on the analysis completed.

APPENDIX C
PROCESS OF RUT RECONSTRUCTION WITH PIX4DMAPPER AND MATLAB

A continuous reconstruction of data over a significant distance for the purpose of material parameter determination does not yet exist in the form presented in this work. Therefore, this appendix details the relevant information to reproduce this process. Firstly, Sections C.1 and C.2 cover the selection of the hardware and software used, relevant to the reconstruction only—not referring to the ability to infer material conditions. Then, Section C.3 covers the process of reconstructing the point cloud from the filmed videos, using Pix4Dmapper and Section C.4 details the process of analysing the point clouds in MATLAB to extract the desired information.

C.1 Selection and use of hardware—GoPro

Two GoPros were selected as the camera to film the ruts in the field work conducted. Their selection was primarily due to a combination of the GoPro's tough nature and sufficiently high film quality. The requirements for a sufficient photogrammetry system is (1) at least two cameras to ensure that the reconstruction has multiple aspects and (2) a minimum filming quality of 1080p to allow sufficient accuracy and density of the resulting reconstruction. A significant point to note, to allow for easier reconstruction at later stages, is to ensure the settings for filming are preset in the reconstruction software or are at least known. Settings such at focal length and pixel dimensions are used by the photogrammetry software in the reconstruction and are preset by most photogrammetry software for common cameras and brands. This was not done in the filming of this work and as a result major difficulties were faced during the processing of the media further details of these lessons learnt are in Section C.3.1.

C.2 Selection of software—Pix4Dmapper and MATLAB

The selection of the photogrammetry software used is possibly the most important choice of this work. It is not possible to gain accurate results without an accurate model to analyse, and it is possible to make up for errors made during filming—as was done in this work. Therefore careful consideration was given to other software with a total of five trialed before selecting Pix4Dmapper. The software which were trialed include: 3DF Zephyr, Autodesk ReCap Pro, Agisoft Metashape, and Neitra 3D. It is more common in photogrammetry to reconstruct an object by taking many pictures from different angles of a single object rather than using fewer angles and a more elongated object. The latter is the case for this analysis and thus the selection of the photogrammetry software was non-trivial. Whilst all are powerful photogrammetry software, Pix4Dmapper was determined to be the best choice for this work. The most significant reasoning for this included that other software often limited the number of frames which could be analysed in a single model and had difficult processes for adding manual tie points. Furthermore, during the trialing of software, Pix4Dmapper was the most capable in optimizing the camera presets, as these were previously unknown.

Once Pix4Dmapper is used to reconstruct the ruts, the reconstructions need to be analysed to extract the desired data. The obvious choice to complete this analysis is MATLAB. It is more than capable and extremely user friendly.

C.3 Reconstruction using Pix4Dmapper

The process for reconstructing the ruts in Pix4Dmapper section is split into pre and post-processing, where pre-processing is considered to be that used by Pix4Dmapper to create the reconstruction and post-processing is the modifications made by the user to improve the quality of the reconstruction.

C.3.1 Pre-processing settings

The first step of pre-processing is to import the media file/s and provide all of the model data. This includes:

- ***Media import:*** Can be in photo or video form, ensue not too many or too few frames are used, this will lead to inaccurate reconstruction and impractically large files, respectively. Video with approximately 5fps is used in this case. 5fps is derived from the videos filmed at 60fps and every 12 frames imported.
- ***Camera details:*** Well known cameras are preset, unknown details can be overcome with Pix4Dmapper's optimization of camera details.
- ***Location details:*** Geo-coordinates of images

Two major errors were made during the filming stage which were identified at this point of the reconstruction process. Firstly, all videos were recorded on the GoPro's with a corrective setting turned on to account for the fish eye lens, meaning that frames were distorted and Pix4Dmapper did not have a preset for the camera filming settings. This was overcome by working with a single rut to reoptimize, adding manual tie points and updating the camera settings as Pix4Dmapper converged on the modified camera settings. Secondly, the GPS feature on the GoPros was turned off during filming, meaning that the location of the frames could not be used to further assist the reconstruction of the ruts.

Next the processing options for Pix4Dmapper are broken down into three categories corresponding to the stages of the analysis: (1) initial processing, (2) point cloud and mesh, and (3) DSM, orthomosaic and index. Since the point cloud was the desired output for this analysis the third stage was not required and can be disregarded. The key features of the first stage include,

- ***General:*** The image size should be set to *full* for the most precise results.
- ***Matching:*** *Custom* should be used to allow for variation, limiting neighbouring images by capture time to 8 and increasing image similarity to 50. This produced the best results in this

analysis. Additionally, the number of image pairs per manual tie point should be maximized (to 100). Finally, *use time for multiple cameras* should be selected.

- ***Calibration:*** *Rematch* should be allowed by selecting *custom* under *rematch*. This allows for more matches to be added after the initial processing.

These features, and in particular the matching settings, can have a significant impact on the quality of the initial reconstructions and should be considered for modifications if the reconstruction is not sufficient.

Next, the notable features of the second stage include:

- ***Point cloud:*** It is essential for this application that the image size is 1 (corresponding to full image size) and that the point density is high. Furthermore, the export should be set to LAS.
- ***3D textured mesh:*** All default settings are sufficient, as a 3D textured mesh is not used in the export of this application.
- ***Advanced:*** No advanced settings are needed.

C.3.2 Post-processing settings

The post processing is a very important stage of the photogrammetry analysis. As the reconstructed ruts in this work are complex, and the provided media was lacking in areas needed for photogrammetry (varying angles/aspect of frames/unaltered frames), post processing can work to improve the rut reconstruction quality. Prior to post processing the ruts reconstructed as part of this work had approximately half of the frames calibrated. The remaining uncalibrated half needed to be calibrated with post processing. The general process for post processing is as follows:

- ***Assessing image linearity:*** As the vehicle making the ruts was driven in a straight line and the videos were taken directly from a camera being pulled by the vehicle, the frames in Pix4Dmapper should also line up in a straight line, with each frame a small distance apart. Furthermore there should be two lines of images close together, representing the two cameras

used to film each rut. Images that fall out of this pattern should be identified as errors and worked to be improved.

- ***Adding manual tie points:*** The images presenting as errors should be tied to images presenting in the correct location by adding manual tie points. These are points the user selects that appear in multiple images (including both images presenting correctly and incorrectly). Multiple manual ties points (at least 3) should be added around problematic areas to improve the reconstruction. Furthermore, manual tie points can be used to calibrate previously uncalibrated images.

- ***Rematch and optimize:*** Completing this step allows for Pix4Dmapper to account for the added manual tie points and include new automatic tie points. Manual tie points should be continued to be added followed by re-matching and re-optimizing until the reconstruction is sufficient. Note it is possible that the process of re-matching and re-optimizing can increase or create new problematic areas. This simply requires more manual tie points or an adjustment of the settings covered in Section C.3.1.

Once the rut is sufficiently reconstructed, the process to export the point cloud from Pix4Dmapper can begin. First, the point cloud needs to be constructed. This is done by running stage (2) of the processing steps. Following this, the point cloud can be opened and cropped to allow for all outliers to be removed. The ruts created in this work produced many outlying points caused by the ruts being filmed with a larger field of view than needed. This lead to distant features, such as people, the ocean, and the sky, being included in the point clouds. Once these additional features are removed, the point cloud can be exported (as a .las file).

C.4 Analysis using MATLAB

The analysis in MATLAB is used to take the point cloud (.las file) and reconstruct a rut profile along the distance of the rut. This analysis is coded into a single automatic process for which the general procedure is detailed in the following subsections.

This section specifically follows the process of determining the rut dimensions, but a similar process can be used to extract any required data from the point cloud.

C.4.1 Importing and reorienting the point cloud

The point cloud that is exported from Pix4Dmapper is then imported to MATLAB and converted to a cell array containing the x, y and z coordinates of approximately five to ten million points which make up the rut. The cell array is then converted to numeric arrays for x, y and z.

Each of the point clouds vary slightly in the form in which they are exported from Pix4Dmapper, in that their x, y and z coordinates can be flipped or on the negative axis. Therefore, they are first aligned so as they are in a known orientation for the analysis. The coordinate system used assumes the North end of the rut (closest to the pier) is at the y = 0 location, and the rut extends in the positive y-direction towards the south. This reorienting process is completed manually by identifying features of the point cloud which correspond to known locations and then transferring this knowledge to how the rut is presenting in MATLAB after extracting the point coordinates.

C.4.2 Scaling based on known features

When using Pix4Dmapper with known camera properties, the reconstruction will be in realistic dimensions (with the units specified in the Pix4Dmapper analysis). However, as is mentioned previously, the camera settings used in this work are not known, and therefore realistic dimensional reconstructions were not possible. For this reason, each of the ruts analysed in MATLAB are scaled based on known features. The most convenient known feature is the width of the rut in a location with little to no rut or berm—a location of stronger material. As with the orienting process, this is again a manual process and requires referring to the reconstruction in Pix4Dmapper. This step could be avoided with filming in a known preset camera configuration.

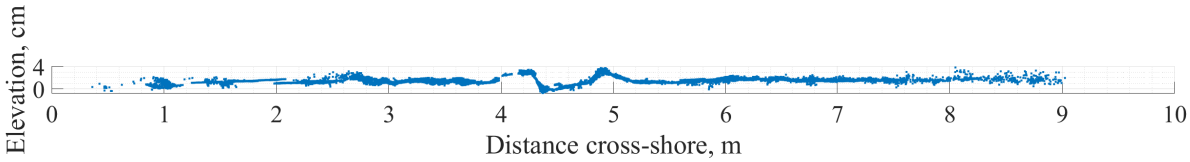

Figure C.1: Slice of rut sample.

C.4.3 Slicing the rut

A slice of the rut is taken approximately every 100 mm and accounts for a single set of measurements (berm height and rut depth used to compute the total rut height). The 100 mm slice width was selected with trial and error Theoretically the slice width would approach zero to get the most accurate analysis of the real world situation. However, as the slice width decreases, the number of points in the slice decrease, and the measurements become more susceptible to error caused by noise in the point cloud. Furthermore, for many of the locations along the rut, the berms were uneven and made up of clumps of sand, causing a less uniform berm. By averaging over small sections a better approximation the the rut height can be made. Figure C.1 presents a sample slice taken directly from the reconstruction of Rut 1 on Day 4, where both the elevation and distance cross-shore are local to the slice and the cross-shore distance refers to the direction perpendicular to the length of the beach.

C.4.4 Approximating the surface level

Due to the topology of the beach, each of the slices are subjected to their own individual geometry. Therefore, a local coordinate system must be implemented to extract measurements. This is done by approximating the surface level with a plane. The plane is determined by,

$$Ax_i + By_i + Cz_i + D = 0 \tag{C.1}$$

Each individual plane is specified with optimization, by minimizing the sum of the distance of all the points in the slice from the plane. This is presented mathematically as,

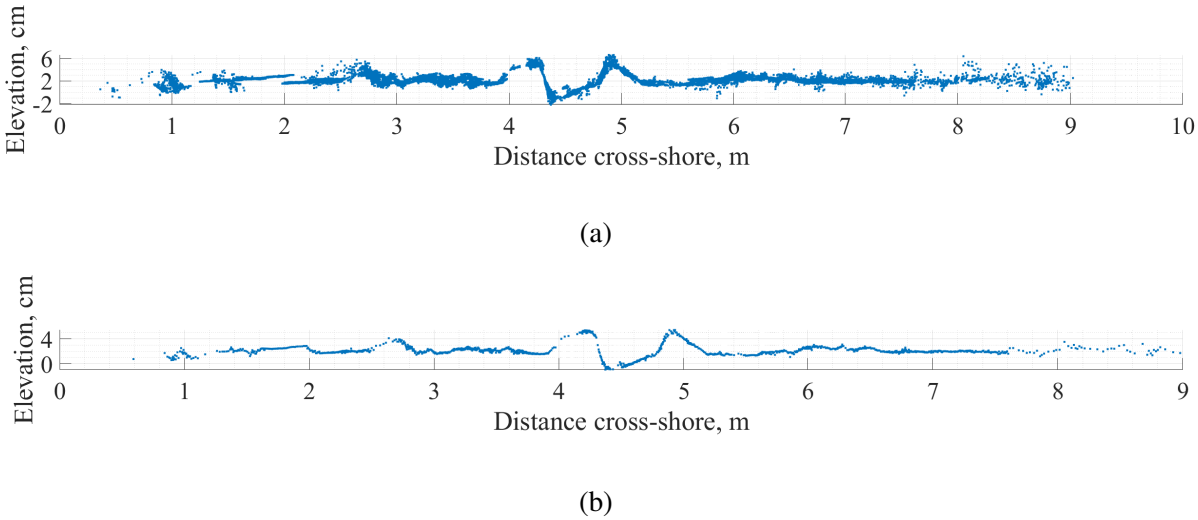

Figure C.2: Modified slice of sample rut: (a) slice plotted as distance from plane; (b) slice plotted as distance from plane and points averaged.

$$\min_{plane} = \sum_{i=1}^{n} \frac{|Ax_i + By_i + Cz_i + D|}{\sqrt{A^2 + B^2 + C^2}} \tag{C.2}$$

where n is the number of points in the slice and x_i, y_i and z_i are the coordinates of a point.

Once the optimal plane is known, each of the points in the slice can be plotted as a distance from the plane. Using the same slice presented in Figure C.1 this is now plotted as a distance form the plane on the z-axis and presented in Figure C.2a. The susceptibility of the slice to noise is reduced at this stage by averaging the points. The points are averaged by arranging them in order by their x-coordinate and computing the arithmetic mean of every 10 points. Figure C.2b shows the same slice after it has been filtered using this averaging method.

C.4.5 Measure max berm height and rut depth

Finally, from the configuration where the points are plotted as a function of distance from the plane, the maximum berm height is taken as the maximum positive distance from the plane, and the rut depth as the maximum negative distance. The total rut height is considered as the sum of these two measurements. It is not always the case that the slices produce such perfect reconstruc-

tions as shown above and in some cases the rut is not even visually identifiable. This is the main contributor to the significant noise that is produced in the final reconstructions (see Figure C.3). Multiple strategies are in-place to reduce the possibility of noisy slices or badly reconstructed areas impacting the measurements taken. One of these strategies is averaging the points as described in Section C.4.3. Another check confirms that there are at least 10 other points within 50 mm either side of identified location that are within 20 mm vertically. A final check is used to ensure that the two measurements, rut depth and berm height, are within 400 mm of each other, in the x-direction. These checks attempt to ensure that the identified locations, of the berm height or rut depth, are not outlying points.

C.4.6 Filtering and averaging data

Following the determination of the total rut height for each of the slices these can be plotted with distance along the rut, as shown in Figure C.3a. It can be seen that this is a noisy function, although there is evidence of a trend. In order to filter this function, MATLAB's $smooth$ function is used with a gaussian filter. The result of the filtered data is shown in Figure C.3b. Finally, an additional effort to further smooth the curve is made by averaging every 10 data points, and the final result of this is presented in Figure C.3c.

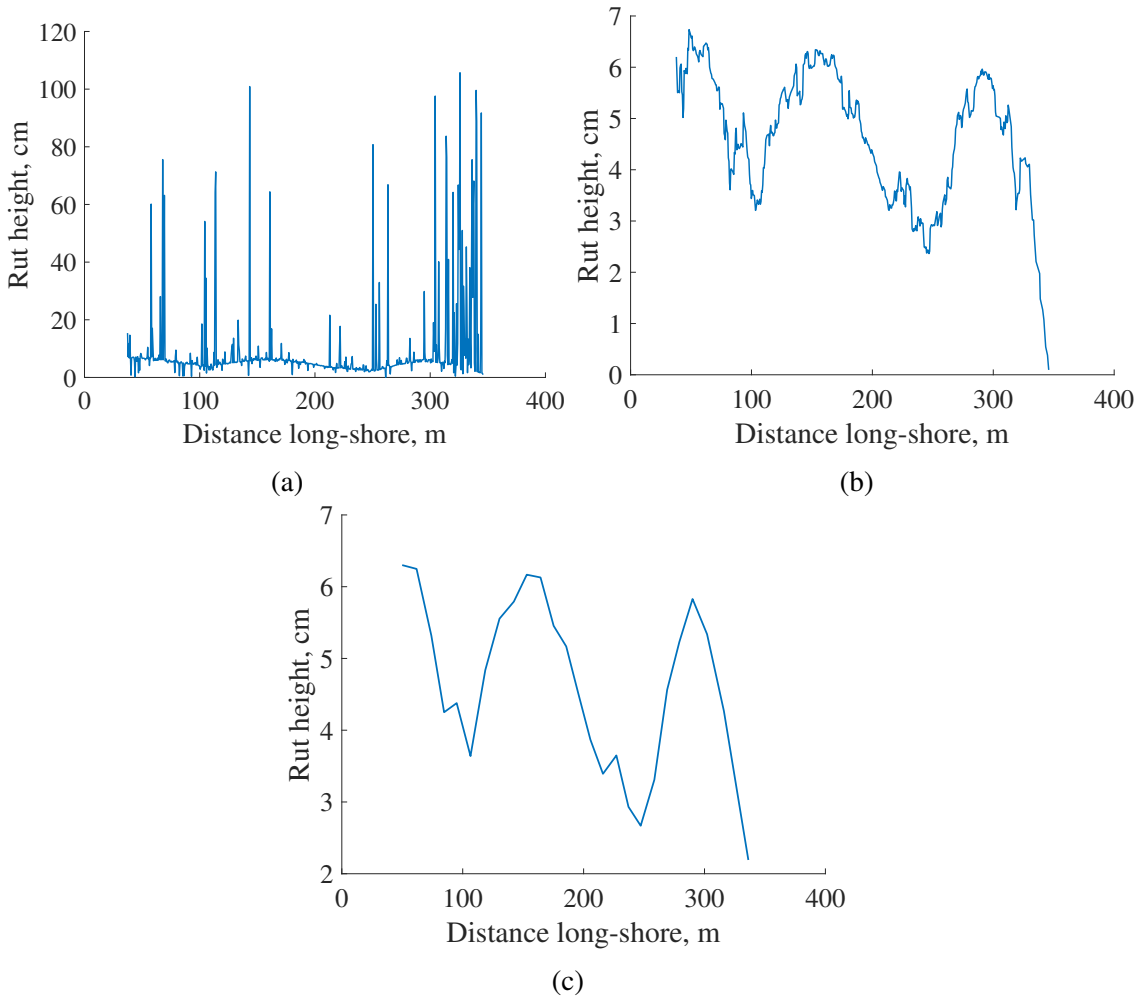

Figure C.3: Filtering of to rut reconstructions: (a) original data; (b) filtered data; (c) filtered and averaged data.